

## Strong-field approximation and its extension for high-order harmonic generation with mid-infrared lasers

This content has been downloaded from IOPscience. Please scroll down to see the full text.

2016 J. Phys. B: At. Mol. Opt. Phys. 49 053001

(<http://iopscience.iop.org/0953-4075/49/5/053001>)

View [the table of contents for this issue](#), or go to the [journal homepage](#) for more

Download details:

IP Address: 129.130.106.65

This content was downloaded on 18/02/2016 at 14:16

Please note that [terms and conditions apply](#).

## Tutorial

# Strong-field approximation and its extension for high-order harmonic generation with mid-infrared lasers

Anh-Thu Le<sup>1</sup>, Hui Wei<sup>1</sup>, Cheng Jin<sup>2</sup> and C D Lin<sup>1</sup><sup>1</sup>Department of Physics, Cardwell Hall, Kansas State University, Manhattan, KS 66506, USA<sup>2</sup>School of Science, Nanjing University of Science and Technology, Nanjing, Jiangsu 210094, People's Republic of ChinaE-mail: [atle@phys.ksu.edu](mailto:atle@phys.ksu.edu)

Received 30 June 2014, revised 1 August 2015

Accepted for publication 15 September 2015

Published 15 February 2016



CrossMark

**Abstract**

In recent years intense mid-infrared lasers with wavelength of a few microns have become the standard tools for research in strong field physics laboratories worldwide. These lasers offer the opportunities to extend the traditional study of high-order harmonics generation and attosecond sciences from the extreme ultraviolet to soft x-rays. In this tutorial we revisit the familiar strong field approximation and its simplification—the quantum orbits theory. We draw special emphasis on the factorization of laser induced dipole moment as the product of a returning electron wave packet with the photo-recombination dipole transition matrix element. The former depends on the laser properties only (up to a normalization constant) while the latter is related to laser-free photoionization transition dipole. The factorization leads to the suggested modification beyond the strong field approximation—the quantitative rescattering theory. In applying these theories to mid-infrared lasers, we analyze the behavior of the returning electron wave packet and its scaling properties vs the wavelength of the laser. A few examples are given to demonstrate how the quantitative rescattering theory is capable of reproducing experimental harmonic spectra under various conditions. Future opportunities in employing harmonics generated by optimized mid-infrared lasers for probing molecular structure and for serving as useful table-top coherent light sources up to the x-ray region are also discussed.

Keywords: harmonic generation, intense laser field, attosecond physics, mid-infrared lasers

(Some figures may appear in colour only in the online journal)

**1. Introduction**

Over the last twenty-five years, tremendous progress has been made in the understanding and application of high-order harmonic generation (HHG) [1]. HHG offers the potential for creating new table-top coherent light sources from the extreme ultra-violet (XUV) to the x-ray regions. Such new light sources may be in the form of single attosecond pulses (SAP) as short as below about 100 as [2, 3], or in the form of attosecond pulse trains (APT) [4]. Availability of attosecond pulses has opened up a new area of research of attosecond

science [1] in recent years. Another important application is HHG spectroscopy, which aims at obtaining atomic and molecular structure information from the measured HHG spectra [5–13]. With the availability of ultrashort laser pulses of duration of sub-ten femtoseconds, HHG spectroscopy is a powerful tool for ultrafast imaging [14–16] of a dynamic molecular system. To make further progress in the field it requires not only advances in technological and experimental tools, but also theoretical insight that offers the capability to perform theoretical simulations in order to understand the basic mechanisms responsible for the observed harmonics,

and to decode the information embedded in the measured harmonic spectra.

Since the early days, HHG has been understood qualitatively in terms of the three-step model (TSM), also called the recollision or rescattering model, proposed by Corkum [17]. Historically, this recollision picture was also discovered by Kulander and collaborators [18], who called it the simple man model. Within the classical recollision model, an HHG process is understood in terms of the following three steps. First, the active electron tunnels out of the potential barrier formed by the quasi-static electric field of the laser and the Coulomb potential of the atomic core. Tunneling happens most likely near the peak of the laser sub-cycle. Second, after the electron is born into the continuum it propagates in the strong laser field. Third, as the laser reverses its electric field direction, the electron has a chance to be driven back to the parent ion and recombine with the core to emit a high harmonic photon. A similar concept of ‘atomic antenna’, but in a less transparent form, has been suggested earlier by Kuchiev [19].

For semi-quantitative calculations, a detailed theory of HHG based on the strong-field approximation (SFA) was first given by Lewenstein *et al* [20]. (In fact, a brief description of the theory was given even earlier in L’Huillier *et al* [21]). This model of HHG is either called SFA or Lewenstein model. It is an extension of the SFA for ionization of atoms and solids in intense laser fields first proposed by Keldysh [22] and later expanded by Faisal [23] and Reiss [24]. For strong-field ionization, this is also called Keldysh-Faisal-Reiss (KFR) theory [25]. The SFA can be considered as a quantum version of the TSM. Similar to the TSM, it can also be extended to describe related recollision phenomena such as high-energy above-threshold ionization (HATI) (see, for example, reviews by Milošević *et al* [26] and Becker *et al* [27]) and non-sequential double ionization (NSDI) in atoms [28–31].

At the quantitative level, high harmonic generation and related nonlinear strong field processes can, in principle, be obtained by numerical solution of the time-dependent Schrödinger equation (TDSE). In reality, TDSE calculations are very time-consuming and accurate numerical results are difficult to come by, except for simple atoms or molecules within the single-active-electron (SAE) approximation. In spite of these difficulties, various groups have performed *ab initio* calculations, mostly for simple atoms like helium and small molecules, by including full (or truncated) degrees of freedom of the system, using the TDSE or the simplified methods such as the time-dependent density functional theory (TDDFT) and time-dependent Hartree–Fock (TDHF) method [32–38]. If such calculations indeed are carried out accurately, then the results can be used to benchmark against simpler approximate models such as the SFA and others. It is highly impractical to use these methods to generate theoretical results to compare directly with experimental data. We emphasize that experimental HHG spectra are obtained from a focused beam. Inclusion of HHG generation and propagation in the medium would require such calculations be carried out for hundreds of laser intensities. To our knowledge, only recently has TDDFT calculations been carried out at this level [39, 40] for HHG generated by 800 nm lasers for Ar. To

extend similar calculations to molecular targets or to mid-infrared lasers would require even much more effort with accuracy that is difficult to check.

Theoretical calculations of HHG starting with the SFA has many advantages since it can efficiently be applied to atoms as well as complex polyatomic molecules. However the SFA has a serious drawback since it is not accurate. To improve the SFA, it is best to start by identifying where it fails. A practical method to improve is first to use saddle point approximation to reduce the SFA induced dipole to a factorized form, where each factor is associated with an individual step of the three-step model. By replacing each of these factors with an ‘improved’ one, the new formula is then shown to provide a better description of the harmonic generation process. This approach has been suggested by Ivanov *et al* [9, 41] who factorized the SFA in the time domain. Such a factorization is not complete since one still has to sum over different born times (or ionization times) during the laser pulse. Note that the original TSM by Corkum was also formulated in the time domain [17]. One can go one step further to get a ‘partial’ factorization in the energy domain. This is achieved in the so-called quantum orbits (QO) theory [20, 27, 42–44].

Today, one of the most accurate and efficient methods for calculating HHG is the quantitative rescattering theory (QRS) [12, 45, 46]. In the QRS, the HHG dipole as a function of harmonic photon energy is factorized as a product of returning electron wave packet and *exact* photo-recombination transition dipole. This factorization is in the energy domain. The QRS was proposed based on the numerous evidence from the numerical solution of the TDSE for atomic targets [45–47] and molecular ion  $H_2^+$  [48]. Furthermore, HHG spectra from the QRS have been found to agree well with various experiments for atoms [49, 50] and molecules, including aligned molecules [11, 51] and polyatomic molecules [52–54]. In the QRS, it is essential that the electron wave packet can be accurately calculated from the SFA. Once theoretical transition dipoles for the target are known in the required energy range, the QRS allows efficient calculations of the HHG spectra as the laser parameters are varied. Such efficiency further speeds up the solution of the macroscopic propagation equations in order to obtain harmonics generated from the gas medium that can be readily compared to experiments. Indeed, macroscopic HHG spectra calculated based on the QRS have been shown to agree well with various experiments [55–58].

It is interesting to note that a factorization similar to that of the QRS has been proposed by Itatani *et al* [6]. The validity of that factorization has also been critically tested numerically within the SFA in [59], showing that it is valid only if the transition dipole was calculated in the plane-wave approximation. In fact, factorization can also be derived *rigorously* within the QO approach which is an approximate SFA. Therefore, in the spirit of the QRS, the returning electron wave packet can be obtained from the SFA or from the QO theory. Similar derivation of factorization has been reported later by other groups [60–64].

For more than twenty years, high harmonics are nearly always generated with Ti-sapphire lasers with wavelength

centered close to 800 nm. In the last few years, with new laser technology, high harmonics are generated with mid-infrared lasers with wavelength covering from about 1  $\mu\text{m}$  up to about 4  $\mu\text{m}$ . Such mid-infrared lasers allow the generation of harmonic spectra extending to soft- and sometimes hard-x-ray regions [65–72]. While the SFA theory is expected to work for such lasers, it is desirable to examine how HHG and, especially, its electron wave packet, depend on the wavelength. As the wavelength is increased, the semiclassical approximation of SFA, i.e., the QO model, becomes more accurate. Since QO theory is conceptually related to the classical three-step model (TSM), harmonics generated by mid-infrared lasers can thus be analyzed in terms of classical concepts such as ionization versus recombination times, long versus short electron trajectories, as well as recombination by first versus higher order return. Furthermore, the QO theory can be cast mostly in analytical form which allows us to study harmonic generation in the long wavelength limit analytically.

The goal of this tutorial is to provide a detailed analysis of the strong field approximation for HHG with the emphasis on the application with mid-IR lasers, when the QO theory becomes more adequate. This tutorial is organized as follows. In section II, we first enumerate the various formal approximations made in order to obtain the SFA from the TDSE. By employing saddle-point approximation on the SFA integral, we then derive the QO theory. In the QO theory, concept and expressions that can be related to the motion of a classical electron in an oscillatory electric field can be derived, except that they are complex quantities. In the QO theory, harmonics are generated from a sequence of recollision events. The relative importance of harmonics from each recollision event can be analyzed as the wavelength of the driving laser is increased. Furthermore, from the QO theory, we derive the factorization of the laser induced dipole for HHG in the energy domain. By analyzing in which step the SFA works and which step fails, a quantitative rescattering model (QRS) is empirically derived. Here we pay special attention to the concept of the electron wave packet and its different forms. In section II we also analyze the nature of the long and short electron trajectories of the first and higher order returns, especially within the QO theory. This analysis is then extended to mid-IR wavelengths in section III, where we discuss the wavelength scaling of HHG in the long wavelength limit. In section IV we summarize the theory of macroscopic propagation of harmonics in the gas medium. Using the QRS for the single atomic or molecular induced dipoles as inputs to the propagation equations, we can compare our macroscopic simulations directly with experimentally measured harmonics, thus allowing us to draw wavelength scaling of the macroscopic HHG yields. Furthermore, using the QO theory we can identify how contributions from different orbits behave and phase match in the medium. A short section V is devoted to illustrate some applications based on the QRS theory. The tutorial is concluded with a short summary and future outlook.

In this tutorial we have not attempted to cover all the extensive works published on the SFA and related methods. Thus, unlike a review article, our references are far from

complete. Furthermore, while we have shown how the QRS can be applied to many areas of strong field physics, we do not cover many specific applications. For these, the readers are referred to the original publications. Atomic units are used throughout the paper, unless otherwise indicated.

## 2. Theoretical models for high-order harmonic generation

### 2.1. Lewenstein model or strong-field approximation for HHG

**2.1.1. Formal derivation of Lewenstein model.** The strong field approximation (SFA) is a widely used model for atoms or molecules in an intense laser field. The main assumption made in SFA is that the continuum electron dynamics is dominated by the laser field while the core potential is a small perturbation that can be ignored to the lowest order. The majority of strong field effects can be understood at least qualitatively by the SFA model, which is much less computational demanding than solving the TDSE numerically. In this subsection the SFA model describing HHG process is derived using a number of approximations from the TDSE in the length gauge. This model is usually referred to as Lewenstein model [20] that serves as a starting point in many HHG studies.

Consider an atom (or an ion) in a single active electron (SAE) approximation under the influence of an intense laser field  $\mathbf{E}(t)$ , the Schrödinger equation in the length gauge takes the form

$$i\frac{\partial}{\partial t} |\Psi(\mathbf{r}, t)\rangle = \left( -\frac{1}{2}\nabla^2 + V(\mathbf{r}) + \mathbf{r} \cdot \mathbf{E}(t) \right) |\Psi(\mathbf{r}, t)\rangle, \quad (1)$$

where  $V(\mathbf{r})$  is the potential due to the ionic core.

The total Hamiltonian can be decomposed as

$$H(t) = H_0 + \mathbf{r} \cdot \mathbf{E}(t). \quad (2)$$

The field free Hamiltonian

$$H_0 = -\frac{1}{2}\nabla^2 + V(\mathbf{r}) \quad (3)$$

determines the ground state  $|g\rangle$  and the excited bound states  $\{|e\rangle\}$  of this system

$$H_0 |g\rangle = -I_p |g\rangle, \quad (4)$$

$$H_0 |e\rangle = E_e |e\rangle, \quad (5)$$

where  $I_p$  is the ionization energy.

The electron in the continuum can also be described by the eigenstates of  $H_0$

$$H_0 |\mathbf{k}\rangle = \frac{k^2}{2} |\mathbf{k}\rangle, \quad (6)$$

where  $\mathbf{k}$  is the kinetic momentum of the outgoing electron.  $|g\rangle$ ,  $\{|e\rangle\}$  and  $\{|\mathbf{k}\rangle\}$  form a complete basis set of the whole Hilbert space.

Consider the case that the field intensity is large enough so that the Keldysh parameter  $\gamma = \sqrt{I_p/2U_p} \lesssim 1$ , with  $U_p = \frac{E_0^2}{4\omega_L^2}$  being the ponderomotive energy. By assuming that the electron in the ground state is tunnel ionized into continuum directly without intermediate resonances, then all the excited bound states can be ignored. Furthermore, consider the situation of weak ionization, which requires the intensity be much smaller than the saturation intensity. In this situation only a small fraction of the targets are ionized during the interaction time so that the depletion of the ground state can be neglected. Within the above assumptions the wavefunction can be expanded as

$$|\Psi(t)\rangle = e^{iI_p t} \left\{ |g\rangle + \int d^3k b(\mathbf{k}, t) |\mathbf{k}\rangle \right\}. \quad (7)$$

The HHG spectrum with polarization along a direction  $\mathbf{e}_i$  can be calculated from the time-dependent induced dipole moment

$$D_i(t) = \mathbf{e}_i \cdot \mathbf{D}(t) = \mathbf{e}_i \cdot \langle \Psi(t) | \mathbf{r} | \Psi(t) \rangle \quad (8)$$

from its Fourier components as

$$P(\omega) \propto \omega^4 |D_i(\omega)|^2. \quad (9)$$

Consider the transitions between continuum state and ground state which contribute to the harmonics while dropping the higher order continuum-continuum part, the induced dipole can be written as

$$\mathbf{D}(t) = \int d^3k \langle g | \mathbf{r} | \mathbf{k} \rangle b(\mathbf{k}, t) + \text{c.c.} \quad (10)$$

Next we use the Keldysh theory (or the KFR model) [22–24] in the length gauge [73] to evaluate the induced dipole moment. The KFR model (or its generalization in the form of the S-matrix theory [25]), was initially derived for strong field above-threshold ionization [22–24, 73, 74]. The approach to HHG process here is equivalent to the original derivation given by Lewenstein [20].

We introduce the time evolution operator  $U(t, t')$  for the total Hamiltonian  $H(t)$  such that

$$|\Psi(t)\rangle = U(t, -\infty) |\Psi(-\infty)\rangle = U(t, -\infty) |g\rangle, \quad (11)$$

and the time evolution operator  $U_0(t, t')$  for the field-free Hamiltonian  $H_0$  such that

$$U_0(t, -\infty) |g\rangle = e^{iI_p t} |g\rangle. \quad (12)$$

From equation (7),  $b(\mathbf{k}, t)$  can be solved as

$$b(\mathbf{k}, t) = e^{-iI_p t} \langle \mathbf{k} | U(t, -\infty) |g\rangle. \quad (13)$$

By substituting equation (13) into equation (10) we obtain

$$\begin{aligned} \mathbf{D}(t) &= \int d^3k e^{-iI_p t} \langle g | \mathbf{r} | \mathbf{k} \rangle \langle \mathbf{k} | U(t, -\infty) |g\rangle + \text{c.c.} \\ &= e^{-iI_p t} \langle g | \mathbf{r} U(t, -\infty) |g\rangle + \text{c.c.} \end{aligned} \quad (14)$$

Based on the S-matrix theory [24, 73], the above equation can be rewritten as

$$\begin{aligned} \mathbf{D}(t) &= e^{-iI_p t} \left\{ -i \int_{-\infty}^t dt' \langle g | \mathbf{r} U(t, t') \right. \\ &\quad \left. \times \mathbf{r} \cdot \mathbf{E}(t') U_0(t', -\infty) |g\rangle \right\} + \text{c.c.} \\ &= -i \int_{-\infty}^t dt' e^{-iI_p t'} \langle g | \mathbf{r} U(t, t') \\ &\quad \times \mathbf{r} \cdot \mathbf{E}(t') e^{iI_p t'} |g\rangle + \text{c.c.} \end{aligned} \quad (15)$$

The total Hamiltonian can also be decomposed as

$$H(t) = H_F(t) + V(\mathbf{r}). \quad (16)$$

$H_F(t)$  is the Hamiltonian of a free electron in the laser field

$$H_F(t) = -\frac{1}{2} \nabla^2 + \mathbf{r} \cdot \mathbf{E}(t), \quad (17)$$

whose eigenstates are the Volkov states (in the length gauge)

$$|\chi_{\mathbf{p}}(t)\rangle = |\mathbf{p} + \mathbf{A}(t)\rangle e^{-i \int_{-\infty}^t dt' \frac{1}{2} [\mathbf{p} + \mathbf{A}(t')]^2}. \quad (18)$$

Here  $|\mathbf{p}\rangle$  denotes the plane wave state

$$\langle \mathbf{r} | \mathbf{p} \rangle = \frac{1}{(2\pi)^{3/2}} e^{i\mathbf{p}\mathbf{r}}, \quad (19)$$

and  $\mathbf{A}(t)$  is the vector potential of the laser field

$$\mathbf{A}(t) = - \int_{-\infty}^t dt' \mathbf{E}(t'). \quad (20)$$

The time evolution operator corresponding to  $H_F(t)$  can be constructed by Volkov states

$$U_F(t, t') = \int d^3p |\chi_{\mathbf{p}}(t)\rangle \langle \chi_{\mathbf{p}}(t')|. \quad (21)$$

The operator  $U(t, t')$  satisfies the Dyson equation

$$U(t, t') = U_F(t, t') - i \int_{t'}^t dt'' U_F(t, t'') V U(t'', t'). \quad (22)$$

In the strong field regime, the electron-core potential  $V(\mathbf{r})$  can be treated as a small perturbation for the electron in the continuum. In the lowest order approximation, equation (22) is

$$U(t, t') = U_F(t, t'). \quad (23)$$

In essence, within the above approximation, the electron in the continuum is treated as a free particle moving in the strong laser field. Equation (15) is then reduced to

$$\begin{aligned} \mathbf{D}(t) &= -i \int_{-\infty}^t dt' e^{-i p t'} \langle g | \mathbf{r} U_F(t, t') \mathbf{r} \cdot \mathbf{E}(t') e^{i p t'} | g \rangle + \text{c.c.} \\ &= -i \int_{-\infty}^t dt' \int d^3 p e^{-i p t'} \langle g | \mathbf{r} | \chi_{\mathbf{p}}(t) \rangle \\ &\quad \times \langle \chi_{\mathbf{p}}(t') | \mathbf{r} \cdot \mathbf{E}(t') e^{i p t'} | g \rangle + \text{c.c.} \\ &= -i \int_{-\infty}^t dt' \int d^3 p e^{-i p t'} \langle g | \mathbf{r} | \mathbf{p} + \mathbf{A}(t) \rangle \\ &\quad \times \mathbf{E}(t') \cdot \langle \mathbf{p} + \mathbf{A}(t') | \mathbf{r} | g \rangle e^{i p t'} \\ &\quad \times e^{-i \int_{t'}^t dt'' \frac{1}{2} [\mathbf{p} + \mathbf{A}(t'')]^2} + \text{c.c.} \end{aligned} \quad (24)$$

$$\begin{aligned} &= -i \int_{-\infty}^t dt' \int d^3 p d^* (\mathbf{p} + \mathbf{A}(t)) \mathbf{E}(t') \\ &\quad \cdot d(\mathbf{p} + \mathbf{A}(t')) e^{-i S(\mathbf{p}, t, t')} + \text{c.c.} \end{aligned} \quad (25)$$

In equation (25),  $\mathbf{d}(\mathbf{p}) = \langle \mathbf{p} | \mathbf{r} | g \rangle$  is the dipole matrix element for the bound-free transition where  $|\mathbf{p}\rangle$  denotes the plane wave state, and the phase factor

$$\begin{aligned} S(\mathbf{p}, t, t') &= \int_{t'}^t dt'' \frac{1}{2} [\mathbf{p} + \mathbf{A}(t'')]^2 + I_p(t - t') \\ &= \int_{t'}^t dt'' \left( \frac{1}{2} [\mathbf{p} + \mathbf{A}(t'')]^2 + I_p \right). \end{aligned} \quad (26)$$

The integral in equation (24) has a simple and intuitive interpretation which corresponds to the quasi-classical three step model [17, 20]:  $\mathbf{p}$  can be treated as the classical canonical momentum, since the electron-ion interaction is neglected for the continuum electron,  $\mathbf{p}$  turns into a conserved quantity;  $\mathbf{p} + \mathbf{A}(t)$  can be assumed as the instantaneous velocity at time  $t$ ; the factor  $\mathbf{E}(t') \cdot \langle \mathbf{p} + \mathbf{A}(t') | \mathbf{r} | g \rangle e^{i p t'}$  describes the ionization process which occurs at time  $t'$  while  $e^{-i p t'} \langle g | \mathbf{r} | \mathbf{p} + \mathbf{A}(t) \rangle$  determines the amplitude of photo-recombination at time  $t$ ; the factor  $e^{-i \int_{t'}^t dt'' \frac{1}{2} [\mathbf{p} + \mathbf{A}(t'')]^2}$  is the phase accumulated from  $t'$  to  $t$  while the electron propagating in the continuum; at a given recombination (or photon emission) time  $t$  the induced dipole is obtained by integrating over the contributions from all ionization time  $t' < t$  and all canonical momentum  $\mathbf{p}$ . The factor  $S(\mathbf{p}, t, t')$  in equation (25) is often referred to as the quasi-classical action but it also incorporates some effects of the ionization and recombination process through its dependence on  $I_p$ , see equation (26). The complex conjugate part in the dipole moment is the time reversal of the above three-step process which is a pure quantum contribution and has no classical interpretation.

In practice the SFA form of equation (25) is rarely used. Instead, a simpler form, based on the saddle point approximation for the integral over 3D momentum in equation (25), has been used more often. This will be discussed in the next subsection.

**2.1.2. Lewenstein model in the saddle-point approximation for 3D integral over momentum and its accuracy.** Before going to the main content in this subsection we briefly give here a formal description of the saddle point approximation from a mathematical point of view, adapted from [75, 76]. First consider a one-dimensional integral

$$I = \int_{-\infty}^{\infty} d\omega E(\omega) e^{i f(\omega)}, \quad (27)$$

where  $E(\omega)$  is a smooth amplitude and  $e^{i f(\omega)}$  is a phase function varying much faster than  $E(\omega)$ . Since all the fast oscillating part have little contribution to the integral,  $I$  is dominated by the integrand close to the saddle point  $\omega_s$  given by the saddle point equation

$$f'(\omega_s) = 0, \quad (28)$$

in which  $f'$  denotes the first derivative of  $f$ . In general there are a set of saddle points satisfying this equation. Using the truncated Taylor expansion in the vicinity of  $\omega_s$  up to the second order one can obtain the saddle point approximation

$$I \approx \sum_s \sqrt{\frac{2\pi i}{f''(\omega_s)}} E(\omega_s) e^{i f(\omega_s)}, \quad (29)$$

where  $f''$  is the second derivative of  $f$ . The summation runs over all the saddle points labeled by  $s$ . Equation (29) is based on the assumption that in the Taylor expansion of  $f(\omega)$  near  $\omega_s$  the second order term is dominant over higher order terms. This may become invalid when  $f''(\omega_s)$  happens to be zero, which will yield an artificial divergence in equation (29). This divergence is not real and could be removed by including the third order term in the Taylor expansion.

Similarly the saddle point approximation can be applied to a  $n$ -dimensional integral as the following

$$\int d^n \omega E(\omega) e^{i f(\omega)} \approx \sum_s \sqrt{\frac{(2\pi i)^n}{\det(f''(\omega_s))}} E(\omega_s) e^{i f(\omega_s)}. \quad (30)$$

In equation (30) the saddle point  $\omega_s$  is determined by the saddle point equation

$$\nabla_{\omega} f(\omega_s) = 0, \quad (31)$$

and  $f''(\omega_s) = \nabla_{\omega} \nabla_{\omega} f(\omega_s)$  is the  $n \times n$  Hessian matrix at the saddle point  $\omega_s$ .

Now let us investigate the dependence of the integrand in equation (25) on  $\mathbf{p}$ . The action  $S(\mathbf{p}, t, t')$  varies on a characteristic scale  $p^2/2 \simeq 1/(t - t')$ . If we approximate  $t - t'$  as the optical period of an 800 nm laser i.e.  $t - t' \simeq 2.6$  fs, we can get  $p^2/2 \simeq 0.25$  eV. Provided that the dipole matrix element  $\mathbf{d}(\mathbf{p})$  changes much slower than this energy scale the integrand in front of  $e^{-iS}$  can be treated as a smooth function while  $e^{-iS}$  yields a very strong oscillation. Thus one can apply the saddle-point method to estimate this integral over  $\mathbf{p}$ . In most cases  $\mathbf{d}(\mathbf{p})$  changes smoothly over tens of electron volts so that the saddle point approximation is guaranteed, except for molecules with very large internuclear separations (typically tens of atomic units) [77]. This discussion also shows that the saddle point approximation should get more accurate for longer wavelengths.

We now apply the saddle point approximation to the 3D integral over momentum in equation (25). The saddle point in equation (31) for  $\mathbf{p}$  in our case can be written in a vector form as

$$\begin{aligned}\nabla_{\mathbf{p}}S(\mathbf{p}, t, t') &= \nabla_{\mathbf{p}} \int_{t'}^t dt'' \left( \frac{1}{2} [\mathbf{p} + \mathbf{A}(t'')]^2 + I_p \right) \\ &= \int_{t'}^t dt'' \nabla_{\mathbf{p}} [\mathbf{p} + \mathbf{A}(t'')] \cdot [\mathbf{p} + \mathbf{A}(t'')] \\ &= \int_{t'}^t [\mathbf{p} + \mathbf{A}(t'')] dt'' = 0,\end{aligned}\quad (32)$$

which gives the saddle point solution  $\mathbf{p}_s$  as

$$\mathbf{p}_s = -\frac{1}{t-t'} \int_{t'}^t \mathbf{A}(t'') dt''. \quad (33)$$

Since  $\nabla_{\mathbf{p}}S(\mathbf{p}, t, t') = \int_{t'}^t \mathbf{v}(t'') dt'' = \mathbf{r}(t) - \mathbf{r}(t')$ , the semi-classical interpretation of equation (32) is clear: the dominant contribution to the HHG photon emission comes from the trajectory with canonical momentum  $\mathbf{p}_s$  such that the electron born at time  $t'$  returns to the same position at time  $t$ .

The Hessian matrix of  $S(\mathbf{p}, t, t')$  is given by

$$\begin{aligned}\nabla_{\mathbf{p}} \nabla_{\mathbf{p}} S(\mathbf{p}, t, t') &= \int_{t'}^t \nabla_{\mathbf{p}} [\mathbf{p} + \mathbf{A}(t'')] dt'' \\ &= (t-t') \mathbf{I},\end{aligned}\quad (34)$$

where  $\mathbf{I}$  is the  $3 \times 3$  unit matrix.

By using equation (30) the saddle-point approximation of equation (25) can be written as

$$\begin{aligned}\mathbf{D}(t) &= -i \int_{-\infty}^t dt' \sqrt{\frac{(2\pi i)^3}{\det(-(t-t')\mathbf{I})}} \mathbf{d}^*(\mathbf{p}_s + \mathbf{A}(t)) \mathbf{E}(t') \\ &\quad \cdot \mathbf{d}(\mathbf{p}_s + \mathbf{A}(t')) e^{-iS(\mathbf{p}_s, t, t')} + \text{c.c.} \\ &= -i \int_{-\infty}^t dt' \left( \frac{-2\pi i}{t-t'-i\epsilon} \right)^{3/2} \mathbf{d}^*(\mathbf{p}_s + \mathbf{A}(t)) \mathbf{E}(t') \\ &\quad \cdot \mathbf{d}(\mathbf{p}_s + \mathbf{A}(t')) e^{-iS(\mathbf{p}_s, t, t')} + \text{c.c.}\end{aligned}\quad (35)$$

Here  $\epsilon$  is an arbitrary small positive regularization constant introduced to smooth out the singularity. The saddle-point approximation for the integral over  $\mathbf{p}$  yields a factor  $(t-t')^{-3/2}$  which accounts for the quantum diffusion effect, i.e., the spread of the wave packet of the continuum electron. Larger excursion time in the continuum will have less contribution to the harmonic emission.

Consider the case that the electric field is linearly polarized along the  $x$ -axis. Equation (33) shows that  $\mathbf{p}_s$  is also along the  $x$ -axis. Equation (35) for  $D_x(t)$  reduces to a one-dimensional equation

$$\begin{aligned}D_x(t) &= -i \int_{-\infty}^t dt' \left( \frac{-2\pi i}{t-t'-i\epsilon} \right)^{3/2} d_x^*(p_s + A(t)) \\ &\quad \times d_x(p_s + A(t')) E(t') e^{-iS(p_s, t, t')} + \text{c.c.}\end{aligned}\quad (36)$$

in which  $d_x(p) = \langle p \mathbf{e}_x | x | g \rangle$  is the  $x$  component of the dipole transition matrix element from the ground state to the plane wave state propagating along  $x$  axis with momentum  $p$ .

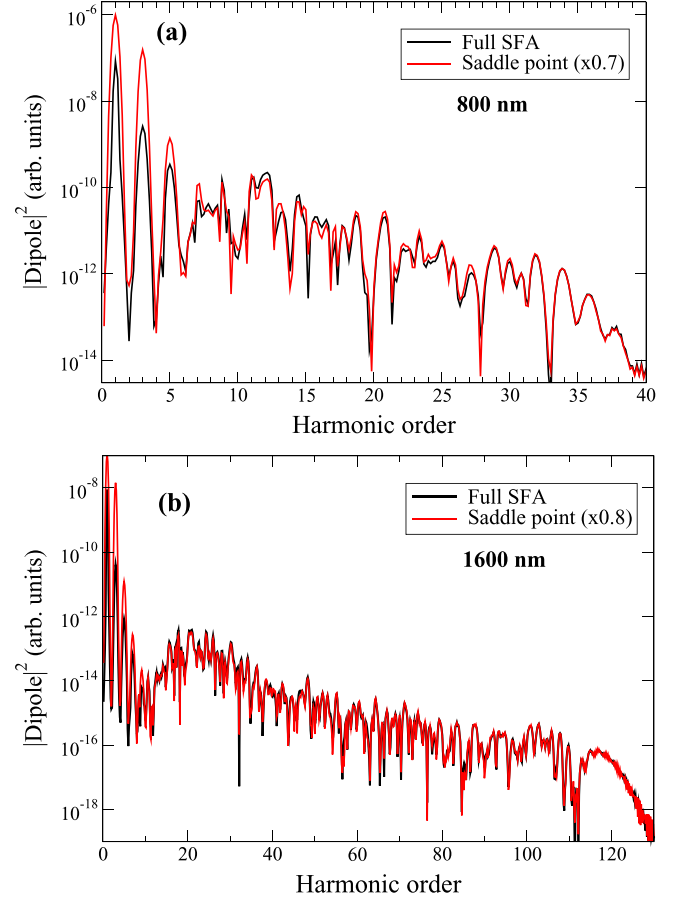


**Figure 1.** (a) Induced dipole vs harmonic order from the full SFA and saddle point approximation using equation (36) for hydrogen. Cosine-squared envelope laser pulse with 6-cycle total duration, 800 nm wavelength,  $2.0 \times 10^{14} \text{ W cm}^{-2}$  peak intensity is used. (b), same as (a), but for 1600 nm and  $1.0 \times 10^{14} \text{ W cm}^{-2}$ .

Equations (25), (35), and (36) are the standard equations in the SFA (or the Lewenstein model) for the laser induced dipole moment. To account for the ground state depletion a damping factor  $a(t)$  is introduced [20]. This factor is often calculated by using the Ammosov–Delone–Krainov (ADK) theory [46, 78]. Different attempts to go beyond this model have been proposed. We will discuss some of these extensions in section 2.4.

To judge about the quality of the saddle point approximation, we now compare the SFA result using equation (36) with that of the full SFA of equation (25), in which integration over 3D momentum is carried out numerically. The comparison of HHG spectra is shown in figure 1(a) and (b) for hydrogen atom with 800 nm and 1600 nm wavelength, respectively. Clearly, the two methods agree very well, although we have to rescale the result with the saddle-point approximation by a factor of 0.7 for the 800 nm case and 0.8 for the 1600 nm case. This scaling factor is quite typical in the applications of the saddle point approximation [26]. The saddle point approximation become less accurate only at very low harmonics below the threshold. Overall the accuracy is improved with increased laser wavelength at similar range of laser intensity, as expected.

In the rest of this tutorial, we will imply equation (36) when we refer to the SFA.

## 2.2. Quantum orbits theory

**2.2.1. Formulation and basic equations.** Equation (36) shows the time dependent dipole moment induced by the laser field. The HHG power spectrum is given by

$$P(\omega) \propto \omega^4 |D_x(\omega)|^2, \quad (37)$$

in which  $\omega$  is the harmonic photon energy.  $D_x(\omega)$  is the Fourier transform of  $D_x(t)$

$$D_x(\omega) = \int_{-\infty}^{\infty} D_x(t) e^{i\omega t} dt = D_x^{(+)}(\omega) + [D_x^{(+)}(-\omega)]^*, \quad (38)$$

where

$$D_x^{(+)}(\omega) = -i \int_{-\infty}^{\infty} dt \int_{-\infty}^t dt' \left( \frac{-2\pi i}{t-t'-i\epsilon} \right)^{3/2} \times d_x^*(p_s + A(t)) d_x(p_s + A(t')) \times E(t') e^{-i\Theta(p_s, t, t')}. \quad (39)$$

In the above equation

$$\Theta(p_s, t, t') = S(p_s, t, t') - \omega t, \quad (40)$$

$$S(p_s, t, t') = \int_{t'}^t dt'' \left( \frac{1}{2} [p_s + A(t'')]^2 + I_p \right), \quad (41)$$

and

$$p_s = -\frac{1}{t-t'} \int_{t'}^t A(t'') dt''. \quad (42)$$

The basic idea of the QO theory is to further apply the saddle-point approximation to the two-dimensional integral over  $t$  and  $t'$  [20, 44]. Saddle point equations for  $t$  and  $t'$  reads

$$\begin{aligned} \frac{\partial \Theta}{\partial t'} &= \frac{\partial S}{\partial t'} = -\frac{1}{2} [p_s + A(t')]^2 - I_p = 0 \\ &\Rightarrow \frac{1}{2} [p_s + A(t')]^2 = -I_p, \end{aligned} \quad (43)$$

$$\begin{aligned} \frac{\partial \Theta}{\partial t} &= \frac{\partial S}{\partial t} - \omega = \frac{1}{2} [p_s + A(t)]^2 + I_p - \omega = 0 \\ &\Rightarrow \frac{1}{2} [p_s + A(t)]^2 = \omega - I_p. \end{aligned} \quad (44)$$

Equation (43) implies that when the electron is born to the continuum, the ‘kinetic energy’ is a negative value  $-I_p$ , which accounts for the quantum effect of tunneling ionization. Equation (44) describes energy conservation when the electron recombines with the ionic core. Upon recombination the electron returns to the ground state and emits a photon with energy  $\omega$ . For a given  $\omega$  one can solve equations (43) and (44) (with  $p_s$  given in (42)) simultaneously to find a series of saddle points  $(t'_s, t_s)$ . Due to the constraint imposed by equation (43) both the solutions  $t'_s$  and  $t_s$  are complex-valued.

Each solution  $(t'_s, t_s)$  determines a unique ‘quantum-orbit’ which can be viewed as an extension of the classical-orbit of an electron moving in the electric field [43, 44]. The saddle-point approximation of equation (39) reads

$$D_x^{(+)}(\omega) = -i \sum_s \sqrt{\frac{(2\pi i)^2}{\det(\Theta'')}} \left( \frac{-2\pi i}{t_s - t'_s} \right)^{3/2} \times d_x^*(p_s + A(t_s)) d_x(p_s + A(t'_s)) \times E(t'_s) e^{-i\Theta(p_s, t_s, t'_s)}. \quad (45)$$

In the spirit of Feynman’s path integrals [42],  $D_x^{(+)}(\omega)$  is a superposition of the contribution from individual quantum-orbit weighted by  $e^{-i\Theta(p_s, t_s, t'_s)}$ . The quantum-orbit that corresponds to negative  $\omega$  does not have any classical counterpart and will have little contribution. For this reason in a typical quantum orbits calculation, the second term on the right hand side of equation (38) is dropped, i.e.

$$D_x(\omega) \approx D_x^{(+)}(\omega) = \sum_s D_{xs}(\omega), \quad (46)$$

where  $D_{xs}(\omega)$  denotes the induced dipole moment by an individual quantum-orbit

$$D_{xs}(\omega) = \frac{2\pi}{\sqrt{\det(S'')}} \left( \frac{-2\pi i}{t_s - t'_s} \right)^{3/2} d_x^*(p_s + A(t_s)) \times d_x(p_s + A(t'_s)) E(t'_s) e^{-i\Theta(p_s, t_s, t'_s)}. \quad (47)$$

Here  $2 \times 2$  Hessian matrix  $S''$  is given as

$$S'' = \begin{pmatrix} \frac{\partial^2 S(p_s, t, t')}{\partial t^2} & \frac{\partial^2 S(p_s, t, t')}{\partial t \partial t'} \\ \frac{\partial^2 S(p_s, t, t')}{\partial t' \partial t} & \frac{\partial^2 S(p_s, t, t')}{\partial t'^2} \end{pmatrix}_{t=t_s, t'=t'_s}. \quad (48)$$

In equation (46) only the quantum orbits leading to negative  $\text{Im}\{\Theta\}$  are included in order to obtain converged results.

From equations (41) and (42) one can obtain

$$\left. \frac{\partial^2 S}{\partial t^2} \right|_{t_s, t'_s} = -\frac{[p_s + A(t_s)]^2}{t_s - t'_s} - E(t_s)[p_s + A(t_s)], \quad (49)$$

$$\left. \frac{\partial^2 S}{\partial t'^2} \right|_{t_s, t'_s} = -\frac{[p_s + A(t'_s)]^2}{t_s - t'_s} + E(t'_s)[p_s + A(t'_s)], \quad (50)$$

$$\left. \frac{\partial^2 S}{\partial t \partial t'} \right|_{t_s, t'_s} = \left. \frac{\partial^2 S}{\partial t' \partial t} \right|_{t_s, t'_s} = \frac{[p_s + A(t_s)][p_s + A(t'_s)]}{t_s - t'_s}. \quad (51)$$

Note that the form of QO equation (47) is strictly valid only when there is no singularity of the transition dipole at the solutions  $t'_s$  of equation (43). Such a singularity actually occurs if the target is a hydrogen atom. We will come back to this point in section 2.3.2.

2.2.2. *Factorization in the quantum-orbit theory.* From equations (43) and (44) it follows that

$$d_x(p_s + A(t'_s)) = \varepsilon'_s d_x(i\sqrt{2I_p}), \quad (52)$$

$$d_x(p_s + A(t_s)) = \varepsilon_s d_x\left(\sqrt{2(\omega - I_p)}\right). \quad (53)$$

For a particular quantum-orbit labeled by  $(t'_s, t_s)$ , the phase factor  $\varepsilon'_s$  (or  $\varepsilon_s$ ) may be either +1 or -1, to account for the direction of the electron momentum at the moment of ionization (or recombination). Note that we focus only on above-threshold harmonics (i.e., with  $\omega > I_p$ ). For harmonics below the threshold, the accuracy of saddle point-approximation in the 3D integration over momentum is questionable (see section 2.1.2), causing the QO to be inadequate. Therefore the induced dipole  $D_x(\omega)$  can be rewritten as

$$\begin{aligned} D_x(\omega) &= d_x^*\left(\sqrt{2(\omega - I_p)}\right) d_x(i\sqrt{2I_p}) \\ &\times \sum_s \frac{2\pi\varepsilon'_s\varepsilon_s}{\sqrt{\det(S'')}} \left(\frac{-2\pi i}{t_s - t'_s}\right)^{3/2} E(t'_s) e^{-i\Theta(p_s, t_s, t'_s)} \\ &\equiv d_x^*\left(\sqrt{2(\omega - I_p)}\right) w(\omega). \end{aligned} \quad (54)$$

Equation (54) clearly shows the factorization of HHG dipole  $D_x(\omega)$  into two factors: the complex conjugate of the bound-free dipole transition matrix element  $d_x(p)$  and a complex ‘returning electron wave packet’  $w(\omega)$ . The latter combines the ionization step and the propagation of continuum electron in the laser field from ionization time  $t'_s$  until recombination time  $t_s$ . Note that we have absorbed the phase factor  $\varepsilon_s$  into the wave packet, to account for contribution from all possible trajectories. Clearly, we can easily identify contribution of each trajectory in the electron wave packet. We emphasize that the recombination step enters equation (54) in the field-free form and all the laser-dependent features are in the wave packet. The wave packet depends on the structure, apart from the ionization potential, only through a  $\omega$ -independent  $d_x(i\sqrt{2I_p})$  at the exit of the tunneling ionization (see equation (43)). In this derivation, the factorization is valid for harmonics above the threshold, i.e.  $\omega > I_p$ . We will further discuss the electron wave packet in section 2.3.2.

We remark that the saddle point equations (33), (43), and (44) are the same for different atomic and molecular targets, as long as the assumptions for the QO are valid. Different targets differ only by their transition dipole matrix elements and ionization potentials. Therefore the above derivation is quite general and can be extended in a straightforward manner to molecular targets. For simplicity, let us consider a linear molecule, aligned along the  $x$ -axis, in a laser field  $E(t)$ , linearly polarized on the  $x - y$  plane with an angle  $\theta$  with respect to the molecular axis. The parallel component of HHG

dipole can be written as [46]

$$\begin{aligned} D_{\parallel}(t) &= -i \int_{-\infty}^{t'} dt' \left(\frac{-2\pi i}{t - t' - i\epsilon}\right)^{3/2} \hat{e} \cdot d^*[(p_s + A(t))\hat{e}] \\ &\times \left\{ \cos \theta d_x[(p_s + A(t'))\hat{e}] \right. \\ &\quad \left. + \sin \theta d_y[(p_s + A(t'))\hat{e}] \right\} \\ &\times E(t') e^{-iS(p_s, t, t')} + \text{c.c.} \end{aligned} \quad (55)$$

with  $\hat{e}$  being the unit vector along laser polarization. Here we assume that saddle-point integration over intermediate momentum  $\mathbf{p}$  has been carried out [see, equation (36)]. Following the QO derivation, we arrive at

$$D_{\parallel}(\omega) = \hat{e} \cdot d^*\left(\sqrt{2(\omega - I_p)}\hat{e}\right) w^m(\theta, \omega). \quad (56)$$

Here  $w^m$  is defined as in equation (54), but with a factor  $d_x(i\sqrt{2I_p})$  replaced by  $\hat{e} \cdot d(i\sqrt{2I_p}\hat{e}) = \cos \theta d_x(i\sqrt{2I_p}\hat{e}) + \sin \theta d_y(i\sqrt{2I_p}\hat{e})$ . For every fixed  $\theta$  this factor only gives an overall coefficient to the wave packet. An equation similar to equation (56) can be written for the perpendicular component with the same  $w^m$  and  $\hat{e} \cdot d^*$  being replaced by  $\hat{e}_{\perp} \cdot d^*$ .

We further note that the factorization is not limited to the case with a single color laser. Indeed, for a synthesized pulse, as long as the saddle-point approximation is applicable, the specific forms of equations (33), (43) and (44) are only modified by the form of the vector potential  $\mathbf{A}$ , but the formal derivation of the factorization remains the same. This remark also applies to different forms of the SFA dipole such as dipole acceleration and velocity forms. We will further illustrate this point in section 2.3.2.

The validity of this factorization in the QO theory implies approximate factorization in the SFA, which was found numerically in [59]. More importantly, the factorization equation (54) can be utilized to ‘extrapolate’ to real atomic and molecular targets with long range Coulomb interaction. More specifically, one speculates that each factor in equation (54) can be put in ‘by hand’ with more accurate expressions that are beyond the assumptions used in the SFA and QO. In fact, this speculation has been verified by numerical solution of the TDSE [45, 47], which serves as the basis for the recently proposed QRS theory [12, 46]. We will come back to this point in section 2.3.

2.2.3. *Analytical QO theory of HHG by monochromatic laser fields.* a. *Sub-cycle dynamics of high-order harmonic emission* In this subsection we consider harmonic emission by a monochromatic laser field within the QO theory where the laser-induced dipole can be calculated analytically. The laser field is given by  $E(t) = E_0 \cos(\omega_L t)$  (This is also called the adiabatic approximation [44]). Here  $\omega_L$  is the frequency of the driving laser, and the optical period is  $T_L = 2\pi/\omega_L$ . Due to the periodicity we can expect the time dependent dipole

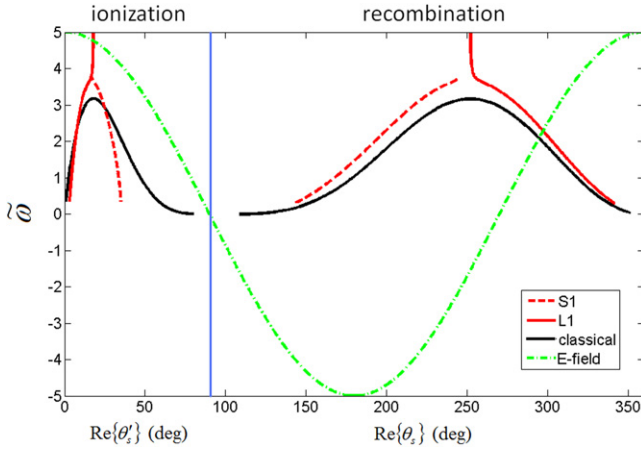


**Figure 2.** Red (or medium grey): the real part of ionization time and recombination time for S1 (dashed) and L1 (solid) as functions of  $\tilde{\omega}$ , obtained from equations (66) and (67) with parameters: 800 nm wavelength,  $1.5 \times 10^{14} \text{W cm}^{-2}$  peak intensity, argon target ( $\gamma = 0.94$ ). Solid black: classical born and return time calculated from equations (68) and (69). Dot-dashed green (or light grey): profile of the electric field.

moment has the following property

$$D_x\left(t + \frac{T_L}{2}\right) = -D_x(t). \quad (57)$$

Thus  $D_x(t)$  can be expressed as

$$D_x(t) = \sum_{n=-\infty}^{\infty} (-1)^n \tilde{D}_x\left(t + n\frac{T_L}{2}\right), \quad (58)$$

in which

$$\tilde{D}_x(t) = \begin{cases} D_x(t) & -\frac{T_L}{4} < t \leq \frac{T_L}{4} \\ 0 & \text{other } t \end{cases} \quad (59)$$

is the dipole moment within one half optical cycle. Its Fourier transform

$$\tilde{D}_x(\omega) = \int_{-\infty}^{\infty} \tilde{D}_x(t) e^{i\omega t} dt = \int_{-\frac{T_L}{4}}^{\frac{T_L}{4}} D_x(t) e^{i\omega t} dt \quad (60)$$

leads to a continuous spectrum.

The spectrum of the whole dipole moment can be expressed by

$$\begin{aligned} D_x(\omega) &= \sum_{n=-\infty}^{\infty} (-1)^n \int_{-\infty}^{\infty} \tilde{D}_x\left(t + n\frac{T_L}{2}\right) e^{i\omega t} dt \\ &= \tilde{D}_x(\omega) \left[ \sum_{n=-\infty}^{\infty} (-1)^n e^{-i\omega n \frac{T_L}{2}} \right] \\ &= \tilde{D}_x(\omega) \left[ \sum_{n=-\infty}^{\infty} e^{i\pi n} e^{-i\omega n \frac{T_L}{2}} \right] \end{aligned}$$

$$\begin{aligned} &= \tilde{D}_x(\omega) \left[ \sum_{n=-\infty}^{\infty} e^{-i\frac{2\pi n}{T_L} \left(\frac{\omega}{2} - \frac{\omega_L}{2}\right)} \right] \\ &= \tilde{D}_x(\omega) \left[ \sum_{k=-\infty}^{\infty} \omega_L \delta\left(\frac{\omega}{2} - \frac{\omega_L}{2} - k\omega_L\right) \right] \\ &= \tilde{D}_x(\omega) \left[ \sum_{k=-\infty}^{\infty} 2\omega_L \delta\left(\omega - (2k+1)\omega_L\right) \right] \\ &= \sum_{\substack{q=-\infty \\ \text{odd } q}}^{\infty} 2\omega_L \delta\left(\omega - q\omega_L\right) \tilde{D}_x(q\omega_L). \end{aligned} \quad (61)$$

Equation (61) shows that the spectrum induced by a monochromatic laser field contains only odd harmonics of the fundamental frequency  $\omega_L$ . These harmonics is fully determined by the induced dipole moment within half optical cycle. Therefore in the following discussion we focus mainly on the sub-cycle dynamics. In the quantum orbits analysis only the orbit that has a ionization time (often called born time) within the half optical cycle,  $(-T_L/4, T_L/4)$ , has to be considered.

*b. Real parts of born time and recombination time: QO versus classical picture.* For a monochromatic electric field,

$$A(t) = - \int E_0 \cos(\omega_L t') dt' = -\frac{E_0}{\omega_L} \sin(\omega_L t), \quad (62)$$

and

$$\begin{aligned} p_s &= -\frac{1}{t-t'} \int_{t'}^t A(t'') dt'' \\ &= -\frac{E_0}{\omega_L} \left( \frac{\cos(\omega_L t) - \cos(\omega_L t')}{\omega_L t - \omega_L t'} \right). \end{aligned} \quad (63)$$

The saddle point equations (43) and (44) now become

$$\left(\frac{E_0}{\omega_L}\right)^2 \left( \frac{\cos(\omega_L t) - \cos(\omega_L t')}{\omega_L t - \omega_L t'} + \sin(\omega_L t') \right)^2 = -2I_p, \quad (64)$$

$$\left(\frac{E_0}{\omega_L}\right)^2 \left( \frac{\cos(\omega_L t) - \cos(\omega_L t')}{\omega_L t - \omega_L t'} + \sin(\omega_L t) \right)^2 = 2(\omega - I_p). \quad (65)$$

By introducing the ponderomotive energy  $U_p = \frac{E_0^2}{4\omega_L^2}$ , the equations above can be rewritten as

$$\left( \frac{\cos \theta - \cos \theta'}{\theta - \theta'} + \sin \theta' \right)^2 = -\frac{I_p}{2U_p} = -\gamma^2, \quad (66)$$

$$\left( \frac{\cos \theta - \cos \theta'}{\theta - \theta'} + \sin \theta \right)^2 = \frac{(\omega - I_p)}{2U_p} = \frac{\tilde{\omega}}{2}, \quad (67)$$

where  $\theta' = \omega_L t'$ ,  $\theta = \omega_L t$  are the born and return time scaled by the optical period,  $\gamma = \sqrt{\frac{I_p}{2U_p}}$  is the Keldysh parameter and  $\tilde{\omega} = \frac{\omega - I_p}{U_p}$  can be interpreted as the kinetic energy of the returning electron scaled by the ponderomotive energy. By

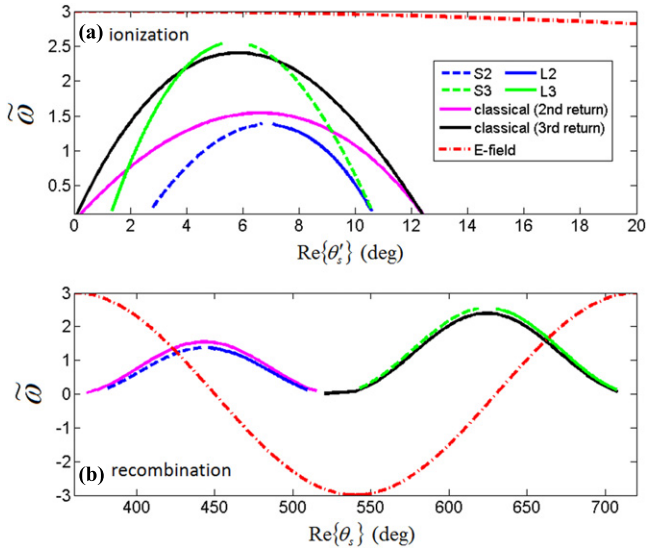


**Figure 3.** The real part of (a) ionization time and (b) recombination time for higher order returns as functions of  $\tilde{\omega}$  calculated from both quantum orbits and classical equations. The parameters are the same as in figure 2.

including the quantum origin of the tunneling process, the solutions  $\theta'_s$  and  $\theta_s$  are all complex values.

The simple classical model assumes the electron is born with zero kinetic energy, which is equivalent to  $\gamma = 0$ . Then equations (66) and (67) reduce into

$$(\cos \theta_c - \cos \theta'_c) + (\theta_c - \theta'_c) \sin \theta'_c = 0, \quad (68)$$

$$2(\sin \theta_c - \sin \theta'_c)^2 = \tilde{\omega}. \quad (69)$$

In this classical picture  $\theta'_c$  and  $\theta_c$  are all real quantities. We can expect that real parts of quantum-orbit solutions  $\text{Re}\{\theta'_s\}$  and  $\text{Re}\{\theta_s\}$  are counterparts of the classical born and return time and will approach them as  $\gamma \rightarrow 0$ .

In the classical picture, as shown in figures 2 and 3, the electron born before the peak field ( $-90^\circ < \theta' < 0^\circ$ ) will not return to the core. The electron born after the peak field ( $0^\circ \leq \theta' < 90^\circ$ ) has a chance to revisit the core with kinetic energy  $\tilde{\omega}U_p$ . Moreover, the electron born in the region  $0^\circ \leq \theta' < 12^\circ$  may revisit its core more than once, which is often named higher order returns. The recombination time for the first return roughly lies in  $110^\circ \leq \theta < 360^\circ$ , for the second return  $360^\circ \leq \theta < 540^\circ$ , for the third return  $540^\circ \leq \theta < 720^\circ$ . Each return has its maximum return energy (cutoff) such as  $\tilde{\omega} = 3.2$  for the first return ( $\theta' = 17^\circ$  correspondingly),  $\tilde{\omega} = 1.5$  for the second,  $\tilde{\omega} = 2.4$  for the third. The overall cutoff of the HHG is dominated by the first return, i.e.  $\omega_{\text{cutoff}} \approx 3.2U_p + I_p$ . In each return the orbit that has a particular return energy  $\tilde{\omega}$  below cutoff splits into two branches: the orbit which returns earlier is named ‘short’ orbit while that returns later is named ‘long’ orbit. For odd-number returns (the first, third, fifth ...) the electron born earlier will follow the long orbit, however for even-number returns (the second, fourth, ...) the electron born earlier will follow the short orbit. In our discussion the label

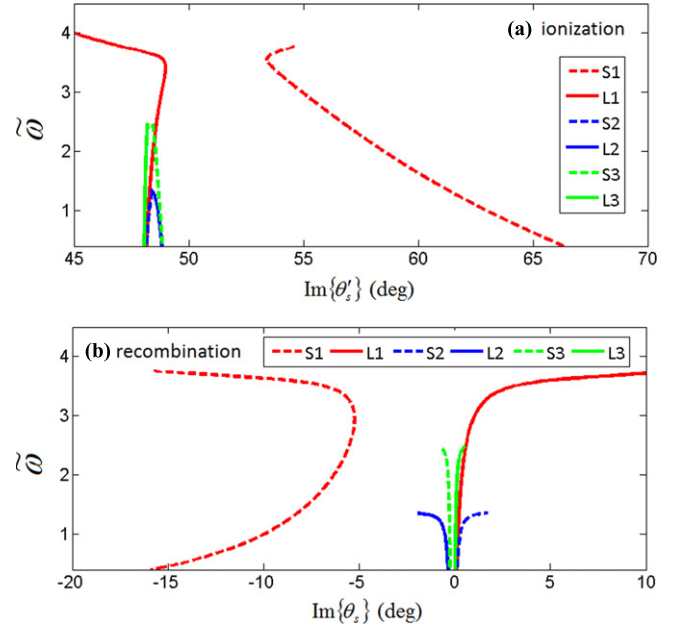


**Figure 4.** (a)  $\text{Im}\{\theta'_s\}$  and (b)  $\text{Im}\{\theta_s\}$  for quantum orbits up to the third return as functions of  $\tilde{\omega}$  calculated from equations (66) and (67). The parameters are the same as in figure 2.

‘S1’ refers to the short orbit in the first return, ‘L1’ refers to the long orbit in the first return and so forth.

Figures 2 and 3 show that the quantum-orbit solutions  $\text{Re}\{\theta'_s\}$  and  $\text{Re}\{\theta_s\}$  (at  $\gamma = 0.94$ ) in general agree with the classical quantities  $\theta'_c$  and  $\theta_c$ . However our example also illustrates some discrepancies between them. The time interval of ionization given by the QO is always narrower than the classical prediction, in particular, the born interval of the S1 orbit is reduced to  $17^\circ < \theta' < 35^\circ$ . Compared to the classical result, the cutoff of the first return is extended to  $\tilde{\omega} = 3.8$  due to quantum tunneling and diffusion [20, 44], and the cutoff of the third return is also increased, while the cutoff of the second return is decreased.

*c. Imaginary parts of born time and recombination time in the QO.* The imaginary part of the born time  $\text{Im}\{\theta'_s\}$  is a direct consequence of the quantum tunneling. As we shall discuss in section 3.1,  $\text{Im}\{\theta'_s\}$  may be interpreted as the time required for the electron to tunnel through the barrier [79]. This tunneling time mainly depends on  $I_p$  and the field strength when the electron is born. As figure 4(a) shows,  $\text{Im}\{\theta'_s\}$  for all orbits except S1 are very close to each other, because these orbits are all born in a narrow time interval right after the peak field so that the electric field at their born time are almost the same. On the contrary the S1 orbit is born later so that the corresponding electric field is much weaker, which leads to a longer tunneling time. Figure 4(b) shows that the imaginary part of the return time  $\text{Im}\{\theta_s\}$  is close to zero for all orbits except S1. In other words, for the orbits with long excursion time the recombination is well separated from tunneling so  $\theta_s$  is dominated by the real classical recombination time. On the contrary, for the S1 orbit, especially at low energies  $\tilde{\omega} \leq 2$ , the excursion time is relatively small so that

the recombination feels the influence of the quantum nature of the tunneling ionization, which gives rise to the nonzero imaginary return time.

#### 2.2.4. The amplitude and phase of high-order harmonics.

From equations (40) and (41) the factor  $\Theta$  corresponding to the saddle point solution  $(t'_s, t_s)$  can be derived as follows:

$$\begin{aligned}
 \Theta_s &= \int_{t'_s}^{t_s} dt'' \left( \frac{1}{2} [p_s + A(t'')]^2 + I_p \right) - \omega t_s \\
 &= I_p (t_s - t'_s) + \frac{1}{2} p_s^2 (t_s - t'_s) + p_s \int_{t'_s}^{t_s} A(t'') dt'' \\
 &\quad + \frac{E_0^2}{2\omega_L^2} \int_{t'_s}^{t_s} \sin^2(\omega_L t'') dt'' - \omega t_s \\
 &= I_p (t_s - t'_s) - \frac{E_0^2}{2\omega_L^2} \left( \frac{\cos(\omega_L t_s) - \cos(\omega_L t'_s)}{\omega_L t_s - \omega_L t'_s} \right)^2 (t_s - t'_s) \\
 &\quad + \frac{E_0^2}{4\omega_L^2} \left[ (t_s - t'_s) - \frac{\sin 2\omega_L t_s - \sin 2\omega_L t'_s}{2\omega_L} \right] - \omega t_s \\
 &= \left[ \frac{I_p}{\omega_L} - \frac{E_0^2}{2\omega_L^3} \left( \frac{\cos \theta_s - \cos \theta'_s}{\theta_s - \theta'_s} \right)^2 + \frac{E_0^2}{4\omega_L^3} \right] (\theta_s - \theta'_s) \\
 &\quad - \frac{E_0^2}{8\omega_L^3} (\sin 2\theta_s - \sin 2\theta'_s) - \frac{\omega}{\omega_L} \theta_s \\
 &= \frac{2U_p}{\omega_L} \left\{ \left[ \gamma^2 + \frac{1}{2} - \left( \frac{\cos \theta_s - \cos \theta'_s}{\theta_s - \theta'_s} \right)^2 \right] (\theta_s - \theta'_s) \right. \\
 &\quad \left. - \frac{1}{4} (\sin 2\theta_s - \sin 2\theta'_s) - \left( \frac{\tilde{\omega}}{2} + \gamma^2 \right) \theta_s \right\}. \tag{70}
 \end{aligned}$$

Since  $\theta'_s, \theta_s$  are complex,  $\Theta_s$  is also a complex quantity. The real part  $\text{Re}\{\Theta_s\} = \text{Re}\{S_s\} - \omega \text{Re}\{t_s\}$ , in which  $\text{Re}\{S_s\}$  is the phase accumulated during the electron excursion in the continuum. As figure 5(a) shows, larger excursion time leads to larger phase accumulated. From figure 5(b), the imaginary part  $\text{Im}\{\Theta_s\}$  is always negative, which will result in a damping factor  $e^{\text{Im}\{\Theta_s\}}$  in the induced dipole equation (47) and thus a factor  $e^{2\text{Im}\{\Theta_s\}}$  to the HHG yield. This exponential factor is very critical to the HHG yield and it is related to the tunneling ionization rate [80]. We shall discuss this point further in section 3.1. This ionization rate depends sensitively on the strength of the electric field when the electron is born. Since the field strength at born time does not significantly change for L1 and all higher order returns,  $\text{Im}\{\Theta_s\}$  for those orbits are almost on top of each other and independent of  $\tilde{\omega}$ . On the other hand, the S1 orbit is born in a weaker field so that its  $\text{Im}\{\Theta_s\}$  value is well below others'. For S1 orbit, as  $\tilde{\omega}$  grows the field strength at born time will have a considerable increase (see figure 2) and  $\text{Im}\{\Theta_s\}$  will also increase.

To evaluate  $D_{xs}(\omega)$  one needs to know the bound-free transition dipole matrix element  $d_x(p) = \langle p e_x | x | g \rangle$ . In our quantum-orbit analysis the ground state is approximated by a

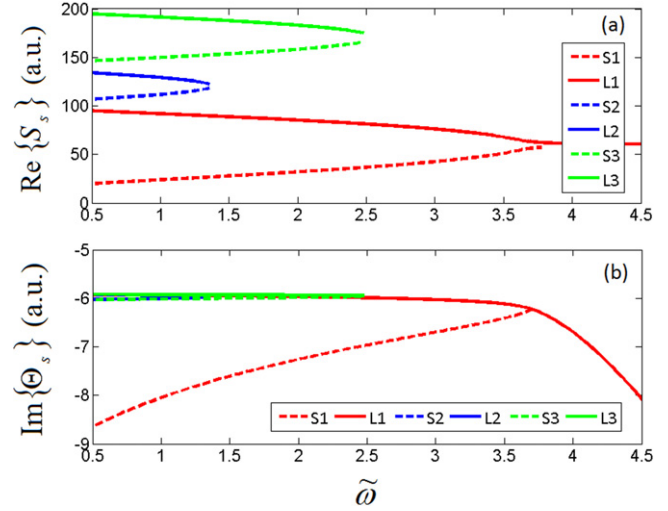


**Figure 5.** (a)  $\text{Re}\{S_s\}$  and (b)  $\text{Im}\{\Theta_s\}$  for quantum orbits up to the third return as functions of  $\tilde{\omega}$  calculated from equation (70). The parameters are the same as in figure 2.

Gaussian form [20]

$$\langle \mathbf{r} | g \rangle = \left( \frac{a}{\pi} \right)^{3/4} e^{-ar^2/2}. \tag{71}$$

So  $d_x(p)$  has a simple analytical expression

$$d_x(p) = i \left( \frac{1}{\pi a} \right)^{3/4} \frac{p}{a} e^{-p^2/2a}, \tag{72}$$

with  $a = 0.8I_p$ . This Gaussian form is convenient since the transition dipole does not have any singularity in the complex plane which could lead to unnecessary complications discussed earlier in section 2.2.1. We will show in section 2.3.2 that the form of transition dipole does not affect the shape of the wave packet as a function of energy.

Figure 6(a) plots the contribution  $|D_{xs}(\omega)|^2$  from each quantum-orbit driven by an 800 nm laser. There are two main factors that determine the HHG yield: the ionization rate given by  $e^{2\text{Im}\{\Theta_s\}}$  and the quantum diffusion described by  $|t_s - t'_s|^{-3}$ . The S1 orbit has the least excursion time and thus the least quantum diffusion, however its ionization rate is considerably smaller. Quantum orbits method shows the latter will dominate so that S1 is weaker than L1. In the lower plateau region S1 may be comparable or even weaker than some of the higher order returns. For the orbits other than S1, since their ionization rates are comparable the dominant factor will be diffusion. Therefore HHG yield drops as the excursion time grows. For example, in the energy range that all returns up to the third contribute,  $L1 > S2 > L2 > S3 > L3$ , as expected. At the cutoff of each return the short and long orbits merge together and the saddle-point approximation produces a spike. Beyond the cutoff the contribution from the short orbit diverges so it must be discarded. Such unphysical divergence can be removed by including the third order derivative term in the Taylor expansion of  $S$  [81] and applying the uniform approximation [43]. We remark that the SFA based quantum orbits method tend to underestimate the contribution from S1 as compared to the TDSE simulation [82, 83]. Figure 6(b)

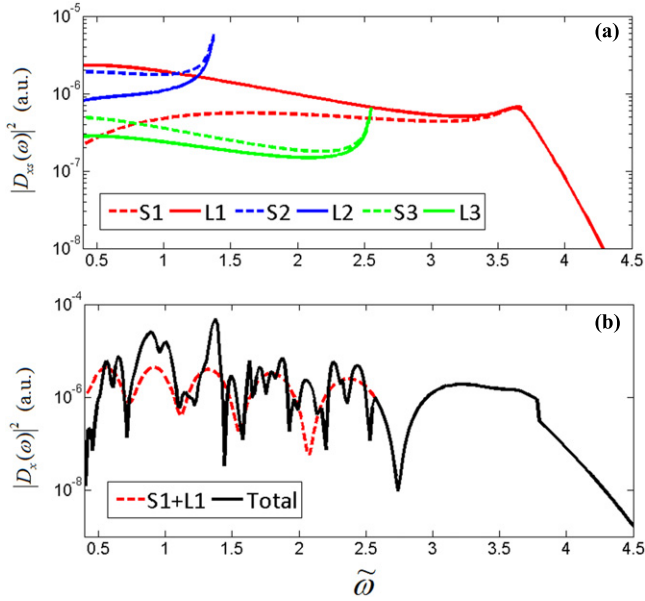


**Figure 6.** (a) HHG spectrum from each individual quantum-orbit. (b) HHG spectrum as a coherent summation of S1 and L1 (dashed red or light grey) and summation of all orbits up to the fifth return (solid black). The parameters are the same as in figure 2.

shows the HHG spectrum as the coherent superposition of various quantum orbits. S1+L1 has a relatively simple oscillating profile since only two orbits are involved. After including higher order returns the spectrum has a more complicated structure, which indicates considerable contribution from higher order returns to the lower plateau. Therefore at single atom level the effect from higher order returns cannot be neglected. However as we consider the macroscopic propagation effect this situation may be changed due to the phase matching of each orbit, see section 4.4.

**2.2.5. The quantum orbits for short laser pulses.** The quantum orbits analysis can also be applied to the situation when the driving laser is a short pulse, for instance, a pulse with a cosine-squared envelope

$$E(t) = E_0 \cos^2\left(\frac{\pi t}{\tau}\right) \cos(\omega_L t + \psi) \quad (73)$$

$$-\frac{\tau}{2} \leq t \leq \frac{\tau}{2}.$$

Here  $\tau$  is the total duration of this pulse, or equivalently, a full width at half maximum (FWHM) duration is approximately  $\tau/2.75$ ,  $\psi$  is the carrier-envelope-phase (CEP), and  $E_0$  is the peak electric field strength.

In the short pulse case (also called non-adiabatic case), due to the breakdown of periodicity we have to treat each half optical cycle individually. Specifically, we need to solve the saddle point equations (43) and (44) to get all quantum orbits for the whole pulse. Figure 7 shows the time profile of a short pulse and the corresponding HHG emission time of the first return as function of photon energy. Clearly, photons emitted in different half cycles have different cutoff energies. The total HHG spectrum is dominated by the emission from a few

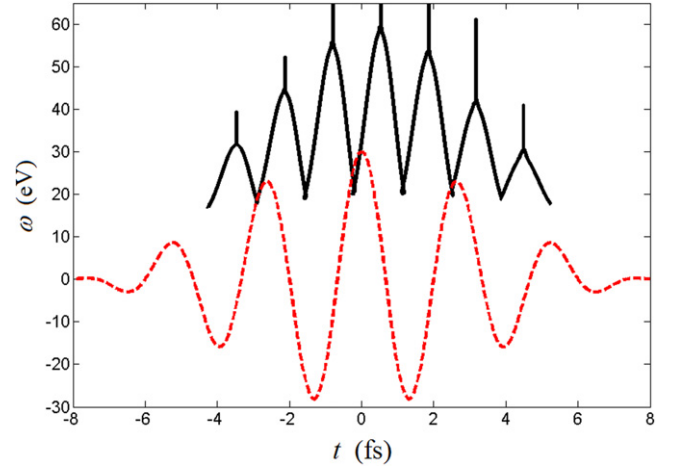


**Figure 7.** Dashed red (or light grey): profile of the electric field of a short laser pulse. Solid black: HHG emission time  $\text{Re}\{t_s\}$  as a function of photon energy (first return only), obtained from equations (43) and (44) for argon ( $I_p = 15.76$  eV). Laser parameters: wavelength 800 nm, peak intensity  $2.0 \times 10^{14}$  W cm $^{-2}$ , FWHM 6 fs,  $\psi = 0$ .

half cycles near the center of the laser pulse, where the photon has the largest cutoff and ionization is also strongest [44]. This is different from the monochromatic light case in which there are numerous half cycles that contribute to the harmonic spectrum equally. The HHG spectrum from a short laser pulse shows a complicated structure as in figure 8 other than sharp odd harmonics. Generally, a few-cycle laser pulse will yield a relatively broad and continuous HHG spectrum in the higher plateau. figure 8 also shows that the quantum orbits method is in qualitative agreement with the direct SFA integral given by equation (36). The cutoff position and the main features of the HHG spectrum are successfully reproduced by QO.

### 2.3. Quantitative rescattering theory

**2.3.1. Formulation and basic concepts.** Here we only briefly describe the QRS formulation to help the reader understand its relationship with other methods discussed in the previous subsections. Interested reader is referred to [12, 46].

The QRS can be considered as a semi-empirical method, relying on an approximate factorization of the HHG induced dipole. The method was originally proposed based on numerical solution of the TDSE for atoms [45, 47] and molecular ion  $\text{H}_2^+$  [48]. It can also be thought of as an ‘extrapolation’ of the factorization equation (54) of the QO theory (see section 2.2.2). The QRS has been ‘justified’ within different approaches, such as the time-dependent effective range theory by Starace, Frolov and collaborators [60–63], the adiabatic theory by Tolstikhin *et al* [64, 84].

For simplicity we discuss below the QRS for linear molecules. Case of polyatomic molecules can be found in [53]. In essence, within the QRS, the (complex) induced dipole  $D(\omega, \theta)$  for a molecule aligned with an angle  $\theta$  with respect to the laser polarization can be written as

$$D(\omega, \theta) = W(E, \theta) d(\omega, \theta), \quad (74)$$

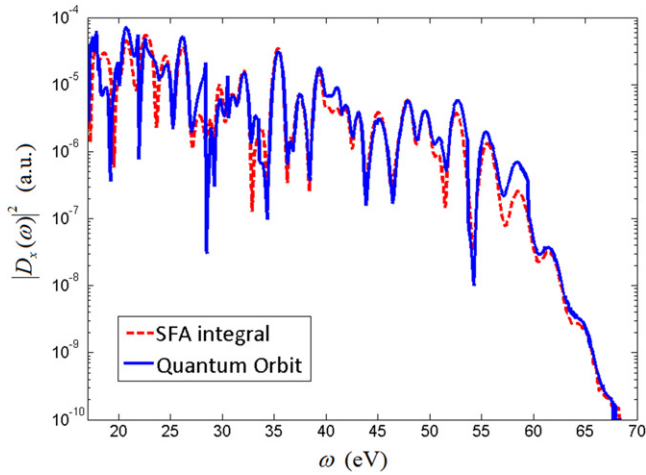


**Figure 8.** HHG spectrum with the short pulse as given in figure 7, obtained from numerical SFA integral equation (36) (dashed line) and from the quantum orbits method (solid line).

where  $d(\omega, \theta)$  is the ‘exact’ transition dipole and the wave packet  $|W(E, \theta)|^2$  describes the flux of the returning electrons. The electron energy  $E$  is related to the emitted photon energy  $\omega$  by  $E = \omega - I_p$ , with  $I_p$  being the ionization potential of the target. Transition dipole  $d(\omega, \theta)$  is the property of the target only, independent of laser parameters. The real power of the QRS comes from the fact that the wave packet, as a function of energy, is nearly independent of the targets (i.e., except for an overall factor, accounting for the different ionization rates). Furthermore, despite that the theory was ‘derived’ using the single active electron model, the transition dipole can be taken from theoretical calculations that account for many-electron correlations. The QRS therefore offers a simple conceptual approach, which relates the nonlinear strong-field physics with the traditional half-collision physics (photo-recombination and its time-reversed, photoionization).

The linear photo-recombination (or its time-reversed, photoionization) transition dipole has been extensively studied since the 1970’s and therefore will not be discussed in this Tutorial. Thus we first focus on the electron wave packet. It turns out that although HHG spectra calculated from SFA or from the QO are not quite accurate, the wave packets [see equation (54)] are quite accurate, as compared to numerical results obtained from solving the TDSE. Recall the three-step model for the HHG process: ionization, propagation, and recombination. In the propagation step, the electron stays mostly outside the target core, and its motion is governed primarily by the laser field. In the strong field approximation, this interaction is treated ‘exactly’. What is missing is the weak electron-ion core interaction. On the other hand, the SFA theory does not treat the ionization rate correctly but this only amounts to an error of the normalization of the wave packet. In the recombination step, the SFA approximates the continuum electron by a plane wave in the calculation of the transition dipole. This is a severe error since recombination occurs near the ion core, and plane wave approximation is well known to be inaccurate for calculating

photo-recombination transition dipole. Thus in the QRS theory, the wave packet can be conveniently obtained by

$$W(E, \theta) \approx W^{SFA}(E, \theta) = \frac{D^{SFA}(\omega, \theta)}{d^{PWA}(\omega, \theta)}, \quad (75)$$

where  $D^{SFA}(\omega, \theta)$  is the induced dipole obtained from the SFA by numerical integration of equation (36) and  $d^{PWA}$  is the transition dipole in the plane-wave approximation. We comment that for most practical applications, the induced dipole is not calculated using the QO theory since accurate calculations of saddle points for short pulses is technically more complicated than numerical integration of equation (36).

The wave packet can also be calculated by using a reference atom with a similar ionization potential, assuming that the transition dipole  $d^{ref}(\omega)$  of the reference atom is known.

$$W^{ref}(E) = \frac{D^{ref}(\omega)}{d^{ref}(\omega)}. \quad (76)$$

This can be done at either TDSE or SFA level, with the use of the exact transition dipole or its plane wave approximation, respectively. The wave packet for the target under consideration is obtained by

$$W(E, \theta) \approx \left( \frac{N(\theta)}{N^{ref}} \right)^{1/2} W^{ref}(E) e^{i\Delta\eta}. \quad (77)$$

Here  $N(\theta)$  and  $N^{ref}$  are the ionization probability for electron emission along the laser polarization direction from the molecule and reference atom, respectively.  $\Delta\eta$  is introduced to account for the phase difference between the two wave packets. This phase difference has been shown to be nearly independent of electron energy [46, 47, 53].

Now let us compare the QRS to other theories. Historically, factorization is implied in Corkum’s three-step model (TSM) [17]. Here the factorization into three factors (tunneling ionization, propagation of the continuum electron in the laser field, and recombination with the parent ion) is in the time domain, not in the energy domain as in the QRS. This model has been considered mostly as a qualitative model. The quantum version of the TSM, the SFA, does not have the factorization explicitly, although factorization in the energy domain has been justified numerically [59]. In section 2.2.2 for the first time we show that factorization can be derived analytically within the QO theory. Interestingly, a factorization similar to the QRS, but in an intensity form (i.e., without the phase), was proposed in Itatani *et al* [6]. In all the above theories, transition dipole in the plane-wave approximation has been used. In the QRS, factorization is assumed to remain valid, but the transition dipole is calculated with accurate scattering continuum wavefunctions. The validity of the QRS has been carefully checked earlier, see, for example, [45–47] and [60–64].

The power of the QRS is not to be overlooked, especially in application to molecular targets. It is extremely computationally efficient since the wave packet can be obtained from the SFA and the transition dipole has to be calculated only once for a required range of photon energy. As the laser’s intensity, wavelength or duration are changed, only the wave

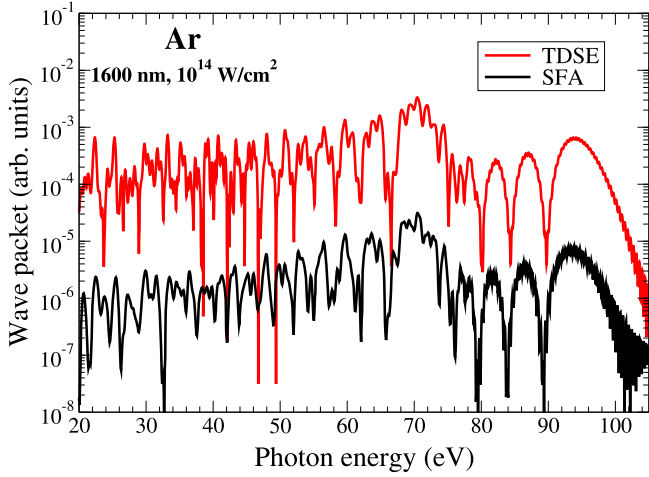


**Figure 9.** Returning electron wave packets extracted from numerical solutions of the TDSE and SFA for Ar. Data have been vertically shifted for clarity. Cosine-squared envelope laser pulse with 4-cycle total duration, 1600 nm wavelength,  $1.0 \times 10^{14} \text{ W cm}^{-2}$  peak intensity is used.

packet has to be recalculated using the SFA. The QRS also stresses that the transition dipoles are under field-free condition, exactly the same as those in conventional photoionization, even though recombination occurs in the laser field. To our knowledge, the QRS is the only method in which the target structure information enters HHG induced dipole (or HHG spectra) in an explicit and simple form. At the macroscopic level, the induced single-atom dipole provided by the QRS allows efficient propagation of harmonic fields in the medium, to generate theoretical high-harmonic spectra that can be directly compared to experiments [55–58].

**2.3.2. Returning electron wave packet and the choice of different dipole forms in the SFA.** In this subsection we show the wave packet from the SFA, its dependence on the target, and on different choices of the dipole form. The good agreement between wave packets from different targets and dipole forms also provides a clear evidence for the validity of the factorization within the QO discussed in section 2.2.2.

Figure 9 shows the comparison of the electron wave packets extracted from the TDSE and SFA for Ar. We use a 1600 nm wavelength laser pulse with 4-cycle total duration (with a cosine-squared envelope) and peak intensity of  $1.0 \times 10^{14} \text{ W cm}^{-2}$ . Overall, the wave packet extracted from the SFA (shifted vertically for clarity) is in good agreement with the TDSE result. Other examples can be found in [46, 47]. Since HHG spectra from the QO agree well with the numerical SFA (see figure 8), it is clear that a similar level of agreement is expected for the QO wave packet as well.

Having established the adequacy of the SFA wave packet, we next discuss the wave packet using a reference atom within the SFA. Although this case has been illustrated earlier in [45–47], here we give a toy model for a mid-IR case. For our purpose we use a scaled hydrogen atom with  $I_p = 15.76 \text{ eV}$  and the transition dipole in the plane wave

approximation written as [20]

$$d(\mathbf{p}) = -i \frac{2^{7/2} \alpha^{5/4}}{\pi} \frac{\mathbf{p}}{p^2 + \alpha}, \quad (78)$$

with  $\alpha = 2I_p$ . Here the nuclear charge is scaled so that the 1 s ground state has the ionization potential of argon. For comparison we use a fictitious atom with the same  $I_p$ , but with a different transition dipole

$$d(\mathbf{p}) = -i \frac{2^{7/2} \alpha^{5/4}}{\pi} \left[ \frac{\mathbf{p}}{(p^2 + \alpha)^3} - \frac{\mathbf{p}}{(ap^2 + b\alpha)^3} \right], \quad (79)$$

with  $a = 0.0368$  and  $b = 3.13$ . This choice of the transition dipole gives an artificial ‘Cooper minimum’ in photoionization cross section near 51 eV. We show in figure 10(a) and 10(b) HHG spectra from these two atoms and their electron wave packets, respectively. Both results were obtained from the SFA with 1600 nm wavelength laser pulse of 6-cycle total duration (with a cosine-squared envelope) and intensity of  $10^{14} \text{ W cm}^{-2}$ . The HHG spectra from the two targets are quite different, with a clear minimum near 51 eV in the fictitious atom case, which is the consequence of the presence of the Cooper minimum in the photoionization cross section. Nevertheless, the wave packets from the two targets are nearly identical, except at the vicinity of the Cooper minimum. The insensitivity of the wave packet (apart from an overall factor) is the main reason that a reference atom can be used. In fact, wave packet from a reference scaled hydrogen atom has an advantage that it avoids the ‘spurious’ peaks often seen in the wave packet obtained from the SFA. Such a spurious peak seen in figure 10(b) is the result of division by zero in equation (75) at the Cooper minimum near 51 eV. No such a Cooper minimum exists in hydrogen. Note that there is a small technical issue for hydrogen if the QO theory is used instead of numerical integration of the SFA. Indeed, within the QO theory, there is a singularity in transition dipole at  $p^2/2 = -I_p$  for hydrogen, see equations (43), (47), and (78). Due to this singularity, the QO equation (47) should be modified for hydrogen [85]. For this reason, it is more convenient to use a Gaussian form for transition dipole as in equation (72) [20, 86]. Based on the above results, it becomes clear that this choice of dipole form only affects HHG spectrum, but it does not change the shape of the electron wave packet.

Let us now consider different choices of dipole form. It is well known from photoionization theory that there are different forms for the transition dipole operator. To be specific let us consider hydrogen atom. The matrix elements of  $\mathbf{r}$ ,  $\mathbf{p}$ , and  $\partial V(r)/\partial \mathbf{r} = -\mathbf{r}/r^3$  are called length, velocity, and acceleration dipole form, respectively [87]. These forms are related by the following equations

$$\langle \Psi_0 | \mathbf{p} | \Psi_f \rangle = -i \omega \langle \Psi_0 | \mathbf{r} | \Psi_f \rangle, \quad (80)$$

$$\langle \Psi_0 | \frac{\mathbf{r}}{r^3} | \Psi_f \rangle = \omega^2 \langle \Psi_0 | \mathbf{r} | \Psi_f \rangle. \quad (81)$$

Although these forms are equivalent, they give somewhat different results for photoionization cross sections in approximate theories. So far we have only considered the

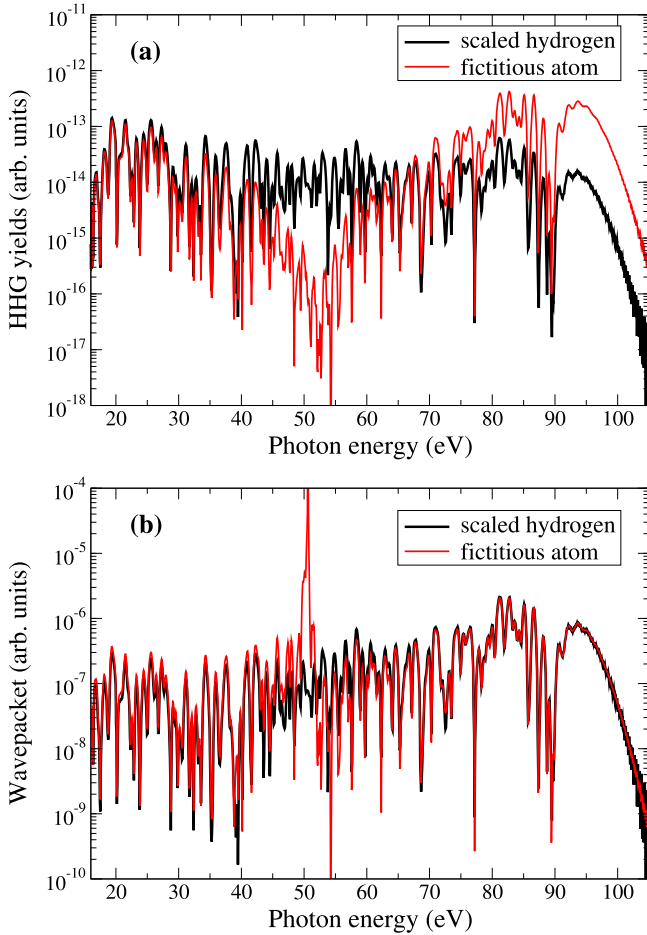


**Figure 10.** (a) HHG yields from scaled hydrogen and a ‘fictitious’ atom. (b) Same as (a), but for electron wave packets. Cosine-squared envelope laser pulse with 6-cycle total duration, 1600 nm wavelength,  $1.0 \times 10^{14} \text{ W cm}^{-2}$  peak intensity is used.

length form for the induced dipole, as it was originally introduced in the SFA by Lewenstein *et al* [20]. Clearly, velocity and acceleration forms of the SFA can also be formulated. More specifically, instead of using equations (8) and (9) for the induced dipole and HHG power in the length form, we can use

$$\mathbf{v}(t) = \langle \Psi(t) | \mathbf{p} | \Psi(t) \rangle, \quad (82)$$

and

$$P(\omega) \propto \omega^2 |v_x(\omega)|^2, \quad (83)$$

for the velocity form (assuming that the laser is linearly polarized along  $x$ -axis), and

$$\mathbf{a}(t) = \langle \Psi(t) | \frac{\partial V}{\partial \mathbf{r}} | \Psi(t) \rangle, \quad (84)$$

and

$$P(\omega) \propto |a_x(\omega)|^2, \quad (85)$$

for the acceleration form. Here dipole velocity  $v(\omega)$  (or acceleration  $a(\omega)$ ) is the Fourier transform of  $v(t)$  [or  $a(t)$ ] and the wavefunction  $\Psi(t)$  is given by equation (7). The formal derivation of the SFA in these forms proceeds in a similar fashion as in section 2.1.1. Similar to photoionization,

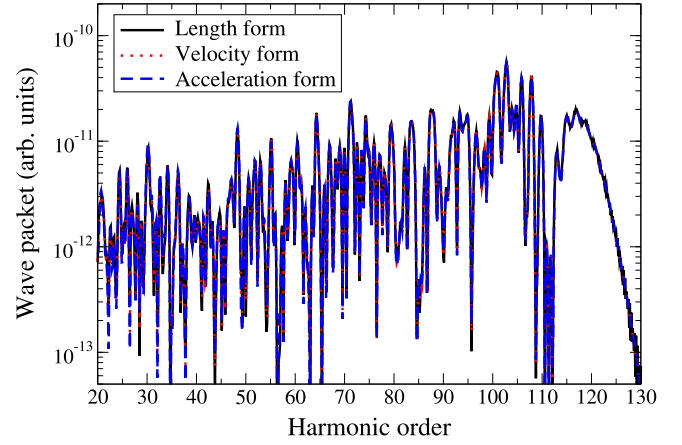


**Figure 11.** Returning electron wave packets extracted from length, velocity, and acceleration forms of the SFA for hydrogen. Cosine-squared envelope laser pulse with 6-cycle total duration, 1600 nm wavelength,  $1.0 \times 10^{14} \text{ W cm}^{-2}$  peak intensity is used.

these forms lead to different HHG spectra in the SFA. There have been some debates about the preference of the velocity or acceleration forms over the length form (see, for example, [88–90]). Here we show that the electron wave packet is quite insensitive to a specific choice of the dipole form, as long as the same form is used in both photoionization and HHG dipoles. In other words, we found that

$$W^{SFA}(E) = \frac{D_x^{SFA}(\omega)}{\langle \Psi_0 | x | \mathbf{p} \rangle} \approx \frac{v_x^{SFA}(\omega)}{\langle \Psi_0 | p_x | \mathbf{p} \rangle} \approx \frac{a_x^{SFA}(\omega)}{\langle \Psi_0 | \partial V / \partial x | \mathbf{p} \rangle}. \quad (86)$$

Here a plane wave  $\mathbf{p}$  has been used for the final wavefunction  $\Psi_f$ . The good agreement among the different dipole forms for the wave packet is illustrated in figure 11. In fact, the results are indistinguishable in the figure. This result is not unexpected. In fact, the insensitivity of the wave packet with respect to different dipole forms is just a special case of the independence of the wave packet on the target, discussed in the beginning of this subsection. It is a manifestation of the approximate factorization of the induced dipole, as shown in section 2.2.2. Finally we remark that although the discussion above only concerns the magnitude of the wave packet, its phase can also be analyzed. Interested reader is referred to [46, 47].

#### 2.4. Other modifications to the SFA

The standard SFA is well founded only for short range potential targets such as negative charged ions. For long range Coulomb potential some additional corrections taking into account the so-called Coulomb-laser coupling can be implemented to make the SFA model more accurate [91, 92]. For example, the phase and amplitude of the Volkov wave function that describes the continuum electron can be corrected by using the eikonal approximation [93].

One of the approaches to improve the SFA for HHG was suggested by Ivanov *et al* [41]. In their approach, the induced dipole in time domain is expressed as a sum over ionization

(born) times, which are the solution of the stationary phase of the action. This is in contrast to the QO theory, where the dipole is given in energy domain and both ionization and recombination times satisfy stationary coupled equations. Therefore in their approach the recombination time remains real. At each born time, the dipole in their approach can be written as a product of three factors: ionization, propagation, and recombination. The procedure is then to make modification to each factor to account for the Coulomb interaction between electron and the core. The Coulomb correction for ionization can be done as in the Perelomov–Popov–Terent’ev (PPT) theory [94] (see section 2.5). Note that in their original paper, an ‘effective’ ionization potential of the form  $I_p + v_y^2/2$  was used in order to account for electron’s initial momentum along the minor axis at the born time in the case of elliptically polarized laser. For the propagation, they modified the action to include the Coulomb term within a certain approximation. The recombination amplitude can also be modified. We remark that their approach is quite close to the QRS. However, since it is done in the time domain, the three steps become entangled upon Fourier transform to the energy domain, thus destroying the direct relationship between photo-recombination dipole and HHG dipole. Furthermore, one still has to sum over many stationary solutions so the factorization for the total yield is not guaranteed. Nevertheless, there are some advantages in this approach, including an intuitive description of sub-cycle dynamics. In fact, this approach has been extended to include sub-cycle multi-electron dynamics in HHG from aligned CO<sub>2</sub> [9].

Other attempts to improve the SFA include using different forms of dipole such as dipole acceleration and dipole velocity [88, 89, 95]. We also mention here other modifications of the SFA by including the effect of field dressing on the bound state [96–98]. An attempt to account for the Coulomb interaction by using approximate two-center Coulomb wavefunction in the recombination step was also reported for molecular ion H<sub>2</sub><sup>+</sup> [99]. Quite recently, Madsen and collaborators [100, 101] have also accounted for the initial state distortion due to the instantaneous field the framework of the SFA. All these attempts have been partially successful in improving certain feature of HHG spectra. However, they do not, to the best of our knowledge, provide evidence for the link between HHG dipole and target structure information embedded in the recombination dipole.

## 2.5. Strong-field ionization: SFA versus other methods

Ionization is the first and utmost nonlinear step in a HHG process. According to the factorization in the QRS and the QO, ionization gives the overall magnitude of the returning electron wave packet. Since experiments do not typically measure absolute HHG yields, one might think that knowledge of ionization from atomic targets is not critical in the application of the QRS or other modifications of the three-step model. That argument is only partially valid for the single-atom response, when the depletion of the ground state is insignificant. In practice, in order to compare with

experimental measurements, simulation of macroscopic phase-matching propagation needs to be carried out (see section 4). This accounts for, in particular, the laser intensity variation within the interaction region. Therefore, the relative ionization rates at different intensities are needed. Similarly, knowledge of relative ionization rates for different molecular alignments and/or orientation is required to simulate the HHG from molecules. Clearly, absolute rates are needed to calculate absolute HHG yields.

In this subsection we discuss three different theoretical methods, namely, the SFA, PPT and ADK. In order to judge about the quality of each method, we compare them with the TDSE calculations in two illustrative examples.

**2.5.1. Theoretical description of the SFA.** In general, the SFA is quite adequate for describing the dependence of ionization on laser intensity, especially at long wavelengths, but the absolute yield needs to be renormalized. Here we only work within the length gauge. The reason is twofold. First, it has been shown that for negative ions with a short range potential, where the SFA is expected to be most accurate, the length gauge is much more accurate than the velocity gauge for photoelectron energy spectra, up to an overall scaling factor [102]. Second, it was also found [103] that the alignment dependent ionization rate for N<sub>2</sub> from the length gauge SFA agrees well with experiments, whereas the velocity gauge does not. Note that for HHG, we also use the SFA in the length gauge only (see, section 2.1.1).

Within the SFA in the length gauge [22], the ionization amplitude for a transition of an active electron from a bound state  $\Psi_0(\mathbf{r})$  to a continuum state with momentum  $\mathbf{p}$  is given by

$$f(\mathbf{p}) = i \int_{-\infty}^{\infty} dt \langle \mathbf{p} + \mathbf{A}(t) | \mathbf{r} \cdot \mathbf{E}(t) | \Psi_0 \rangle \times \exp[-iS(\mathbf{p}, t)], \quad (87)$$

where

$$S(\mathbf{p}, t) = \int_t^{\infty} dt' \left\{ \frac{[\mathbf{p} + \mathbf{A}(t')]^2}{2} + I_p \right\}. \quad (88)$$

These equations are quite similar to equations (13) and (26), respectively, but with the evolution operator being replaced by that of a free electron in the laser field  $U_F(t, \infty)$ . The electron is born into the continuum at time  $t$  and propagates further in the laser field until the final time at a detector. Again, the effect of the core potential is neglected, as usual in the SFA, for the continuum state, which is approximated by a Volkov state

$$\langle \mathbf{r} | \mathbf{p} + \mathbf{A}(t) \rangle = \frac{1}{(2\pi)^{3/2}} \exp \{ i[\mathbf{p} + \mathbf{A}(t)] \cdot \mathbf{r} \}. \quad (89)$$

The ionization probability is given by the integrated signal over all emission directions

$$P = \int d\phi_e \int d\theta_e \sin \theta_e \int dp^2 |f(\mathbf{p})|^2, \quad (90)$$

where  $\phi_e$  and  $\theta_e$  are the azimuthal angle and polar angle of the electron momentum  $\mathbf{p}$ . The integrations in equations (87) and

(90) are carried out numerically. In case of a monochromatic laser, further analytical calculation can be carried out to express the probability and rate as sum of  $n$ -photon absorption via generalized Bessel functions [91, 103].

We note that the Coulomb potential is neglected in the SFA, while it is accounted for in the PPT [94, 104, 105] and the ADK [78] theories. In fact, one can introduce a Coulomb correction factor,  $C_c^2 = (\kappa^3/E_0)^{2Z_c/\kappa}$ , to the SFA rates [106]. Here,  $Z_c$  is the charge of the residual ion,  $\kappa = \sqrt{2I_p}$ , and  $E_0$  is the electric field strength of the laser. This version of the SFA will be called the SFA-CC in the following.

The SFA can be extended to include higher order interaction with the ion core. This has been done in the so-called SFA2 [74] or improved SFA [26]. However this higher-order effect does not change the total ionization probability significantly and therefore is not included in typical simulations.

Extension of the above equations for a molecule is straightforward. Clearly, the ionization probability  $P$  in equation (90) will depend on the direction of the laser polarization with respect to the molecule. For molecules, it is convenient to use quantum chemistry packages such as Gaussian [107] or Gamess [108] to calculate molecular orbitals. Within the single active electron approximation, the bound state wavefunction for the active electron  $\Psi_0(\mathbf{r})$  is typically taken as the highest occupied molecular orbital (HOMO) at the Hartree–Fock or DFT levels. The use of Gaussian-type orbitals allows analytical calculations of the matrix elements entering equation (87), making its numerical integration very efficient.

**2.5.2. PPT, ADK and their extension to molecules.** The ADK theory [78] for atoms has been extended to molecular targets by Tong *et al* [109] (so-called the MO-ADK theory) based on a single-center expansion for the asymptotic molecular wavefunction. A similar approach can be used to extend the PPT theory [94, 104] to molecular target [110, 111]. The resulting theory, called the molecular PPT (MO-PPT or simply PPT), is expected to have a broader range of validity as compared to the MO-ADK theory. Recall that the ADK is strictly a tunneling theory, which can also be obtained from the PPT in the limit of small Keldysh parameter  $\gamma \rightarrow 0$ .

There have been some confusions in the literature due to misprints as well as different notations used in the ADK and PPT theory, we therefore briefly describe the main results here. For clarity we consider linear molecules. Nonlinear polyatomic case can be done in a similar manner [112]. The wavefunction of the active electron can be expressed in a single-center expansion as  $\sum_l F_l(r) Y_{lm}(\mathbf{r})$ , with the asymptotic radial functions  $F_l(r \rightarrow \infty) \approx C_l r^{Z_c/\kappa-1} \exp(-\kappa r)$ . Here  $m$  is the magnetic quantum number along the molecular axis and  $\kappa = \sqrt{2I_p}$ . If the molecular axis is along the laser polarization direction, following the derivation of [94, 104, 109] the cycle-averaged rate from the PPT can be

written as

$$W(0) = \left( \frac{3E_0}{\pi\kappa^3} \right)^{1/2} \frac{B^2(m)}{2^{|m|}|m|!} \frac{A_m(\omega, \gamma)}{\kappa^{2Z_c/\kappa-1}} \left( \frac{2\kappa^3}{E_0} \right)^{2Z_c/\kappa-|m|-1} \times (1 + \gamma^2)^{|m|/2+3/4} \exp\left( -\frac{2\kappa^3}{3E_0} g(\gamma) \right), \quad (91)$$

where functions  $A_m(\omega, \gamma)$  and  $g(\gamma)$  can be found in [104, 113], and  $B(m) = \sum_l C_l Q(l, m)$ , with  $Q(l, m) = (-1)^{(m+|m|)/2} \sqrt{\frac{(2l+1)(l+|m|)!}{2^{l-|m|} l!}}$ . The factor  $\left( \frac{3E_0}{\pi\kappa^3} \right)^{1/2}$  is due to averaging over an optical cycle [104]. In the limit of  $\gamma \rightarrow 0$ , both  $A_m$  and  $g(\gamma)$  go to 1 and equation (91) coincides with the MO-ADK theory [109]. For atoms it coincides with equation (10) of [114] and with equation (54) of [104] with the Coulomb correction factor  $(2\kappa^3/E_0)^{2Z_c/\kappa}$  included [94]. Note also that Popruzhenko *et al* [115] recently proposed an ‘improved’ correction that includes the next order term in  $\gamma$ . We further remark that the structure coefficients are defined slightly differently in Tong *et al* [109] and the original ADK paper [78]. In essence, they are related by  $|C_l|^2 = |C_{n^*l^*}|^2 \kappa^{2Z_c/\kappa+1}$ , although the practical procedures to obtain their values and the recommended values differ in these two papers. In PPT theory, the structure coefficient was defined in the same way as in the ADK, see equation (6) of [104]. In this paper we follow the notation of Tong *et al* [109]. We remark in passing that in [109], the direction of ionized electron was assumed to be along  $z \rightarrow +\infty$ . This means that the electric field is directed along  $z \rightarrow -\infty$ . In other words, strictly their equation (7) should correspond to  $\theta = \pi$ .

For a molecule aligned along an arbitrary axis with respect to the field direction  $B(m)$  in equation (91) has to be replaced by

$$B(m') = \sum_l C_l D_{m'm}^l(\Omega) Q(l, m'), \quad (92)$$

with  $D_{m'm}^l$  being the rotation matrix and  $\Omega$  the Euler angles. In Tong *et al* [109], the rate is expressed as a sum over all  $m'$  terms as

$$W = \sum_m W_{m'}, \quad (93)$$

where  $W_{m'}$  is given in equation (91) with  $B(m)$  replaced by  $B(m')$ . Following Tolstikhin *et al* [116], for consistency reason, one should only retain the dominant term with  $m' = 0$ . Clearly, this would affect mostly near nodal lines, where the  $m' = 0$  term vanishes. We found that this modification of the original MO-ADK gives an alignment dependence in better agreement with the SFA results.

**2.5.3. Illustrative examples and general remarks.** We now compare the SFA with different methods to obtain ionization probability for hydrogen atom in few-cycle laser pulses. Comparison for the TDSE, ADK, PPT, and SFA for the wavelength of 400 nm, 800 nm, and 1600 nm is shown in figure 12 for a range of intensity from  $1 \times 10^{13}$  to  $1.5 \times 10^{14}$  W cm<sup>-2</sup>. The laser pulse duration (full duration with the sine-square envelope) is 12-cycle for 400 nm, and 6-cycle for the

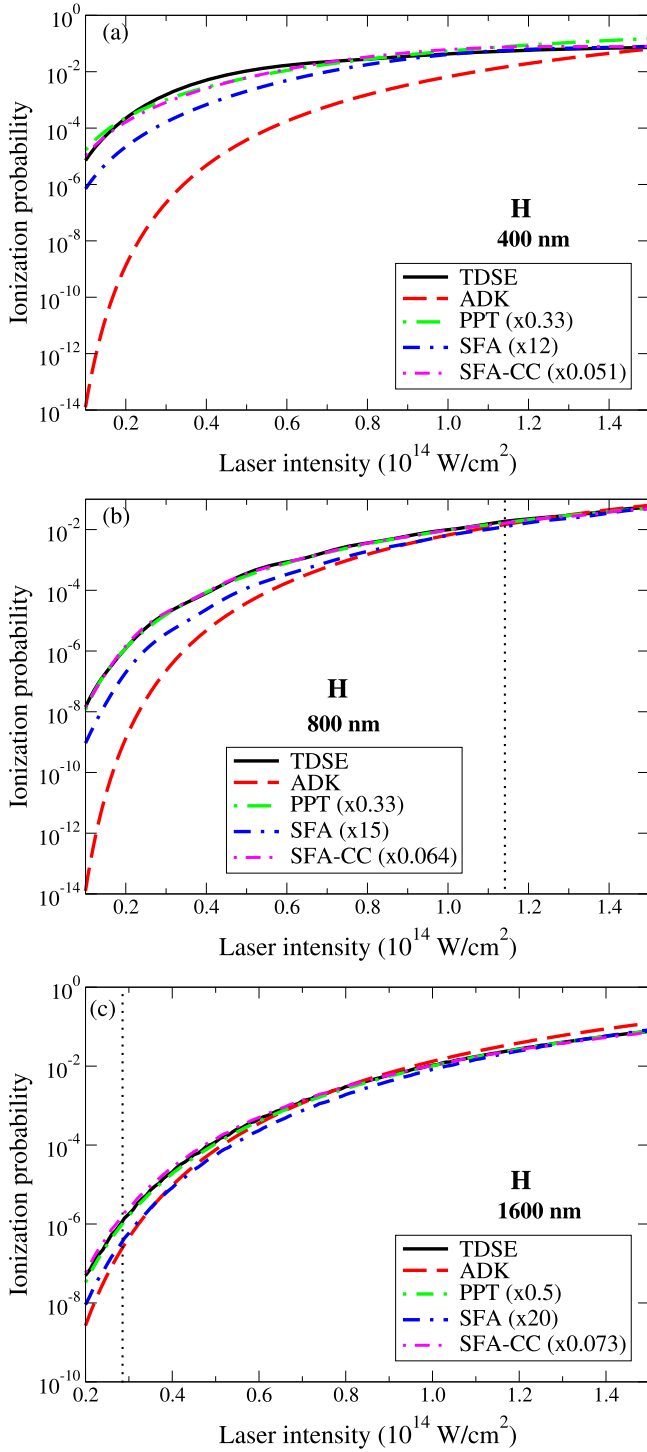


**Figure 12.** Comparison of different methods for ionization probability for hydrogen atom vs laser intensity for the wavelength of 400 nm (a), 800 nm (b), and 1600 nm (c). Note that for each wavelength the PPT and SFA results have been multiplied by a factor given in the labels. The vertical dotted lines indicate the position with  $\gamma = 1$ .

other cases. These parameters were chosen so that the Keldysh parameter  $\gamma \simeq 1$  is well within the intensity range for 800 nm and the ionization probability is still far from saturation. At 800 nm, shown in figure 12(b) the SFA result (rescaled by a factor of 15) agrees fairly well with the TDSE

over the large range of laser intensity. The SFA-CC (rescaled by 0.064) agrees much better with the TDSE. The ADK result only agrees at high intensities above about  $1 \times 10^{14}$  W cm $^{-2}$ , which is in the tunneling regime. Note that no scaling factor is used for the ADK in this intensity range. However, below its range of validity, the quality of the ADK result decreases significantly. In fact, at  $4 \times 10^{13}$  W cm $^{-2}$ , the ADK underestimates by almost two orders of magnitude. The PPT result (rescaled by a factor of 1/3) nicely reproduces the TDSE result for the whole range of laser intensity. As the laser wavelength increases to 1600 nm (see figure 12(c)), there is relatively good agreement among all the methods for the whole intensity range. Clearly, all of these approximate methods become better with mid-infrared lasers. While the level of agreement with the TDSE for PPT and SFA is only slightly reduced, as the laser wavelength decreases to 400 nm, as shown in figure 12(a), the quality of ADK theory clearly deteriorates in this multiphoton ionization regime. We remark that in all these cases, the SFA underestimates, whereas the SFA-CC overestimates, and the PPT slightly overestimates the ionization probability for hydrogen. The above results are quite typical. In fact, similar behaviors were also found for other atoms as well as molecules.

As another example we show in figure 13 the comparison for the case of molecular H $_2$ , perfectly aligned along laser polarization direction. The TDSE results were taken from Saenz *et al* [117]. In all cases, the pulse duration (total duration with sine-square envelope) was taken to be about 32 fs. Note that no scaling factor is used in the PPT and MO-ADK results shown in the figure. Here, the MO-ADK is only valid near  $\gamma \approx 1$  (indicated by the dashed line in the figure) for the case of 800 nm. For the other wavelengths, the  $\gamma \approx 1$  range falls into the saturation regime already. Overall, the PPT is superior to the MO-ADK in the whole range of laser intensity, although a small correction factor is still needed. Comparison with different version of the SFA results can be found in [117], which shows that in general an overall scaling factor is needed for the SFA to reproduce the TDSE results for H $_2$ . We remark that comparison with the MO-ADK results for 400 nm and 266 nm is not quite useful here since in the range of its validity the ionization is already well saturated (ionization probability is identical to 1). Clearly, a shorter pulse is more desirable.

The above analysis indicates that the ADK theory is barely adequate for 800 nm wavelength in a small range of laser intensity. The validity range for the ADK significantly increases with longer wavelengths. For the SFA, the overall quality of the SFA is quite good in a relatively broad range of intensity, although one always needs to rescale the ionization rates. That is the main reason that many calculations are still based on the SFA. In particular, the SFA results can be renormalized to the ADK results at the region of the ADK validity. This practice is particularly useful for molecular target (see, for example, [11, 46]). With slightly more computational effort compared to the ADK, one can get the PPT rates which are uniformly adequate for a larger range of laser intensity and wavelength. Unfortunately, a small correction factor is still needed.

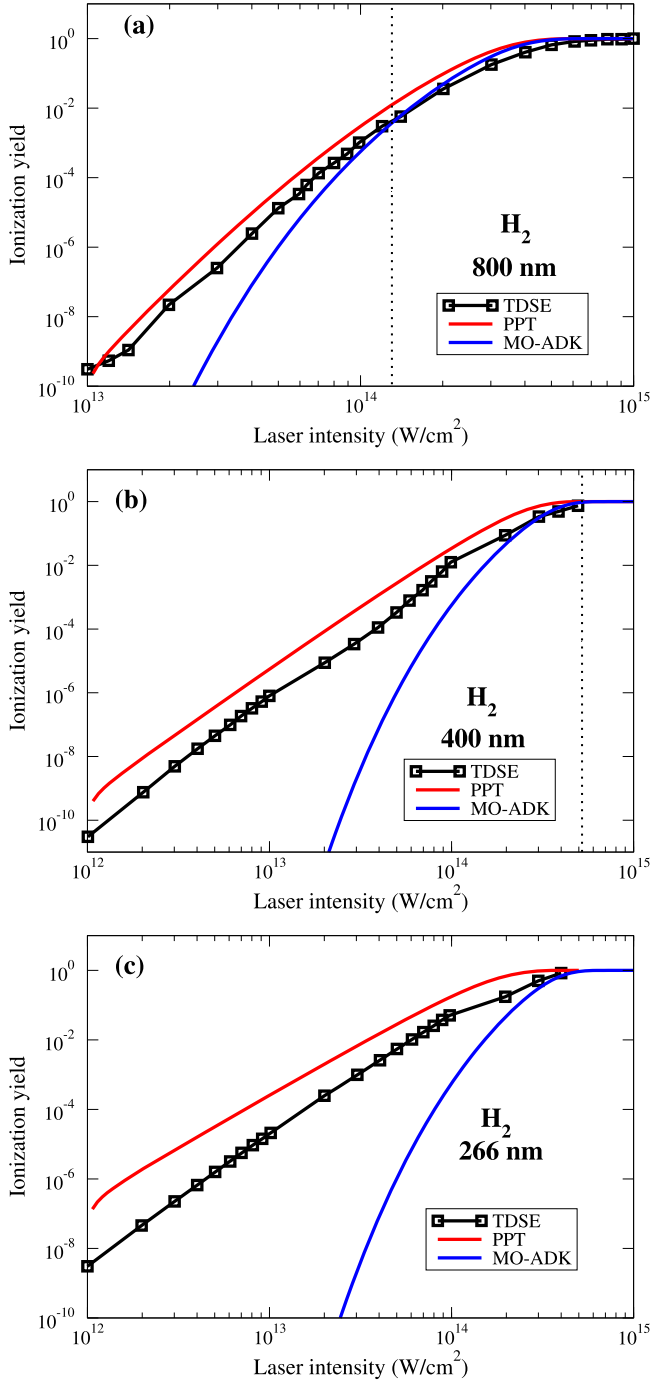


**Figure 13.** Same as figure 12 but for  $\text{H}_2$  at the wavelength of 800 nm (a), 400 nm (b), and 266 nm (c). The TDSE results were taken from Saenz *et al* [117]. The laser polarization is along the molecular axis. The vertical dotted lines indicate the position with  $\gamma = 1$ .

We further note that in applications of both ADK and PPT, one needs to know the structure coefficients  $C_{lm}$ . These structure coefficients are extracted using the wavefunction at asymptotic distance, which still poses difficulties at present. In fact, the structure coefficients differ significantly from different methods and different authors. The main difficulty stems from the fact that standard quantum chemistry packages such as Gaussian [107] or Gamess [108] are based on the

Gaussian-type orbitals expansion, which decays too rapidly at large distance. For linear molecules, in principle one can solve the Hartree–Fock equation with a grid-based numerical method exactly [118]. Alternatively, one can use specially optimized Gaussian basis sets for that purpose [119]. Another approach is to construct a model potential for molecules and solve the Schrödinger equation numerically to extract structure constants [120, 121]. These approaches are dependent on the Hartree–Fock or a specific choice of the density functional, so variations in extracted structure constants are still expected. Nevertheless, extension of these methods to polyatomic molecules are desirable.

Clearly, the accuracy of theoretical ionization rates, which governs the overall magnitude of the returning wave packet, remains critical at present. The recently developed weak-field asymptotic theory (WFAT) [116, 119, 122, 123] appears to be quite promising. Nevertheless, its application to polyatomic molecules remains to be seen. Treatment for polar molecules has been proposed in the so-called Stark-corrected MOADK and SFA [124–126]. A more rigorous treatment was also reported in the WFAT [116, 122].

It is important to also realize that, in contrast to the ADK, which is a truly static theory, the PPT does not give instantaneous rate. For an arbitrary  $\gamma$ , sub-cycle (instantaneous) rate can be obtained by using Yudin–Ivanov model [127], which reduces to the PPT for the cycle-averaged rate. New developments in ionization rates include analytical  $R$ -matrix method by Torlina and Smirnova [128] and its extension to many-electron targets [129].

### 3. HHG with mid-infrared driving laser: universality of the electron wave packet and scaling law

#### 3.1. Quantum orbits analysis of long and short trajectories at long wavelengths

In this section we apply the quantum orbits analysis on HHG driven by mid-infrared lasers. Let’s imagine a situation when the laser wavelength  $\lambda$  is increased gradually while the field strength  $E_0$  is fixed, such that the laser-atom interactions are kept in the tunneling regime. Since the HHG cutoff is determined by  $I_p + 3.2U_p$  and  $U_p \propto \lambda^2$ , by using a mid-infrared laser the HHG spectrum may be extended to hundreds of eVs (covering the water window) or even the keV regime (soft x-ray) [68, 69]. The Keldysh parameter

$$\gamma = \sqrt{\frac{I_p}{2U_p}} = \frac{\sqrt{2I_p}}{E_0} \omega_L \propto \lambda^{-1}, \quad (94)$$

where  $\omega_L = 2\pi c/\lambda$  is the laser frequency. Clearly  $\gamma$  decreases as the wavelength is increased, thus in the long wavelength limit  $\gamma \ll 1$  and ionization falls into the deep tunneling regime. In this limit tunneling (imaginary part of the born time) only occurs within a very tiny time interval compared to the optical period. Our goal here is to seek further simplification in the QO theory in order to investigate the behavior of harmonics due to long and short orbits in this regime.

In the long wavelength limit, the saddle point equations (66) and (67) can be simplified by approximating the recombination time  $\theta$  to be a real quantity [80, 130] while keeping the born time  $\theta'$  complex. Here we separate the real and imaginary part of the ionization time explicitly:  $\theta' = \alpha + i\beta$ ,  $0 < \alpha < \frac{\pi}{2}$  and  $\beta > 0$ . The  $\sin \theta'$  and  $\cos \theta'$  term can be rewritten as

$$\sin \theta' = \sin(\alpha + i\beta) = \sin \alpha \cosh \beta + i \cos \alpha \sinh \beta, \quad (95)$$

$$\cos \theta' = \cos(\alpha + i\beta) = \cos \alpha \cosh \beta - i \sin \alpha \sinh \beta. \quad (96)$$

Since  $\sin \theta$  is real in this approximation, by following the constraint equation (67), we have to approximate  $\frac{\cos \theta - \cos \theta'}{\theta - \theta'}$  to be real consistently, i.e.

$$\begin{aligned} \frac{\cos \theta - \cos \theta'}{\theta - \theta'} &\approx \operatorname{Re} \left\{ \frac{\cos \theta - \cos \theta'}{\theta - \theta'} \right\} \\ &= \operatorname{Re} \left\{ \frac{\cos \theta - \cos \alpha \cosh \beta + i \sin \alpha \sinh \beta}{\theta - \alpha - i\beta} \right\} \\ &= \frac{(\cos \theta - \cos \alpha \cosh \beta)(\theta - \alpha) - \beta \sin \alpha \sinh \beta}{(\theta - \alpha)^2 + \beta^2}. \end{aligned} \quad (97)$$

Then equations (66) and (67) can be reduced to

$$\cos \alpha \sinh \beta = \gamma, \quad (98)$$

$$\begin{aligned} \frac{(\cos \theta - \cos \alpha \cosh \beta)(\theta - \alpha) - \beta \sin \alpha \sinh \beta}{(\theta - \alpha)^2 + \beta^2} \\ + \sin \alpha \cosh \beta = 0, \end{aligned} \quad (99)$$

$$2(\sin \theta - \sin \alpha \cosh \beta)^2 = \tilde{\omega}. \quad (100)$$

When  $\gamma \ll 1$  and the ionization time is ionized not too far from the (sub-cycle) peak of the electric field, for example  $0 < \alpha < \frac{\pi}{3}$ , from equation (98) we get

$$\sinh \beta = \frac{\gamma}{\cos \alpha}, \quad (101)$$

$$\cosh \beta = \sqrt{1 + \left(\frac{\gamma}{\cos \alpha}\right)^2} \approx 1 + \frac{\gamma^2}{2 \cos^2 \alpha}, \quad (102)$$

$$\begin{aligned} \beta &= \ln \left[ \frac{\gamma}{\cos \alpha} + \sqrt{1 + \left(\frac{\gamma}{\cos \alpha}\right)^2} \right] \\ &\approx \frac{\gamma}{\cos \alpha} - \frac{\gamma^3}{6 \cos^3 \alpha}. \end{aligned} \quad (103)$$

Substituting equations (101)–(103) into equations (99) and (100) yields

$$\begin{aligned} (\cos \theta - \cos \alpha) + (\theta - \alpha) \sin \alpha \\ + \frac{\gamma^2}{2 \cos \alpha} \left( \frac{(\theta - \alpha) \sin \alpha}{\cos \alpha} - 1 \right) = 0, \end{aligned} \quad (104)$$

$$2(\sin \theta - \sin \alpha)^2 - \frac{2 \sin \alpha (\sin \theta - \sin \alpha)}{\cos^2 \alpha} \gamma^2 = \tilde{\omega}. \quad (105)$$

In equations (104) and (105) we keep terms up to the order of  $\gamma^2$ . One can solve these equations to obtain the real born time  $\alpha_s$  and return time  $\theta_s$  for a given scaled photon energy  $\tilde{\omega} = (\omega - I_p)/U_p$ . These solutions will depend on the Keldysh parameter  $\gamma$ . Clearly as  $\gamma \rightarrow 0$ , equations (104) and (105) reduce to classical equations (68) and (69), thus  $\alpha_s$  and  $\theta_s$  will converge to their classical counterparts  $\theta'_c$  and  $\theta_c$ , respectively. This convergence is shown in figure 14 for the first return. Higher order returns also have similar convergence. While clear differences can be seen for the  $0.8 \mu\text{m}$  case in figure 14, the QO results become very close to the classical values quickly for  $\lambda \gtrsim 1.6 \mu\text{m}$ . Additionally, the born time of S1 converges slower than L1 in the small  $\tilde{\omega}$  region. When  $\tilde{\omega} \approx 1$  we observe that the born time of S1 changes significantly from  $34^\circ$  ( $0.8 \mu\text{m}$  case) to  $48^\circ$  (long wavelength case).

From equation (103) one can deduce that

$$\operatorname{Im}\{t'_s\} = \frac{\beta_s}{\omega_L} \approx \frac{\gamma}{\omega_L \cos \alpha_s} = \frac{\sqrt{2I_p}}{E_0 \cos \alpha_s} = \frac{\sqrt{2I_p}}{E_s}. \quad (106)$$

Here  $E_s = E_0 \cos \alpha_s = E_0 \cos(\omega_L \operatorname{Re}\{t'_s\})$  is the electric field right at the born time. When  $\gamma \ll 1$ , during the tunneling process the electric field can be treated as quasi-static with the strength  $E_s$ . Equation (106) indicates that the imaginary part of  $t'_s$  can be interpreted as a timescale of quantum tunneling [22]. Figure 15(a) verifies that as the wavelength increases,  $\operatorname{Im}\{t'_s\}$  converges to  $\frac{\sqrt{2I_p}}{E_0 \cos \theta'_c}$  (black curve) predicted by equation (106). Figure 15(b) shows that for long wavelengths the imaginary part of the recombination time  $\operatorname{Im}\{t_s\}$  quickly converges to zero, which validates the approximations made in the above derivation.

Starting from equation (70), for a long quantum-orbit ( $\alpha_s < 17^\circ$ ), when  $\gamma \ll 1$ ,  $\operatorname{Im}\{\Theta_s\}$  can be approximated as

$$\begin{aligned} \operatorname{Im}\{\Theta_s\} &\approx \frac{2U_p}{\omega_L} \left\{ -\beta_s \left[ \gamma^2 + \frac{1}{2} - \sin^2 \alpha_s \cosh^2 \beta_s \right] \right. \\ &\quad \left. + \frac{1}{2} \cos 2\alpha_s \sinh \beta_s \cosh \beta_s \right\} \\ &\approx \frac{2U_p}{\omega_L} \left\{ -\left( \frac{\gamma}{\cos \alpha_s} - \frac{\gamma^3}{6 \cos^3 \alpha_s} \right) \left[ \gamma^2 + \frac{1}{2} - \sin^2 \alpha_s \right] \right. \\ &\quad \left. \times \left( 1 + \frac{\gamma^2}{\cos^2 \alpha_s} \right) + \frac{1}{2} \cos 2\alpha_s \frac{\gamma}{\cos \alpha_s} \left( 1 + \frac{\gamma^2}{2 \cos^2 \alpha_s} \right) \right\} \\ &\approx -\frac{2U_p \gamma}{\omega_L \cos \alpha_s} \left\{ \gamma^2 + \frac{1}{2} - \sin^2 \alpha_s - \frac{\gamma^2 \sin^2 \alpha_s}{\cos^2 \alpha_s} \right. \\ &\quad \left. - \frac{\gamma^2}{12 \cos^2 \alpha_s} + \frac{\gamma^2 \sin^2 \alpha_s}{6 \cos^2 \alpha_s} - \frac{1}{2} \cos 2\alpha_s - \frac{1}{4} \frac{\gamma^2 \cos 2\alpha_s}{\cos^2 \alpha_s} \right\} \\ &= -\frac{2U_p \gamma^3}{\omega_L \cos \alpha_s} \left\{ 1 - \frac{5 \sin^2 \alpha_s}{6 \cos^2 \alpha_s} - \frac{1}{12 \cos^2 \alpha_s} - \frac{1 \cos 2\alpha_s}{4 \cos^2 \alpha_s} \right\} \\ &= -\frac{4U_p \gamma^3}{3\omega_L \cos \alpha_s} (1 - \tan^2 \alpha_s) \approx -\frac{(2I_p)^{3/2}}{3E_0 \cos \alpha_s}. \end{aligned} \quad (107)$$

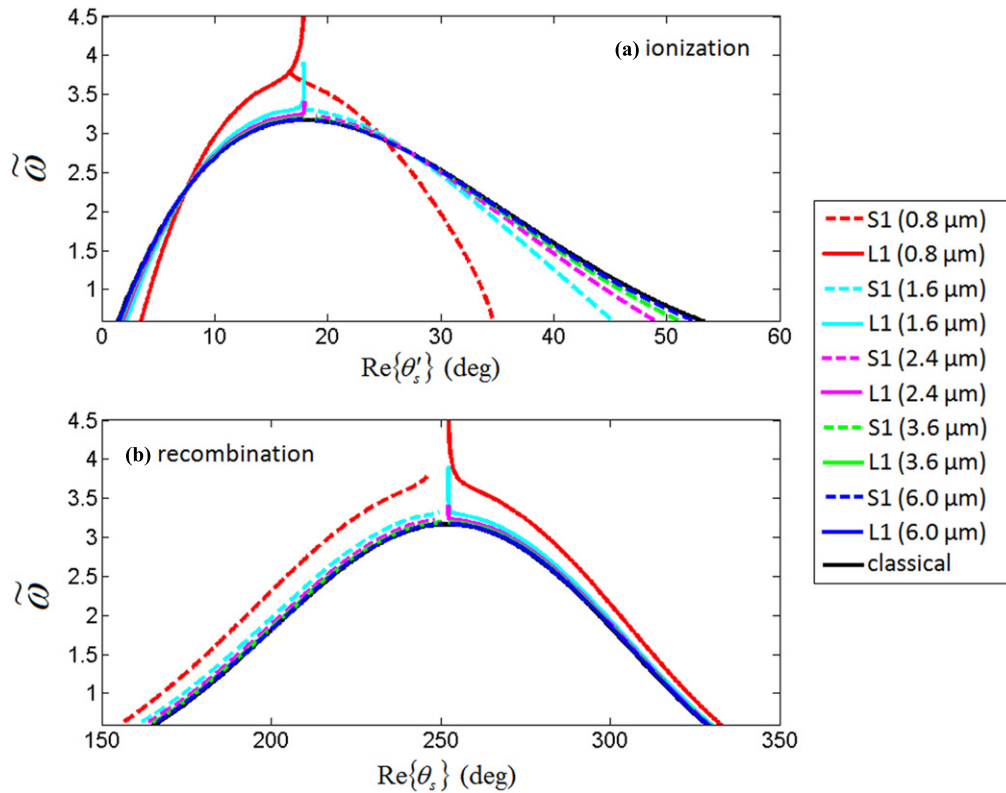


**Figure 14.** The real part of (a) ionization time and (b) recombination time for the long (L1) and short (S1) orbit of the first return as functions of  $\tilde{\omega}$ , obtained by solving equations (66) and (67) for wavelengths [0.8 – 6.0]  $\mu\text{m}$ , peak intensity  $1.5 \times 10^{14} \text{ W cm}^{-2}$ , argon target ( $I_p = 15.76 \text{ eV}$ ). The classical born and return time are also shown as solid black curves.

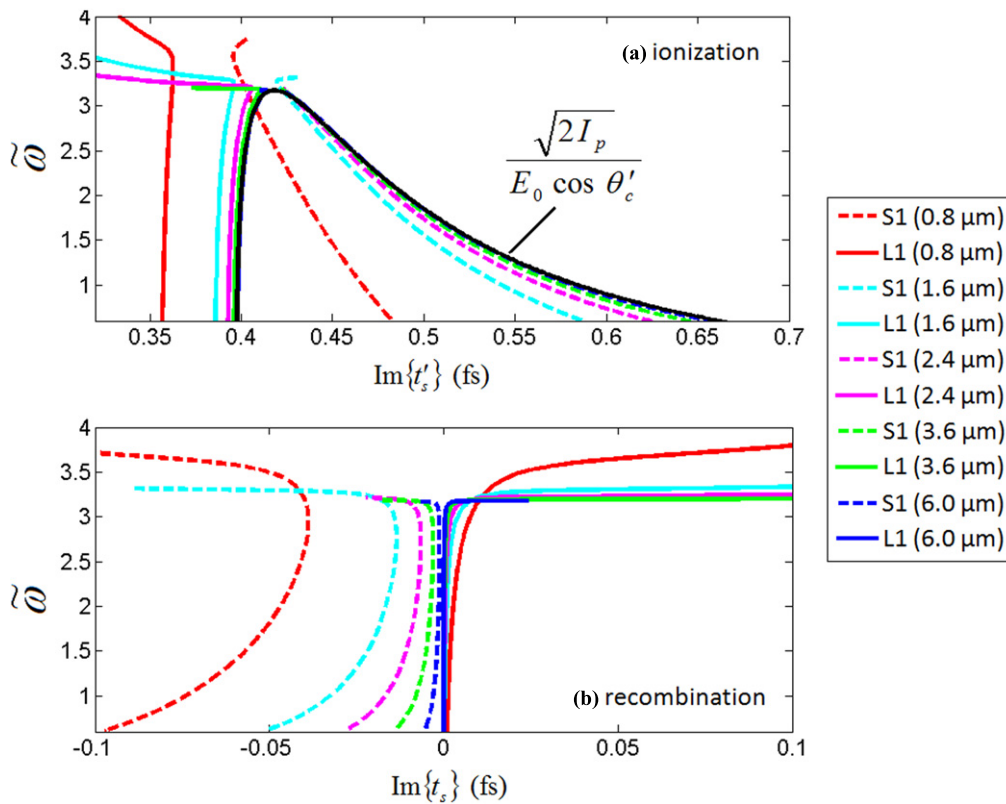


**Figure 15.** (a)  $\text{Im}\{t'_s\}$  and (b)  $\text{Im}\{t_s\}$  for the long and short orbits of the first return as functions of  $\tilde{\omega}$  obtained by solving equations (66) and (67) for wavelengths [0.8 – 6.0]  $\mu\text{m}$ . Other parameters are the same as in figure 14. The solid black curve in (a) shows the tunneling time given in equation (106) with  $\alpha_s$  replaced by the classical born time  $\theta'_c$ .

From equation (47), contribution from this quantum-orbit to HHG spectrum depends on an exponential factor

$$|D_{\text{XS}}(\omega)|^2 \propto e^{2 \text{Im}\{\Theta_s\}} \approx e^{-\frac{2(2I_p)^{3/2}}{3E_0 \cos \alpha_s}} = e^{-\frac{2(2I_p)^{3/2}}{3E_s}}. \quad (108)$$

The exponential factor in equation (108) is similar to a Landau-Dykhne type of tunneling ionization for an atom in a static field  $E_s$  [22, 78]. Therefore the quantum orbits theory can account for the tunneling ionization rate in its electron wave packet. The derivation of  $\text{Im}\{\Theta_s\}$  for a short orbit is much more complicated than the derivation of equation (107). The former requires us to approximate the imaginary part of the recombination time  $\text{Im}\{\theta_s\}$  to the order of  $\gamma^3$  rather than simply zero. Nevertheless for long wavelengths it is still reasonable to treat the electric field as quasi-static at the born time of the short orbit, thus the tunneling ionization rate equation (108) remains valid for the short orbits as well. This point has been verified in figure 16 which shows that, as the laser wavelength increases,  $\text{Im}\{\Theta_s\}$  converges to the factor  $-\frac{(2I_p)^{3/2}}{3E_0 \cos \theta'_c}$  (solid black curve) for both long and short orbits. We remark that the same exponential factor was obtained in [80] through a different approach. There, the vector potential was approximated to be linear near the maximum of the electric field.

### 3.2. Electron wave packet and scaling law at long wavelengths

Based on equations (49)–(51), (62) and (63) one can derive

$$|\det(S'')| = \frac{E_0^4 |G_{11}G_{22} - G_{12}G_{21}|}{\omega_L^2 |\theta_s - \theta'_s|^2}, \quad (109)$$

where

$$G_{11}(\theta'_s, \theta_s) = -\left(g(\theta'_s, \theta_s) + \sin \theta_s\right)^2 + (\theta_s - \theta'_s) \cos \theta'_s \left[g(\theta'_s, \theta_s) + \sin \theta_s\right], \quad (110)$$

$$G_{22}(\theta'_s, \theta_s) = -\left(g(\theta'_s, \theta_s) + \sin \theta'_s\right)^2 - (\theta_s - \theta'_s) \cos \theta'_s \left[g(\theta'_s, \theta_s) + \sin \theta'_s\right], \quad (111)$$

$$G_{12}(\theta'_s, \theta_s) = G_{21}(\theta'_s, \theta_s) = \left(g(\theta'_s, \theta_s) + \sin \theta_s\right) \left(g(\theta'_s, \theta_s) + \sin \theta'_s\right), \quad (112)$$

and

$$g(\theta'_s, \theta_s) = \frac{\cos \theta_s - \cos \theta'_s}{\theta_s - \theta'_s}. \quad (113)$$

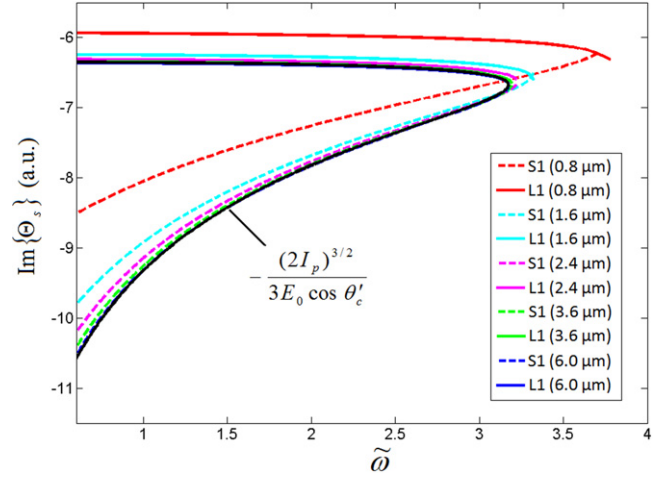


**Figure 16.**  $\text{Im}\{\Theta_s\}$  for the long and short orbit of the first return as the function of  $\tilde{\omega}$  given by equation (70) for wavelengths from 0.8  $\mu\text{m}$  to 6.0  $\mu\text{m}$ . Other parameters are the same as in figure 14. The solid black curve shows the factor given in equation (107) where  $\alpha_s$  is replaced by the classical born time  $\theta'_c$ .

By combining with equations (66) and (67) we get

$$\begin{aligned} & G_{11}G_{22} - G_{12}G_{21} \\ &= \left(g(\theta'_s, \theta_s) + \sin \theta'_s\right) \left(g(\theta'_s, \theta_s) + \sin \theta_s\right) \\ &\quad \times (\theta_s - \theta'_s)^2 \cos \theta'_s \left(\frac{\sin \theta_s - \sin \theta'_s}{\theta_s - \theta'_s} - \cos \theta'_s\right) \\ &= \pm i \gamma \sqrt{\frac{\tilde{\omega}}{2}} (\theta_s - \theta'_s)^2 \cos \theta'_s \left(\frac{\sin \theta_s - \sin \theta'_s}{\theta_s - \theta'_s} - \cos \theta'_s\right). \end{aligned} \quad (114)$$

Thus

$$|\det(S'')| = \frac{\gamma E_0^4}{\omega_L^2} \sqrt{\frac{\tilde{\omega}}{2}} |\cos \theta'_s| \left| \frac{\sin \theta_s - \sin \theta'_s}{\theta_s - \theta'_s} - \cos \theta'_s \right|. \quad (115)$$

Additionally, we notice equations (52) and (53),

$$|d_x(p_s + A(t'_s))| = |d_x(i\sqrt{2I_p})|, \quad (116)$$

$$\begin{aligned} |d_x^*(p_s + A(t_s))| &= \left| d_x \left( \sqrt{2(\omega - I_p)} \right) \right| \\ &= \left| d_x \left( \sqrt{2\tilde{\omega}U_p} \right) \right|. \end{aligned} \quad (117)$$

Substituting the above results into equation (47) one can rewrite the harmonic spectrum from a particular quantum-

orbit as

$$\begin{aligned}
 |D_{xs}(\omega)|^2 &\propto \frac{1}{|\det(S'')|} \left| \frac{\omega_L}{\theta_s - \theta'_s} \right|^3 \left| d_x(\sqrt{2\tilde{\omega}U_p}) \right|^2 \\
 &\times E_0^2 |\cos \theta'_s|^2 e^{-\frac{2(2I_p)^{3/2}}{3E_0 \cos \theta'_s}} \\
 &\propto \frac{\omega_L^5}{\gamma E_0^2 \sqrt{\tilde{\omega}}} \left| d_x(\sqrt{2\tilde{\omega}U_p}) \right|^2 f_s(\theta'_s, \theta_s) \\
 &\propto \lambda^{-4} \tilde{\omega}^{-1/2} E_0^{-1} \left| d_x\left(\frac{E_0 \sqrt{2\tilde{\omega}}}{4\pi c} \lambda\right) \right|^2 f_s(\theta'_s, \theta_s). \quad (118)
 \end{aligned}$$

Here  $f_s(\theta'_s, \theta_s)$  is a function that depends on  $(\theta'_s, \theta_s)$ . Note that here and in the following we omit the factor  $\left| d_x(i\sqrt{2I_p}) \right|^2$ , which is a constant for a given target. Since saddle point solutions  $(\theta'_s, \theta_s)$  relies on  $\tilde{\omega}$  and  $\gamma \propto \lambda^{-1}$ ,  $f_s(\theta'_s, \theta_s)$  can also be treated as a function of  $\tilde{\omega}$  and  $\lambda$  which reads

$$\begin{aligned}
 F_s(\tilde{\omega}, \lambda) &= f_s(\theta'_s, \theta_s) \\
 &= \frac{|\cos \theta'_s| e^{-\frac{2(2I_p)^{3/2}}{3E_0 \cos(\theta'_s)}}}{\left| \frac{\sin \theta_s - \sin \theta'_s}{\theta_s - \theta'_s} - \cos \theta'_s \right| |\theta_s - \theta'_s|^3}. \quad (119)
 \end{aligned}$$

Equation (118) shows that the wavelength scaling of  $|D_{xs}(\omega)|^2$  at a fixed scaled energy  $\tilde{\omega}$  depends on the form of  $d_x(p)$  and thus on the target, as discussed in [61]. Following the idea of QRS theory [46] as discussed in section 2.3 we can get rid of the target-dependent transition dipole and only study the wavelength scaling of the returning electron wave packet. For convenience here we define the wave packet  $W(\omega)$  as the HHG yield  $P(\omega)$  divided by the photo-recombination cross section  $\sigma(\omega)$

$$\begin{aligned}
 W(\omega) &\propto \frac{P(\omega)}{\sigma(\omega)} = \frac{\omega^4 |D_x(\omega)|^2}{\frac{4\pi^2 \omega^3}{cp} |d_x(p)|^2} \\
 &= \frac{c}{4\pi^2} \frac{\omega \sqrt{2(\omega - I_p)} |D_x(\omega)|^2}{\left| d_x\left(\sqrt{2(\omega - I_p)}\right) \right|^2}. \quad (120)
 \end{aligned}$$

Then the electron wave packet of a particular quantum-orbit follows (assuming  $\omega \gg I_p$ )

$$\begin{aligned}
 W_s(\tilde{\omega}) &\propto \frac{\tilde{\omega} U_p \sqrt{2\tilde{\omega} U_p} |D_{xs}(\omega)|^2}{\left| d_x(\sqrt{2\tilde{\omega} U_p}) \right|^2} \\
 &\propto (\tilde{\omega} U_p)^{3/2} \lambda^{-4} \tilde{\omega}^{-1/2} E_0^{-1} F_s(\tilde{\omega}, \lambda) \\
 &\propto \lambda^{-1} \tilde{\omega} E_0^2 F_s(\tilde{\omega}, \lambda). \quad (121)
 \end{aligned}$$

For very long wavelength we can expect that  $\gamma \rightarrow 0$  and  $(\theta'_s, \theta_s)$  converges to its classical counterpart  $(\theta'_c, \theta_c)$ , thus  $F_s(\tilde{\omega}, \lambda)$  will reduce to a wavelength independent factor  $\tilde{F}_s(\tilde{\omega})$

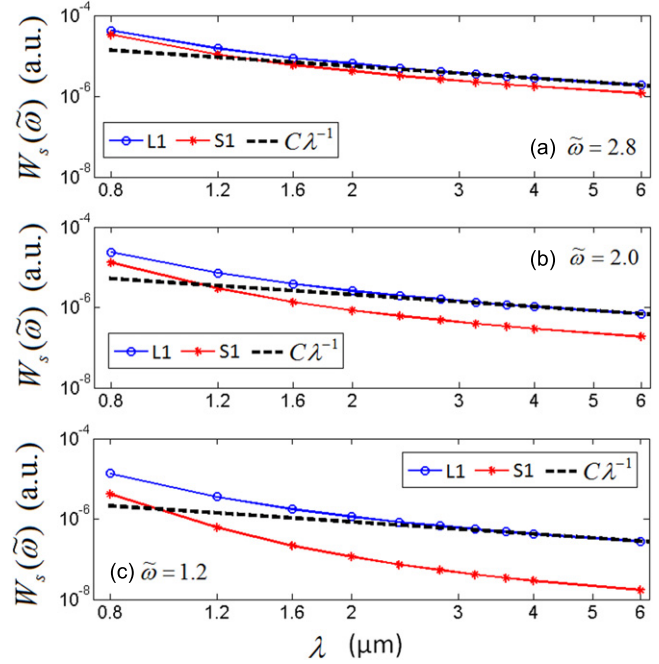


**Figure 17.** Wavelength scaling of the electron wave packet of the long and short orbit in the first return, at (a)  $\tilde{\omega} = 2.8$  (b)  $\tilde{\omega} = 2.0$  (c)  $\tilde{\omega} = 1.2$ . Other parameters are the same as in figure 14.

which reads

$$\begin{aligned}
 \tilde{F}_s(\tilde{\omega}) &= f_s(\theta'_c, \theta_c) \\
 &= \frac{|\cos \theta'_c| e^{-\frac{2(2I_p)^{3/2}}{3E_0 \cos \theta'_c}}}{\left| \frac{\sin \theta_c - \sin \theta'_c}{\theta_c - \theta'_c} - \cos \theta'_c \right| |\theta_c - \theta'_c|^3}. \quad (122)
 \end{aligned}$$

Therefore in the region of sufficiently long wavelength the electron wave packet follows

$$W_s(\tilde{\omega}) \propto \lambda^{-1} \tilde{\omega} E_0^2 \tilde{F}_s(\tilde{\omega}). \quad (123)$$

Figure 17 shows the  $\lambda$  scaling of the electron wave packet for both short and long quantum orbits at three  $\tilde{\omega}$  values. From equation (121), at a fixed scaled energy  $\tilde{\omega}$ ,  $W_s \propto \lambda^{-1} F_s(\tilde{\omega}, \lambda)$ . For  $\lambda \lesssim 2.0 \mu\text{m}$ , the scaling law deviates from  $\lambda^{-1}$ , indicating some dependence of  $F_s(\tilde{\omega}, \lambda)$  on  $\lambda$ . From  $0.8 \mu\text{m}$  to  $2.0 \mu\text{m}$  the wave packet drops quickly, especially for the short orbits at energies  $\tilde{\omega} = 1.2$ . On the other hand, as the wavelength increases beyond about  $2.4 \mu\text{m}$ , one can observe a rough  $\lambda^{-1}$  scaling law for both long and short orbits and for all  $\tilde{\omega}$  values. This  $\lambda^{-1}$  dependence is predicted by equation (123). This general behavior has been confirmed by the TDSE calculations for different atoms [131].

Next we study the profile of electron wave packet as a function of  $\tilde{\omega}$ . For convenience, we define a scaled wave packet as  $\tilde{W}_s = \lambda W_s$ . According to equation (121),  $\tilde{W}_s$  has a  $\lambda$  dependent profile  $\tilde{\omega} F_s(\tilde{\omega}, \lambda)$ . As  $\lambda$  increases, equation (123) predicts that this profile will converge to a universal form  $\tilde{\omega} \tilde{F}_s(\tilde{\omega})$ . The convergence of L1 and S1 wave packets is shown in figure 18. It can be shown that the wave packets of

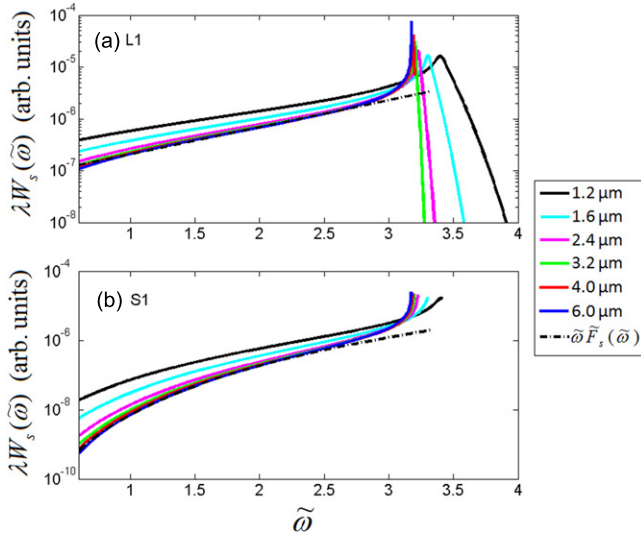


**Figure 18.** The electron wave packet of (a) long orbit and (b) short orbit at different wavelengths. Other parameters are the same as in figure 14. Wave packets have been rescaled by a factor of  $\lambda$  in order to show the convergence. The dot-dashed black curve shows the factor  $\tilde{\omega}\tilde{F}_s(\tilde{\omega})$ .

higher order quantum orbits also converge in a similar fashion. One can observe that S1 wave packet converges somewhat slower than L1, which is consistent with the behavior of ionization time for S1 and L1 orbits (see figure 14(a)). The agreement with the ‘classical limit’ (dot-dashed curve) gets worse near the cutoff. This is probably due to the influence of the artificial divergence imposed by the saddle-point approximation. We further note that, except very close to the cutoff, the ratio of the contributions from the short to long orbits decreases, as the wavelength increases, before it eventually converges to the ‘classical limit’. A similar trend has been found in the TDSE results reported in [131], where the convergence to a universal limit was found as soon as above  $\lambda \approx 3 \mu\text{m}$ .

Figure 19 shows the factor  $\tilde{F}_s(\tilde{\omega})$  for each quantum-orbit up to the third return.  $\tilde{F}_s(\tilde{\omega})$  for S1 orbit decreases rapidly from higher plateau to lower plateau, while  $\tilde{F}_s(\tilde{\omega})$  for other orbits are relatively more flat. We can deduce that for very long wavelengths L1 is the dominant orbit to the total wave packet, and higher order returns, especially the S2 orbit, also have considerable contribution. The role of higher order returns discussed here is in good agreement with the observation in [132–134].

We can also approximately derive the wavelength scaling law at a fixed absolute photon energy  $\omega$  in the long wavelength region. For that purpose, we first approximately fit the factor  $\tilde{F}_s(\tilde{\omega})$  as  $\tilde{F}_{S1}(\tilde{\omega}) \propto \tilde{\omega}^{3.7}$  for the short orbit and  $\tilde{F}_{L1}(\tilde{\omega}) \propto \tilde{\omega}^{0.8}$  for the long orbit, see figure 19. Using equation (123), we get for the long orbit

$$W_{L1}(\omega) \propto \lambda^{-1}\tilde{\omega}^{1.8} \propto \lambda^{-1}U_p^{-1.8} \propto \lambda^{-4.6}, \quad (124)$$

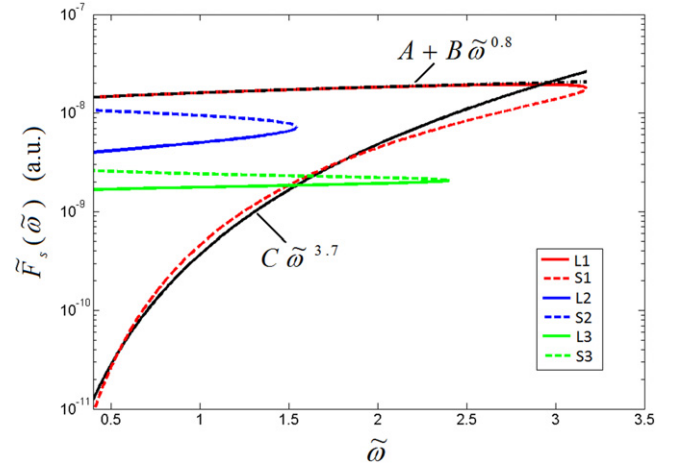


**Figure 19.** The factor  $\tilde{F}_s(\tilde{\omega})$  given in equation (122) for different quantum orbits up to the third return.

and for the short orbit

$$W_{S1}(\omega) \propto \lambda^{-1}\tilde{\omega}^{4.7} \propto \lambda^{-1}U_p^{-4.7} \propto \lambda^{-10.4}. \quad (125)$$

Note that, by definition equation (120), at a fixed absolute photon energy  $\omega$ , the wavelength scaling of HHG yield  $P_s(\omega)$  is the same as the scaling of electron wave packet given in equations (124) and (125). Since HHG at single atom level is mostly dominated by the long orbit L1 (see figure 19), the scaling law for the total HHG yield (from all quantum orbits) is only slightly different from equation (124). In fact, the scaling law  $\lambda^{-4.2}$  was obtained in [131] for  $\lambda$  in [3.0 – 6.0]  $\mu\text{m}$ , when the wave packet, as a function of  $\tilde{\omega}$  scales as approximately  $\lambda^{-1.2}$ . In the truly long wavelength limit we have  $W(\tilde{\omega}) \propto \lambda^{-1}$ , (see equation (123) and also the discussion in [131]), which would lead to a scaling  $W(\omega) \propto \lambda^{-4}$  for a fixed absolute energy  $\omega$ . Note that the apparent discrepancy, as compared to the scaling law of  $\lambda^{-(5-6)}$  reported earlier [61, 132, 135] has been mostly resolved [136] as due to the different definitions for HHG yield used in these papers as compared to [131] and the present paper. Indeed, their definition, i.e., HHG yield per unit time, differs from ours by a factor of  $T^{-1} \propto \lambda^{-1}$ .

The universal wave packet in the long wavelength limit as given by equations (123) and (122) and its approximate fitting shown in figure 19 can be used as simple estimates for realistic HHG simulation with mid-infrared lasers. Although the analysis presented here is for a monochromatic driving laser, it can also be performed, in principle, for the case of short pulses.

#### 4. Macroscopic effect on HHG in the gas medium

To simulate experimental HHG measurements, propagation of the fundamental and high-harmonic fields in the medium needs to be considered, and further propagation of XUV pulse after it exits the gas medium should also be taken into account. In this section we briefly describe our theoretical

framework for the macroscopic treatment of HHG and illustrate some results. The (microscopic) induced dipole considered in the previous sections enters the Maxwell's wave equation as the source term. We remark that under certain conditions the concept of returning electron wave packet can be extended to macroscopic case [137]. In other words, the macroscopic HHG signal can be presented as a product of a macroscopic wave packet (MWP) and photo-recombination cross section [137].

#### 4.1. Theoretical approach

**4.1.1. Propagation of the fundamental laser field.** In an ionizing gas medium, a driving infrared laser is affected by plasma defocusing, diffraction, refraction, and nonlinear self-focusing. The evolution of laser pulse in such a medium is governed by the three-dimensional (3-D) Maxwell's wave equation (in SI units) [138–142]

$$\begin{aligned} \nabla^2 E_1(r, z, t) - \frac{1}{c^2} \frac{\partial^2 E_1(r, z, t)}{\partial t^2} &= \mu_0 \frac{\partial J_{\text{abs}}(r, z, t)}{\partial t} \\ &+ \frac{\omega_0^2}{c^2} (1 - \eta_{\text{eff}}^2) E_1(r, z, t), \end{aligned} \quad (126)$$

where  $E_1(r, z, t)$  is the transverse electric field of the laser pulse with the central frequency  $\omega_0$ . In cylindrical coordinates,  $\nabla^2 = \nabla_{\perp}^2 + \partial^2/\partial z^2$ , where  $z$  is the axial propagation direction. The effective refractive index  $\eta_{\text{eff}}$  of the gas medium can be written as

$$\eta_{\text{eff}}(r, z, t) = \eta_0(r, z, t) + \eta_2 I(r, z, t) - \frac{\omega_p^2(r, z, t)}{2\omega_0^2}. \quad (127)$$

The first term  $\eta_0 = 1 + \delta_1 - i\beta_1$  accounts for refraction ( $\delta_1$ ) and absorption ( $\beta_1$ ) by the neutral atoms, the second term accounts for the optical Kerr nonlinearity which depends linearly on laser intensity  $I(t)$ , and the third term accounts for the free electrons, expressed in terms of plasma frequency,  $\omega_p(t) = [e^2 n_p(t)/(\varepsilon_0 m_e)]^{1/2}$ , where  $m_e$  and  $e$  are the mass and charge of an electron, respectively,  $\varepsilon_0$  is the permittivity of free space, and  $n_e(t)$  is the density of free electrons. The absorption due to the ionization of the gas medium is expressed as [138, 143]

$$J_{\text{abs}}(t) = \frac{\gamma(t) n_0(t) I_p E_1(t)}{|E_1(t)|^2}, \quad (128)$$

where  $\gamma(t)$  is the ionization rate,  $I_p$  the ionization potential, and  $n_0(t)$  the density of remnant neutral atoms.

The small absorption effect ( $\beta_1$ ) on the fundamental laser field caused by neutral atoms is usually neglected. With only the real terms in the refractive index  $\eta_{\text{eff}}$ , equation (126) can

be written as

$$\begin{aligned} \nabla^2 E_1(r, z, t) - \frac{1}{c^2} \frac{\partial^2 E_1(r, z, t)}{\partial t^2} &= \mu_0 \frac{\partial J_{\text{abs}}(r, z, t)}{\partial t} \\ &+ \frac{\omega_p^2}{c^2} E_1(r, z, t) - 2 \frac{\omega_0^2}{c^2} [\delta_1 + \eta_2 I(r, z, t)] E_1(r, z, t). \end{aligned} \quad (129)$$

By going to a moving coordinate frame ( $z' = z$  and  $t' = t - z/c$ ) and neglecting  $\partial^2 E_1/\partial z'^2$  since the  $z'$  dependence of the electric field is very slow, we obtain [144]

$$\begin{aligned} \nabla_{\perp}^2 E_1(r, z', t') - \frac{2}{c} \frac{\partial^2 E_1(r, z', t')}{\partial z' \partial t'} &= \mu_0 \frac{\partial J_{\text{abs}}(r, z', t')}{\partial t'} \\ &+ \frac{\omega_p^2}{c^2} E_1(r, z', t') - 2 \frac{\omega_0^2}{c^2} [\delta_1 + \eta_2 I(r, z', t')] E_1(r, z', t'). \end{aligned} \quad (130)$$

We apply Fourier transform to eliminate the temporal derivative in equation (130). In the frequency domain, the equation becomes

$$\nabla_{\perp}^2 \tilde{E}_1(r, z', \omega) - \frac{2i\omega}{c} \frac{\partial \tilde{E}_1(r, z', \omega)}{\partial z'} = \tilde{G}(r, z', \omega), \quad (131)$$

where

$$\tilde{E}_1(r, z', \omega) = \hat{F} [E_1(r, z', t')], \quad (132)$$

and

$$\begin{aligned} \tilde{G}(r, z', \omega) &= \hat{F} \left\{ \mu_0 \frac{\partial J_{\text{abs}}(r, z', t')}{\partial t'} + \frac{\omega_p^2}{c^2} E_1(r, z', t') \right. \\ &\left. - 2 \frac{\omega_0^2}{c^2} [\delta_1 + \eta_2 I(r, z', t')] E_1(r, z', t') \right\}, \end{aligned} \quad (133)$$

where  $\hat{F}$  is the Fourier transform operator acting on the temporal coordinate.

The plasma frequency  $\omega_p(r, z', t')$  depends on the free-electron density  $n_e(t')$  which can be calculated from

$$n_p(r, z', t') = N_0 \left\{ 1 - \exp \left[ - \int_{-\infty}^{t'} \gamma(r, z', \tau) d\tau \right] \right\}, \quad (134)$$

where  $N_0$  is the initial neutral atom density, and  $\gamma(r, z', \tau)$  is the ionization rate calculated by Ammosov-Delone-Krainov (ADK) theory [78, 145]. The refraction coefficient  $\delta_1$ , depending on the pressure and temperature of the gas medium, is obtained from the Sellmeier equation [146, 147]. The second-order refractive index  $\eta_2$ , also depending on gas pressure, can be calculated through third-order susceptibility  $\chi^{(3)}$ , which can be measured from experiments [148–151]. Note that the relationship between  $\eta_2$  and  $\chi^{(3)}$  in Koga *et al* [152] differs from that in Boyd [153] since the latter is derived by using time-averaged intensity of the optical field.

The time profile of the fundamental laser pulse at the entrance of a gas jet ( $z' = z_{\text{in}}$ ) is usually assumed to be cosine-squared or Gaussian, and the spatial dependence is truncated Bessel [154–157], truncated Gaussian [158, 159], or Gaussian, while the pressure distribution within the

interaction region can be assumed as uniform, Gaussian or Lorentzian according to the experimental conditions. As presented in [137], when both the gas pressure and laser intensity are low, the source term in equation (126) can be taken as zero, and the fundamental laser field is not modified through the gas medium.

Assuming a Gaussian beam in space, its electric field  $E_g(r, z')$  is given by

$$E_g(r, z') = \frac{bE_0}{b + 2iz'} \exp\left(-\frac{kr^2}{b + 2iz'}\right) = |E_g(r, z')| e^{i\phi_{laser}(r, z')}. \quad (135)$$

Here  $E_0$  is the laser peak field at the focus,  $b = 2\pi w_0^2/\lambda_0$  is the confocal parameter, where  $w_0$  is the beam waist at the focus and  $\phi_{laser}$  is the laser geometric phase ('Gouy' phase in general). The fundamental laser pulse can be approximately written in analytical form [137, 139]:

$$E_1(r, z', t') = \text{Re} \left[ E_g(r, z') A(r, z', t') e^{-i(\omega_0 t' + \varphi_{ce})} \right], \quad (136)$$

where  $\varphi_{ce}$  represents the carrier-envelope phase. If the temporal envelope is assumed to be cosine-squared function [137], then

$$A(r, z', t') = \cos^2 \left\{ \frac{\pi \left[ t' - \phi_{laser}(r, z')/\omega_0 \right]}{\tau_p} \right\}, \quad (137)$$

where  $\tau_p$  is the total duration of the laser pulse and is equal to 2.75 times  $\tau_w$ , the full width at half maximum (FWHM) of laser's intensity. One can also take the Gaussian envelope in time,

$$A(r, z', t') = \exp \left[ -2 \ln 2 \frac{\left( t' - \phi_{laser}(r, z')/\omega_0 \right)^2}{\tau_w^2} \right]. \quad (138)$$

**4.1.2. Propagation of the high-harmonic field.** The 3-D propagation equation of the high-harmonic field is described in [138, 139, 144, 160]

$$\nabla^2 E_h(r, z, t) - \frac{1}{c^2} \frac{\partial^2 E_h(r, z, t)}{\partial t^2} = \mu_0 \frac{\partial^2 P(r, z, t)}{\partial t^2}, \quad (139)$$

where  $P(r, z, t)$  is the polarization caused by the applied optical field  $E_1(r, z, t)$ . In this equation, the free-electron dispersion is neglected because the plasma frequency is much smaller than the frequencies of high harmonics. Again going to a moving coordinate frame and neglecting  $\partial^2 E_h/\partial z'^2$ , equation (139) becomes

$$\nabla_{\perp}^2 E_h(r, z', t') - \frac{2}{c} \frac{\partial^2 E_h(r, z', t')}{\partial z' \partial t'} = \mu_0 \frac{\partial^2 P(r, z', t')}{\partial t'^2}. \quad (140)$$

We eliminate the temporal derivative by Fourier transform. In the frequency domain it becomes

$$\nabla_{\perp}^2 \tilde{E}_h(r, z', \omega) - \frac{2i\omega}{c} \frac{\partial \tilde{E}_h(r, z', \omega)}{\partial z'} = -\omega^2 \mu_0 \tilde{P}(r, z', \omega), \quad (141)$$

where

$$\tilde{E}_h(r, z', \omega) = \hat{F} [E_h(r, z', t')], \quad (142)$$

and

$$\tilde{P}(r, z', \omega) = \hat{F} [P(r, z', t')]. \quad (143)$$

The source term on the right-hand side of equation (141) describes the response of the medium to the laser field and includes both linear and nonlinear terms. It is convenient to separate the polarization field into linear and nonlinear components,  $\tilde{P}(r, z', \omega) = \chi^{(1)}(\omega) \tilde{E}_h(r, z', \omega) + \tilde{P}_{nl}(r, z', \omega)$ , where the linear susceptibility  $\chi^{(1)}(\omega)$  includes both linear dispersion and absorption through its real and imaginary parts, respectively. The nonlinear polarization term  $\tilde{P}_{nl}(r, z', \omega)$  can be expressed as

$$\tilde{P}_{nl}(r, z', \omega) = \hat{F} \left\{ [N_0 - n_p(r, z', t')] D(r, z', t') \right\}, \quad (144)$$

where  $n_e(r, z', t')$  is calculated from equation (134), and  $D(r, z', t')$  is the single atom induced dipole moment caused by the fundamental driving laser field.

The refractive index  $n(\omega) = \sqrt{1 + \chi^{(1)}(\omega)/\varepsilon_0}$  [153] is related to atomic scattering factors by

$$n(\omega) = 1 - \delta_h(\omega) - i\beta_h(\omega) = 1 - \frac{1}{2\pi} N_0 r_0 \lambda^2 (f_1 + if_2), \quad (145)$$

where  $r_0$  is the classical electron radius,  $\lambda$  is the XUV wavelength,  $N_0$  is again the initial neutral atom density, and  $f_1$  and  $f_2$  are atomic scattering factors which can be obtained from [161, 162]. Note that  $\delta_h(\omega)$  and  $\beta_h(\omega)$  account for the dispersion and absorption of the medium on the high harmonics, respectively.

Finally equation (141) can be written as

$$\nabla_{\perp}^2 \tilde{E}_h(r, z', \omega) - \frac{2i\omega}{c} \frac{\partial \tilde{E}_h(r, z', \omega)}{\partial z'} - \frac{2\omega^2}{c^2} (\delta_h + i\beta_h) \tilde{E}_h(r, z', \omega) = -\omega^2 \mu_0 \tilde{P}_{nl}(r, z', \omega),$$

where the nonlinear polarization as the source of the harmonics is explicitly given. After the propagation in the medium, we obtain the near-field harmonics at the exit face of the gas jet ( $z' = z_{out}$ ).

The two key propagation equations, i.e., equations (131) and (146), are solved using a Crank-Nicholson routine for each value of  $\omega$ . For a typical experimental setup, such as a 1 mm long gas jet located after a focused laser with the beam waist of tens of  $\mu\text{m}$ , the parameters used in the calculations

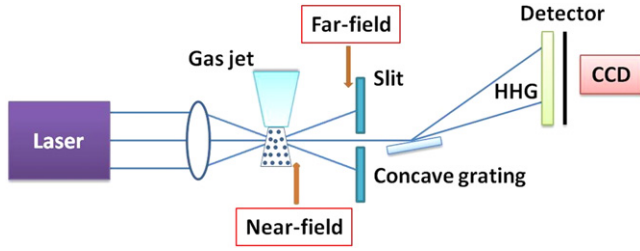


**Figure 20.** Typical configuration for measuring the HHG in the far field. Adapted from [55].

are 200 ~ 300 grid points along the radial direction and 400 grid points along the longitudinal direction.

**4.1.3. Far-field harmonic emission.** Experimentally, harmonics are not measured at the exit face of a gas medium, as shown in figure 20. They may go through a slit, an iris or a pinhole, or reflected by a mirror before they reach the detector. Far-field harmonics in free space can be obtained from near-field harmonics through a Hankel transformation [139, 163–165]

$$E_h^f(r_f, z_f, \omega) = -ik \int \frac{\tilde{E}_h(r, z', \omega)}{z_f - z'} J_0\left(\frac{kr r_f}{z_f - z'}\right) \times \exp\left[\frac{ik(r^2 + r_f^2)}{2(z_f - z')}\right] r dr, \quad (147)$$

where  $J_0$  is the zero-order Bessel function,  $z_f$  is the far-field position from the laser focus,  $r_f$  is the transverse coordinate in the far field, and the wave vector  $k$  is given by  $k = \omega/c$ . Using equation (147), we can also calculate the divergence of high harmonics. Assuming that harmonics in the far field are collected from an extended area, the power spectrum of the macroscopic harmonics at  $z_f$  is obtained by integrating harmonic yields over the area

$$S_h(\omega) \propto \iint |E_h^f(x_f, y_f, z_f, \omega)|^2 dx_f dy_f, \quad (148)$$

where  $x_f$  and  $y_f$  are the Cartesian coordinates on the plane perpendicular to the propagation direction, and  $r_f = \sqrt{x_f^2 + y_f^2}$ .

Note that detailed information on the experimental setup is involved in equation (148). To quantitatively simulate the experimental HHG spectra, not only the laser parameters such as intensity, duration, wavelength, spot, and so on, are required, but also the setup parameters in the experiment, for example, the size and location of a slit.

#### 4.2. Phase matching conditions

For efficient generation of a high-order harmonic, its phase front should match with the phase front of the fundamental laser pulse. Due to the spatiotemporal variation of laser intensity in the medium, phase matching is complicated in space and time. The phase mismatch  $\Delta k_q$  for the  $q$ th

harmonic can be written as [154]

$$\begin{aligned} \Delta k_q &= (k_q - qk_0) - K_{q,dip} \\ &= \Delta k_{q,geo} + \Delta k_{q,el} + \Delta k_{q,at} - K_{q,dip}. \end{aligned} \quad (149)$$

Here  $k_q$  and  $k_0$  are wave vectors of the harmonic and the fundamental laser fields, respectively. Since coherence length is proportional to the inverse of phase mismatch, efficient harmonic generation calls for creating conditions of minimum phase mismatch in the gas medium. There are four major source terms in equation (149): geometric phase (diffraction), free electron dispersion, neutral atom dispersion (refraction), and induced-dipole phase. Each term will be discussed in the following. Here we omit the time dependence of the phase matching, and take  $z = z'$ .

**4.2.1. Geometric dispersion.** When an intense laser is focused into a small region in space, it introduces a geometric phase (or ‘Gouy’ phase). The corresponding phase mismatch for the generated harmonic is written as

$$\Delta k_{q,geo} = k_{q,geo}(r, z) - qk_{0,geo}(r, z). \quad (150)$$

Here we only consider on-axis ( $r=0$ ) phase matching for a Gaussian beam, and assume that the fundamental laser and harmonic beams have the same geometrical phase,  $\Delta k_{q,geo}$  can be written as

$$\begin{aligned} \Delta k_{q,geo}(0, z) &\approx -(q-1)\delta k_{0,geo}(0, z) \\ &= \frac{2}{b}(q-1) \frac{1}{1 + (2z/b)^2}, \end{aligned} \quad (151)$$

where  $b$  is the confocal parameter, which has been defined in equation (135).

**4.2.2. Induced dipole phase.** The phase of high harmonic has strong dependence on laser intensity. Laser intensity variation in space results in longitudinal and transverse gradients of this phase. The contribution to the phase mismatch is

$$K_{q,dip} = \nabla \varphi_{q,dip}. \quad (152)$$

Here the intrinsic dipole phase  $\varphi_{q,dip}$  is the action accumulated by an electron during its excursion in the laser field, which is finally recombined with the atomic ion to emit the  $q$ th harmonic. To first order, this phase can be expressed as

$$\varphi_{q,dip} = -\alpha_i^q I, \quad (153)$$

where  $I$  is the instantaneous laser intensity. The proportional constant  $\alpha_{i=S,L}$  depends on ‘short’ (S) or ‘long’ (L) trajectory. For the harmonics in the plateau region,  $\alpha_{i=S}^q \approx 1 \times 10^{-14}$  rad cm<sup>2</sup>/W and  $\alpha_{i=L}^q \approx 24 \times 10^{-14}$  rad cm<sup>2</sup>/W [82, 166–168]. At the cut-off, these two trajectories merge into one, and  $\alpha_{i=S,L}^q \approx 13.7 \times 10^{-14}$  rad cm<sup>2</sup>/W.

Consider the on-axis phase mismatch of a Gaussian beam it can be written as follows:

$$\begin{aligned} \frac{\partial \varphi_{q,dip}(0, z)}{\partial z} &= -\alpha_i^q \frac{\partial I(0, z)}{\partial z} \\ &= \frac{8z}{b^2} \frac{1}{[1 + (2z/b)^2]^2} \alpha_i^q I_0, \end{aligned} \quad (154)$$

where  $I_0$  is the laser peak intensity at the focus.

**4.2.3. Plasma or free electron dispersion.** Harmonic generation is initiated by ionization. However, only a small fraction of the ionized electrons could be drive back to recombine with the parent ion to emit high energy photons. The rest are free electrons in the gas medium which will modify the refractive index. The phase mismatch caused by the presence of free electrons is

$$\begin{aligned} \Delta k_{q,el} &= k_{q,el}(r, z, t) - qk_{0,el}(r, z, t) \\ &\approx \frac{e^2 n_e(r, z, t)}{4\pi\epsilon_0 m_e c^2} q\lambda_0 = qr_0 n_e(r, z, t)\lambda_0, \end{aligned} \quad (155)$$

where  $n_e(r, z, t)$  is the spatiotemporal dependent electron density. In equation (155), free-electron dispersion for the harmonic field is neglected because the frequencies of high harmonics are much higher than the plasma frequency.

**4.2.4. Neutral atom dispersion.** Any conversion medium for harmonic generation exhibits dispersion. The refractive index of the fundamental infrared laser is different from the high harmonics. The phase mismatch is

$$\begin{aligned} \Delta k_{q,at} &= k_{q,at}(r, z, t) - qk_{0,at}(r, z, t) \\ &\approx -\frac{n_0(r, z, t)\pi\alpha_1}{\lambda_q} - n_0(r, z, t)r_0\lambda_q f_1, \end{aligned} \quad (156)$$

where  $n_0(r, z, t)$  is the neutral atom density,  $\lambda_q = \lambda_1/q$  the wavelength of the  $q$ th harmonic,  $\alpha_1$  the atomic polarizability at the fundamental wavelength  $\lambda_0$ . Here  $f_1$  is the real part of the atomic scattering factor  $f = f_1 + if_2$  [161, 162] at the harmonic wavelength  $\lambda_q$ , the imaginary part  $f_2$  is related to the absorption length  $L_{abs}$  by  $L_{abs}^{-1} = 2r_0\lambda_q n_0(r, z, t)f_2$ . In the present phase mismatch analysis, we don't include the Kerr nonlinearity since it is a higher order effect.

#### 4.3. Illustrative examples: comparison of simulations with experiments

We will show three examples, two of which the fundamental field is not much modified (Ar case and aligned  $N_2$  case), and one in which it is severely reshaped (Xe case), as the pulse propagates in the gas medium. The single-atom harmonic response is calculated using the QRS model. In the QRS calculation, the returning electron wave packet is obtained from the SFA. The transition dipole for Ar is calculated in a single active electron approximation using Muller's model potential [169]. For Xe, the photorecombination cross section is taken from the relativistic random-phase approximation (RRPA) [170] which includes multielectron correlation effect.

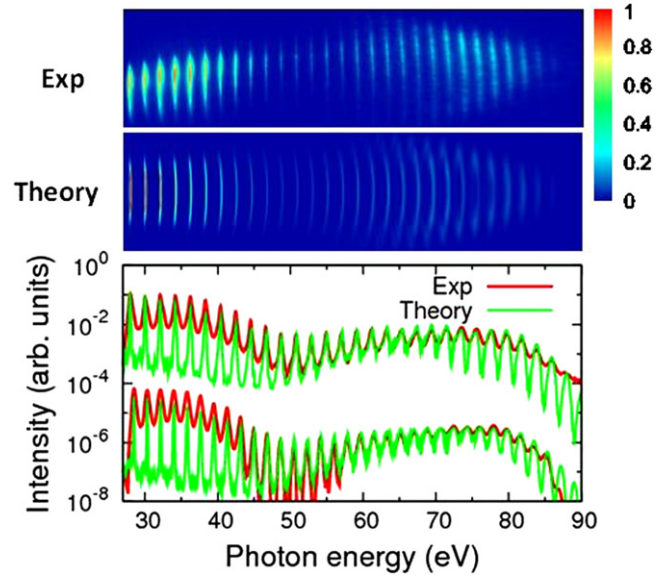


**Figure 21.** HHG spectra of Ar generated by long-wavelength lasers. Upper frame: Spatial distribution of harmonic emission versus photon energy in the far field by a 1200 nm laser. Lower frame: Comparison of experimental (red lines) and theoretical (green lines) HHG yields integrated over the vertical dimension for 1200 nm (upper curves) and 1360 nm (lower curves) lasers. Other laser parameters are given in the text. Adapted from [55].

For  $N_2$  molecules the transition dipoles are obtained from the package developed by Lucchese [171]. In the following subsections we give these examples to show how well the experimental harmonic spectra can be successfully reproduced by simulations based on the theory presented.

**4.3.1. Macroscopic HHG spectra of Ar.** We show the measured and simulated HHG spectra of Ar in figure 21. Experimental harmonics were produced by a 0.5-mm-long gas jet, which was located a few mm's after the laser focus. Harmonics emitted from the exit plane of gas jet are further propagated 24 cm and reached a vertical slit with a width of 100  $\mu\text{m}$ , see figure 20. For a 1200- (1360-) nm laser in the experiment, the beam waist at the focus is estimated to be 47.5 (52.5)  $\mu\text{m}$ , and the pulse duration is  $\sim 40$  ( $\sim 50$ ) fs. To reach the best overall fit with experimental data, laser intensity and gas pressure used in the simulations are adjusted. For the 1200 nm laser, peak intensity for the experiment (theory) is  $1.6$  ( $1.5$ )  $\times 10^{14}$   $\text{W cm}^{-2}$ , and gas pressure is 28 (84) Torr. For the 1360 nm laser, the corresponding intensity and pressure are  $1.25$  ( $1.15$ )  $\times 10^{14}$   $\text{W cm}^{-2}$  and 28 (56) Torr, respectively.

In the upper frame of figure 21, the vertical axis is the transverse spatial dimension, and the horizontal axis is photon energy. The experimental and theoretical spectra for the 1200 nm case are normalized at photon energy of 77 eV, i.e., the 75th harmonic (H75). There is a general agreement between the two spectra except for 'up-down' asymmetry in the experimental spectra, which is due to the asymmetric laser

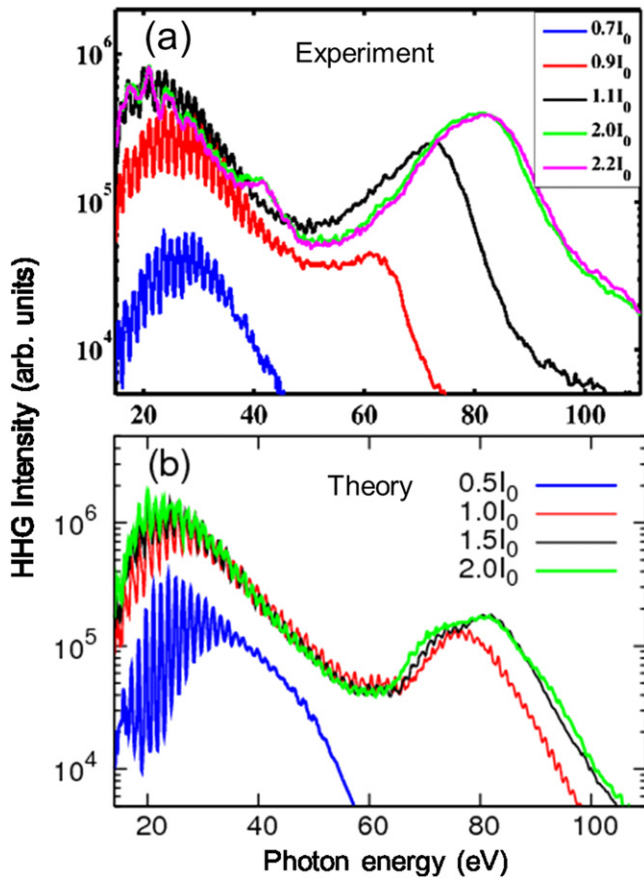


**Figure 22.** Measured (a) and simulated (b) HHG spectra of Xe generated by 1825 nm lasers for different laser intensities, where  $I_0 = 10^{14} \text{ W cm}^{-2}$ . Laser duration is 14 fs. In the experiment, CEP was not stabilized, and theoretical spectra are averaged over random values of the CEP. Adapted from [172].

beam profile. The ‘famous’ Cooper minimum is clearly seen in both experimental and theoretical spectra. Harmonic yields integrated over the vertical dimension are compared in the lower frame of figure 21. The HHG spectra for the 1360 nm pulse are also shown. In both cases, there is a good agreement (in the envelope of the spectrum) over the 30–90 eV region between theory and experiment.

Detailed discussions about other properties, such as the chirp and angular divergence of the harmonics, as well as the macroscopic wave packet and scaling of the efficiency of harmonic yields versus wavelength, can be found in [56].

**4.3.2. Macroscopic HHG spectra of Xe.** We show the measured and simulated HHG spectra of Xe in figure 22. Looking at the experimental data, one of the most striking features in figure 22(a) is the emergence of quasi-continuous harmonic spectrum as the laser intensity is increased. These continuous spectra extend over a broad range of photon energy from the cutoff at about 100 eV down to very low energy of 20–30 eV. Simulations showed that these continuum spectra indeed are capable of producing isolated attosecond pulses if proper spatial and spectral filters are applied [172, 173]. We also note that saturation occurs in

the observed spectra, where further increase of input laser intensity does not change the HHG spectrum much. This is clearly seen for laser intensities above about  $2 \times 10^{14} \text{ W cm}^{-2}$  in figure 22(a). Another striking feature is the broad enhancement in the HHG yield observed near 100 eV. This well-known enhancement is attributed to the partial photoionization cross section of Xe from 5p which is modified by the strong inter-channel coupling with photoionization from the 4d shell of Xe. Such coupling can be included only if electron correlation is appropriately included in the theory [174].

In figure 22(b) theoretical harmonic spectra for four peak laser intensities after propagation through the gas jet are shown. In the simulation, the experimental parameters including, the jet size (1 mm), the slit opening of the spectrometer (190  $\mu\text{m}$ ), the distance of the slit from the gas jet (455 mm), and the laser wavelength and pulse duration (1825 nm and 14 fs), are used. The calculated spectra have been averaged over the CEP dependence. The simulations indeed show transition to a quasi-continuous spectrum from the ‘apparent’ cutoff down to about 30 eV, as the laser intensity is increased, in agreement with the experimental finding. The saturation effect observed in the experiment is also reproduced by the simulation. Note that single-atom simulations [172] alone would not be able to explain these observations. The quasi-continuum and saturation observed in the spectra are all attributable to significant reshaping of the input laser pulses in the medium, in particular by the plasma defocusing due to high degrees of ionization.

In the simulation, the broad harmonic enhancement near 100 eV is reproduced by feeding theoretical photoionization transition dipole calculated from many-body perturbation theory [170] into the QRS. With the QRS theory, one can bypass the complexity of formulating a strong field theory that also includes many-electron correlation effect. By taking advantage of the factorization feature of the QRS, the strong field effect is reflected in the returning electron wave packet which is mostly a single-electron process, whereas the strong many-electron correlation effect is reflected in the recombination transition dipole moment. This ‘divide and conquer’ strategy not only makes the calculation much easier, it also offer the interpretation of the observed HHG spectra much more transparent.

#### 4.4. Wavelength scaling of high-order harmonics after including macroscopic propagation

To study wavelength scaling of harmonic yields in the laboratory, ideally one has to fix all other parameters that may affect the efficiency of HHG. One also needs to decide if the scaling is with respect to a given photon-energy region or the total HHG yield. In single-atom simulation, the laser parameters can be easily fixed. However, this is not the case in real experiments. Here we define a single parameter that describes the efficiency of harmonic generation. It is the ratio between the output energy (total harmonic energy) with respect to the input energy (fundamental laser energy) for different laser wavelengths. In the example shown below, we

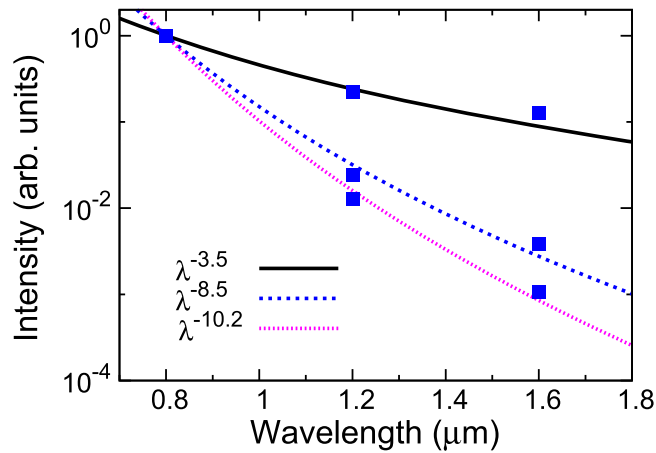


**Figure 23.** Wavelength dependence of the total integrated HHG yields above 20 eV. The results shown (from top to bottom) are for single-atom HHG, and macroscopic HHG in the near field and in the far field. The harmonic yield is normalized according to the input energy. Adapted from [56].

fix laser intensity, duration, and beam waist. Gas-jet length, position, and pressure are also kept the same. We only vary the laser wavelength from 0.8 to 1.6  $\mu\text{m}$ . The detailed parameters can be found in [56].

For single-atom harmonic generation, the input energy is set to be the same for 800-, 1200-, and 1600 nm lasers. The total harmonic yield is obtained by integrating the spectra from 20 eV up which is then taken as the total output energy. the resulting harmonic output then follows  $\lambda^{-3.5 \pm 0.5}$ , as shown in figure 23. It is generally known that phase-matching condition is more difficult to meet if longer wavelength lasers are used to drive the HHG; thus the HHG efficiency decreases further with increasing wavelength. For macroscopic harmonic generation, since the laser intensity is fixed at the center of the gas jet and the laser is focused before the gas jet, thus the input energies for the three wavelengths are different. They are calculated to be at the ratios of 1.0: 1.13: 1.31, for the 800-, 1200-, and 1600 nm lasers in this example. We assume that all the harmonics emitted in the near field are collected. From our calculation, we found that HHG yield integrated from 20 eV up scales like  $\lambda^{-8.5 \pm 0.5}$ , as shown in figure 23. For harmonics that are useful for applications, they are often collected by placing a slit in the far field. This would further reduce the scaling, like  $\lambda^{-10.2 \pm 0.2}$ , see figure 23, since harmonics generated by longer wavelength lasers are more divergent.

When considering the propagation of harmonics in the gas medium, it is easy to understand that phase matching condition for different quantum orbits are quite different [138]. Although higher order return orbits have considerable contribution to single atom harmonics, because they accumulate a relatively large phase in the continuum and they are more sensitive to laser intensity, their net contribution to the macroscopic harmonics becomes negligible after propagation. In figure 24 we separate the contributions from short orbit (S1), long orbit (L1) and higher return orbits (up to the third) to the macroscopic HHG yield. We used the induced dipole calculated from the QO method as the source term in the

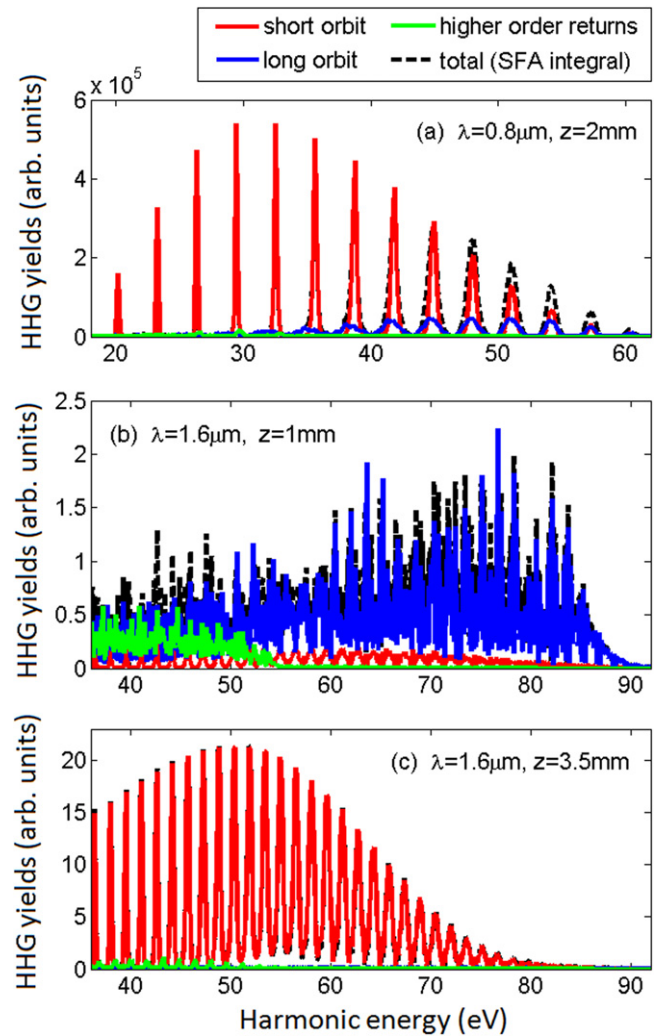


**Figure 24.** Macroscopic HHG yield after propagating in an Ar gas jet of 1 mm thick placed after the laser focus. The laser pulse has a cosine-squared envelope with 30 cycles total duration, CEP = 0. (a) 0.8  $\mu\text{m}$  laser with beam waist 25  $\mu\text{m}$ , the center of the gas jet is at  $z = 2 \text{ mm}$  where the peak intensity is  $2.0 \times 10^{14} \text{ W cm}^{-2}$  ( $U_p = 12 \text{ eV}$ ). (b) 1.6  $\mu\text{m}$  laser with beam waist 36  $\mu\text{m}$ , the center of the gas jet is at  $z = 1 \text{ mm}$  where the peak intensity is  $1.0 \times 10^{14} \text{ W cm}^{-2}$  ( $U_p = 24 \text{ eV}$ ). (c) the center of the gas jet is at  $z = 3.5 \text{ mm}$ , other parameters are the same as in (b). (b) and (c) are adapted from [131].

propagation equation. The HHG yield is defined as the integrated harmonic field intensity right at the rear face of the gas jet. The 0.8  $\mu\text{m}$  case shown in figure 24(a) is well understood: as the gas jet is placed after the laser focus, the short orbit (S1) is effectively selected, the long orbit only contributes near the cutoff. For longer wavelengths phase matching becomes more sensitive to experimental setup. Simulations for a typical setup using a tightly focused 1.6  $\mu\text{m}$  laser beam are shown in figure 24(b) and (c), with the gas jet placed at  $z = 1 \text{ mm}$  and 3.5 mm after the laser focus, respectively. For  $z = 1 \text{ mm}$  the long orbit dominates the HHG yield. Higher order returns contribute mainly below about 50 eV ( $1.5U_p + I_p$ ), which indicates that this contribution comes mostly from the second return. Good phase matching is achieved in the  $z = 3.5 \text{ mm}$  case, which resembles the

0.8  $\mu\text{m}$ ,  $z = 2\text{ mm}$  case above. Here, the HHG spectrum shows clear harmonic peaks but the cutoff is somewhat reduced. The short orbit dominates the total yield and there is hardly any signature from long orbits and higher order returns. Note that higher order returns may be important in studying sub-cycle dynamics at the single atom level and in interpreting the interference structures in angle-resolved photoelectron distributions [175]. However in the case of phase-matched high harmonic generation, high-order returns are not important.

We recall that at single atom level the HHG yield scales unfavorably with increased laser wavelength, as discussed in section 3.2. The situation gets even worse for the short orbits, which are typically weaker than long orbits, especially at lower energies, say below,  $2U_p$ . Nevertheless, good phase matching tends to select short orbits. Therefore it is very challenging to obtain efficient macroscopic harmonic emission with long wavelength driving field. In this respect, it is quite tempting to enhance the short orbits contribution by using a synthesized laser waveform. This has been suggested in [176] and will be discussed in section 5.2.

## 5. Extension of QRS to molecular targets and other applications

### 5.1. Application to HHG from molecules

The QRS can be extended to molecular targets in a straightforward manner. Again, the electron wave packet can be obtained from the SFA or its modifications for each fixed-in-space molecule. If a reference atom is used, one also needs to know the alignment dependent ionization rates (see section 2.5). Photo-recombination (or photoionization) dipole can be calculated using molecular photoionization packages such as ePolyScat [177, 178]. Although there is no formal derivation of the QRS for molecules, the model has been tested by comparison with TDSE results for molecular ion,  $\text{H}_2^+$  [48]. The model has also been well tested against various experiments for aligned linear molecules [11, 12, 46, 51, 55–58, 179] as well as polyatomic molecules [52–54]. Extensions for different polarizations and large-amplitude vibrating molecules have also been reported [51, 180, 181]. Other applications of the QRS include, for example, [49, 67, 182–186]. In fact, so far only the QRS theory has been so extensively applied to HHG from molecular targets and compared to experimental observations.

As an illustration we just show one example which has been carefully studied experimentally: the HHG spectra of perpendicularly aligned  $\text{N}_2$  molecules by a 1200 nm laser pulse, see figure 25 (see, [58]). The pulse duration (FWHM) is  $\sim 44\text{ fs}$ , laser is focused 3 mm before the 1 mm long gas jet, and the beam waist at the focus is  $\sim 40\ \mu\text{m}$ . In the far field (24 cm after the gas jet), there is a vertical slit with a width of  $100\ \mu\text{m}$  (see an example on figure 20). Laser intensities estimated in figures 25(a)–25(c) are 0.65, 1.1, and 1.3, in units of  $10^{14}\text{ W cm}^{-2}$ , respectively. The main features in the spectra are the deep minima at 38.2 eV and 40.4 eV, at the

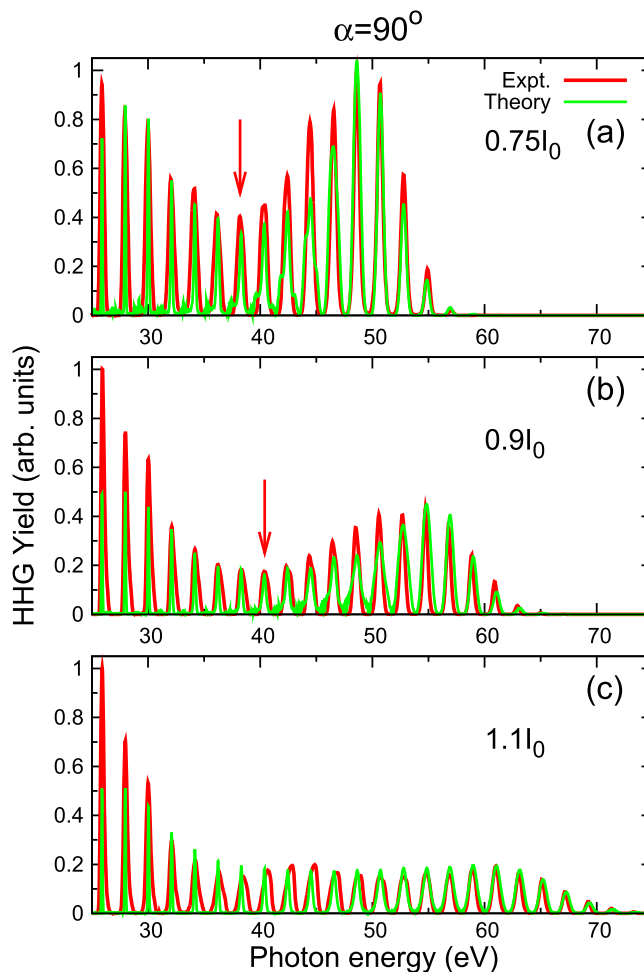


**Figure 25.** Comparison of experimental (red lines) and theoretical (green lines) HHG spectra of aligned  $\text{N}_2$ . Harmonic driving laser is a 1200 nm one, and the pump-probe angle  $\alpha = 90^\circ$ . Laser intensities in the simulations are indicated in the figure where  $I_0 = 10^{14}\text{ W cm}^{-2}$ . Alignment degree is  $\langle \cos^2 \theta \rangle = 0.60$ . Other laser and setup information is given in the text. In the simulations, only  $\sigma$  orbital is included in (a) and (b), and both  $\sigma$  and  $\pi$  orbitals are included in (c). Spectral minima are indicated by the arrows. Adapted from [58].

two lower intensities in figures 25(a) and 25(b), respectively. The minimum disappears at the higher intensity in figure 25(c). From the simulations, we found that the intensities (in the center of the gas jet) of 0.75, 0.9, and 1.1 to coincide with the experimental HHG cutoff as indicated in the figure. Other parameters are closely matched to the experimental ones. The HHG spectra from the simulation and experiment are normalized at the cutoff. For the two lower intensities in figures 25(a) and (b), we include harmonics initiated from the  $\sigma$  orbital (the HOMO) only. Both the shape and the precise positions of the minima of the spectra are reproduced by the simulation. At the higher intensity in figure 25(c), we include HHG from both the  $\sigma$  and  $\pi$  orbitals (the HOMO and HOMO-1). A very good agreement between theory and experiment (correct shape and no minimum in the spectrum) is achieved. If only the  $\sigma$  orbital is included, the theory could not be made to reproduce the correct spectral shape. It would also predicted a minimum in the spectrum

which was not seen in the experiment. To generate the theoretical results, photoionization transition dipole matrix elements, including the amplitude and phase, from all orientation angles of fixed-in-space  $N_2$  molecules over the covered photon energy range of 25 to 70 eV are calculated. In fact, these same matrix elements are used in the QRS theory independent of whether the molecules are isotropically distributed or parallel aligned with respect to laser's polarization. In fact, even if the laser's wavelength and/or intensity are changed, the calculations of HHG at the single-molecule level would require the calculations of new returning electron wave packets only. Additional experiments on  $N_2$  molecules have been reported widely in the literature, see [6, 8, 10, 184, 185, 187–193], and the QRS theory has been used to interpret these observations [46, 51, 55, 56, 179, 185].

### 5.2. Application to laser waveform synthesis for enhancement of HHG yields

One of the main goals in HHG research is to create bright coherent table-top light source from the XUV to soft X-rays. Since HHG cutoff scales as  $3.2U_p \sim I_0 \lambda^2$ , one might expect two simple ways to reach high energy photons: One is to increase laser intensity  $I_0$ , the second is to increase its wavelength. However, it is clear that one cannot increase laser intensity too much due to the ground state depletion and the excess free electrons in the medium which would destroy good phase matching. Nor can one just increase the wavelength alone. From the analysis in section 3 and [61, 131, 132, 135], the unfavored wavelength scaling means that harmonic yields would diminish drastically as the wavelength is increased. One may try to increase the target density (or pressure), which in fact has been implemented in the waveguide setup by the JILA group [68, 69]. Nevertheless, there is an optimal range for target pressure in any medium [69] that prevents further enhancement. While enhancement of macroscopic HHG yield may be achieved by adjusting phase matching conditions, the enhancement factor so far is not large enough to overcome the difficulty of generating useful high harmonics toward the soft x-ray region [194, 195], except probably only for application with condensed medium targets.

Recently we have demonstrated [176] that by combining just two or three lasers of different colors, the HHG yields can be enhanced by two or more orders of magnitude, as compared to the single color one without the increase of the total pulse energy. The principle of this waveform synthesis is shown in figure 26(a), where we compare the electric fields of the optimized two-color waveform and the single-color one (the fundamental) in one optical cycle of the fundamental laser. With a sinusoidal single color laser pulse, from the QO theory, harmonics are generated within one optical cycle by a long-trajectory or a short-trajectory electron. Harmonics from the long-trajectory electrons are stronger but they do not phase match well in the gas medium. Thus the strategy is to generate a new waveform which would generate more short-trajectory harmonics. This should be done by keeping the free electron density in the medium nearly constant to avoid

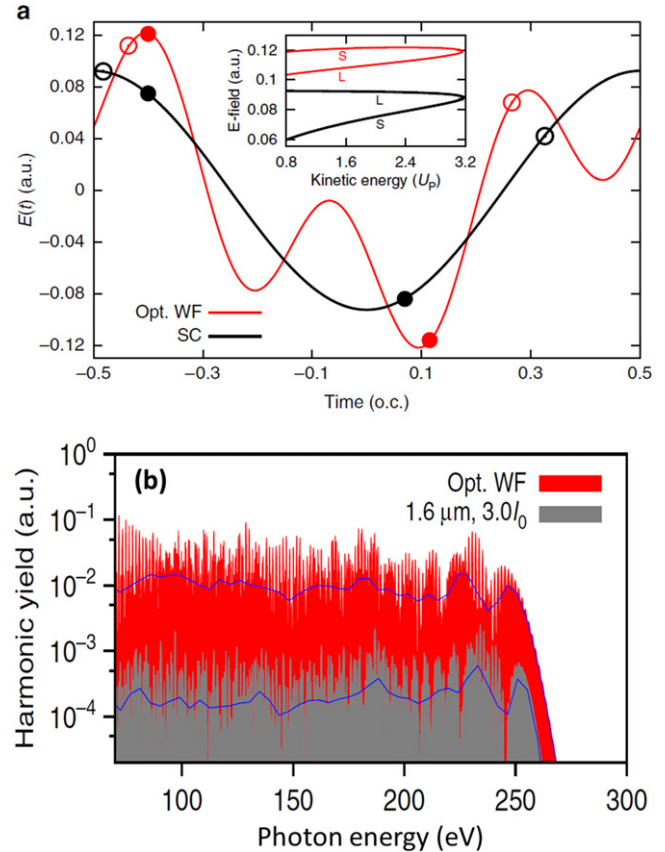


**Figure 26.** (a) Electric field of a single color (SC) and optimal two-color lasers. The filled (empty) circles correspond to the ionization and recombination times for the short (long) trajectory at returning electron energy of  $2U_p$ . The inset shows electric fields vs returning electron energy from long and short trajectories for the two cases. (b) An example of the harmonic spectra from SC and optimal two-color waveform at the single atom level, illustrating the enhancement over an order of magnitude. Adapted from [176].

plasma defocusing and excessive phase mismatching. The optimized waveform is derived by adjusting the relative phase and amplitude of each of the driving lasers with the constraint that the total ionization yield is set at a prescribed level and that harmonics from the short trajectory electrons be stronger than from the long trajectory ones while the cutoff energy is more or less fixed. Using genetic algorithm, such an optimized waveform can be readily obtained. In each iteration, the single atom harmonic spectra are calculated using the QRS. In figure 26(a) an example of such an optimized waveform is shown. It is found that the instantaneous electric field for short trajectory electrons in the optimized waveform is enhanced by 50%, resulting in an increase of ionization rate by about one hundred fold due to the exponential increase of tunneling ionization rate (see, for example, figure 12(c) for the case of hydrogen). Figure 26(b) shows the enhancement of single-atom harmonic spectra generated from the optimized waveform. This example illustrates how the factorization feature of the QRS is useful for identifying the optimal waveform since the calculation of harmonic spectra for each optical field for a given target amounts to the calculation of the returning electron wave packet only. The latter can be

carried out within the SFA which is computationally very efficient. Additional recent works on waveform synthesis can be found in our recent publications [176, 196, 197].

### 5.3. Application to high-energy photoelectrons and to nonsequential double ionization

Although we mainly focus on HHG in this Tutorial, the concept of returning electron wave packet applies to other rescattering phenomena such as HATI and NSDI as well. Instead of photo-recombining as in the HHG process, in HATI, the returning electron is elastically scattered from the parent ion [17, 26, 27, 45], and in NSDI it is inelastically scattered from the ion by kicking out another electron [17, 28–31, 198]. Methods for calculating the returning electron wave packets based on the SFA are quite similar and have been described before [12, 30, 199]. Briefly, for HATI from an atomic target, the photoelectron momentum distribution  $D(k, \theta)$  can be expressed as

$$D(k, \theta) = W(k_r) \sigma(k_r, \theta_r), \quad (157)$$

where  $\sigma(k_r, \theta_r)$  is the electron-parent ion elastic differential cross section (DCS) at the scattering momentum  $k_r$  and scattering angle  $\theta_r$ . Assuming that  $z$  axis is parallel to the laser polarization axis, the detected momentum  $\mathbf{k}$  and the scattering momentum are related by

$$k_z = k \cos \theta = -A_r \mp k_r \cos \theta_r \quad (158)$$

$$k_y = k \sin \theta = k_r \sin \theta_r. \quad (159)$$

Here  $A_r$  is the vector potential at the moment of recollision. Equation (158) shows that upon recollision, the electron changes its direction and gains a momentum  $-A_r$  along laser polarization direction after it has exited the laser field. Only the backscattered electrons can be well described by the QRS, since forwardly rescattered low energy electrons will interfere with direct tunnel ionized electron. As the laser wavelength increases, the direct electron distribution will be more localized along the laser polarization, thus the range of validity of the QRS will be increased towards smaller scattering angles. The wave packet can be calculated within the SFA [12, 199]. Similar to the HHG process, it can also be calculated and analyzed in terms of short and long trajectories within the QO theory [27]. The same returning electron wave packet can be used for the NSDI processes [12, 30, 200].

The simple relationship in equation (157) allows accurate extraction of elastic DCS from laser experiments [45, 201–204] for backscattered electrons. More important application is the retrieval of real-space structures from molecules. Nevertheless, retrieval of real-space molecular structures from the DCS is difficult since it is an inverse scattering problem. At low energies, accurate theoretical DCS can only be obtained by full quantum-mechanical calculations. Fortunately, simplification comes for large momentum transfer collisions, where elastic scattering amplitudes can be calculated as due to coherent contribution from each atom in a molecule, as in the independent-atom model (IAM). This fact has been utilized in the proposed laser-induced electron diffraction (LIED) technique [205] for HATI electrons to

retrieve the molecular bond lengths, in a similar manner to the conventional electron diffraction. Experimentally, this can be achieved by using a mid-infrared laser with a relative long wavelength (above about  $2 \mu\text{m}$ ), so that the returning electron cutoff energy ( $\sim I_0 \lambda^2$ ) can be greatly increased. In fact, LIED experiment has been used with the wavelength of about  $2 \mu\text{m}$  to extract the molecular bond length in  $N_2$  and  $O_2$  by Blaga *et al* [206]. Quite recently, extraction of two bond lengths in aligned  $C_2H_2$  has also been reported by Pullen *et al* [207] using  $3.1 \mu\text{m}$  laser with 160 kHz repetition rate.

It is expected that LIED can be performed to retrieve structure information from dynamically evolving targets in the near future. Nevertheless, the HATI yields drop quickly with increased laser wavelength. It is therefore highly desirable to optimize the laser waveform to enhance the signals, as in case of HHG.

## 6. Summary and outlook

In this Tutorial we have presented detailed description of the SFA and one of its modifications, the QRS, with the focus on high-order harmonics generated by mid-infrared lasers. For long wavelength driving lasers, the saddle point approximation that is used to derive the QO theory from the SFA becomes more accurate. From the QO theory, classical concepts for quantities such as ionization and recombination time, long and short trajectory electrons, single and multiple returns, etc., can all be isolated with their own semiclassical phases. Thus contribution to the amplitude and phase of the harmonic dipole at a given energy from each orbit can be separated. Within the QO, it is further shown that harmonic dipole in the energy domain can be factorized. This factorization allows the extraction of a returning electron wave packet which largely depends only on the laser, and a recombination dipole term which depends only on the target.

The concept of a returning electron wave packet is at the heart of the QRS theory. It combines the ionization and propagation steps in the standard three-step model and therefore contains all the nonlinear physics of the HHG process. Since electron-laser interaction is included ‘exactly’ in the SFA, the electron wave packet obtained from the SFA is accurate whenever the electron-ion core interaction is weak, i.e., during the propagation step. In the third step, recombination occurs near the ion core and thus the SFA is not accurate. In the QRS this part is replaced by accurate transition dipole. The latter is a one-photon process and computational packages for atomic and molecular photoionization are available, which can include elaborate electron correlation effect in a many-electron system. This simple QRS approach allows HHG simulation to be performed even for complex polyatomic molecules [52–54] which are otherwise hardly tractable.

In this Tutorial we did not present many examples of comparing the QRS theory with experimental HHG data. The interested readers are directed to the original publications mentioned in the text. The QRS is a rescattering model, thus it also applies to HATI and NSDI processes. There are still

many areas in strong field physics where the SFA or its extensions have been used but were not covered in this Tutorial. For example, HHG and other rescattering phenomena may be driven by elliptically polarized, or by two orthogonal linearly polarized pulses. In attosecond physics, XUV pulses may be used to generate photoelectrons in the presence of a moderately intense infrared laser. The SFA and its extensions have been found to be useful for studying such problems and it was at the heart of the theory behind the characterization of the phase of single attosecond pulses, called FROG-CRAB [208, 209]. As laser technology continues to advance toward longer wavelength and higher repetition rates, and for better waveform manipulation, ample opportunities lie ahead for continuing discovery in HHG and other strong-field rescattering phenomena. It will not be surprising to find that the simple SFA and its extensions continues to play an important role for understanding potentially very complicated nonlinear phenomena.

## Acknowledgments

This work was supported in part by the Chemical Sciences, Geosciences and Biosciences Division, Office of Basic Energy Sciences, Office of Science, US Department of Energy under grant no. DE-FG02-86ER13491 and DE-FG02-06ER15832. Partial support also was provided by Air Force Office of Scientific Research FA9550-14-1-0255 grant and by the National Science Foundation under Award No. IIA-1430493.

## References

- [1] Krausz F and Ivanov M 2009 *Rev. Mod. Phys.* **81** 163–72 pages
- [2] Goulielmakis E *et al* 2008 *Science* **320** 1614
- [3] Zhao K, Zhang Q, Chini M, Wu Y, Wang X and Chang Z 2012 *Opt. Lett.* **37** 3891
- [4] López-Martens R *et al* 2005 *Phys. Rev. Lett.* **94** 033001
- [5] Lein M, Hay N, Velotta R, Marangos J P and Knight P L 2002 *Phys. Rev. Lett.* **88** 183903
- [6] Itatani J, Levesque J, Zeidler D, Niikura H, Pepin H, Kieffer J C, Corkum I P B and Villeneuve D M 2004 *Nature* **432** 867
- [7] Kanai T, Minemoto S and Sakai H 2005 *Nature* **435** 470
- [8] McFarland B K, Farrell J P, Bucksbaum P H and Guhr M 2008 *Science* **322** 1232
- [9] Smirnova O, Mairesse Y, Patchkovskii S, Dudovich N, Villeneuve D, Corkum P and Ivanov M Y 2009 *Nature* **460** 972
- [10] Haessler S *et al* 2010 *Nat. Phys.* **6** 200
- [11] Le A-T, Lucchese R R, Lee M T and Lin C D 2009a *Phys. Rev. Lett.* **102** 203001
- [12] Lin C D, Le A-T, Chen Z, Morishita T and Lucchese R 2010 *J. Phys. B: At. Mol. Opt. Phys.* **43** 122001
- [13] Spector L S, Artamonov M, Miyabe S, Martinez T, Seideman T, Guehr M and Bucksbaum P H 2014 *Nat. Commun.* **5** 3190
- [14] Li W, Zhou X, Lock R, Patchkovskii S, Stolow A, Kapteyn H C and Murnane M M 2008 *Science* **322** 1207
- [15] Wörner H, Bertrand J, Kartashov D, Corkum P and Villeneuve D 2010 *Nature* **466** 604
- [16] Wörner H J *et al* 2011 *Science* **334** 208
- [17] Corkum P B 1993 *Phys. Rev. Lett.* **71** 1994
- [18] Krause J L, Schafer K J and Kulander K C 1992 *Phys. Rev. Lett.* **68** 3535
- [19] Kuchiev M Y 1987 *JETP Lett.* **45** 404
- [20] Lewenstein M, Balcou P, Ivanov M Y, L’Huillier A and Corkum P B 1994 *Phys. Rev. A* **49** 2117
- [21] L’Huillier A, Lewenstein M, Salières P, Balcou P, Ivanov M Y, Larsson J and Wahlström C G 1993 *Phys. Rev. A* **48** R3433
- [22] Keldysh L 1965 *Sov. Phys. JETP* **20** 1307
- [23] Faisal F H M 1973 *J. Phys. B: At. Mol. Phys.* **6** L89
- [24] Reiss H R 1980 *Phys. Rev. A* **22** 1786
- [25] Becker A and Faisal F H M 2005 *J. Phys. B: At. Mol. Opt. Phys.* **38** R1
- [26] Milosevic D B, Paulus G G, Bauer D and Becker W 2006 *J. Phys. B: At. Mol. Opt. Phys.* **39** R203
- [27] Becker W, Grasbon F, Kopold R, Milošević D, Paulus G and Walther H 2002 *Advances in Atomic, molecular, and optical physics* **48** 35
- [28] Kopold R, Becker W, Rottke H and Sandner W 2000a *Phys. Rev. Lett.* **85** 3781
- [29] Figueira de Morisson Faria C, Schomerus H, Liu X and Becker W 2004 *Phys. Rev. A* **69** 043405
- [30] Micheau S, Chen Z, Le A-T and Lin C D 2009 *Phys. Rev.* **79** 013417
- [31] Chen Z, Liang Y and Lin C D 2010a *Phys. Rev. Lett.* **104** 253201
- [32] Tong X-M and Chu S-I 1998 *Phys. Rev. A* **57** 452
- [33] Chu X and Chu S-I 2001 *Phys. Rev. A* **63** 023411
- [34] Chu S-I 2005 *J. Chem. Phys.* **123** 062207
- [35] Luppi E and Head-Gordon M 2012 *Mol. Phys.* **110** 909
- [36] Dundas D 2012 *J. Chem. Phys.* **136** 194303
- [37] Zhang B, Yuan J and Zhao Z 2013 *Phys. Rev. Lett.* **111** 163001
- [38] Mack M R, Whitenack D and Wasserman A 2013 *Chem. Phys. Lett.* **558** 15 ISSN 0009-2614
- [39] Li P-C and Chu S-I 2013 *Phys. Rev. A* **88** 053415
- [40] Telnov D A, Sosnova K E, Rozenbaum E and Chu S-I 2013 *Phys. Rev. A* **87** 053406
- [41] Ivanov M Y, Brabec T and Burnett N 1996 *Phys. Rev. A* **54** 742
- [42] Salières P *et al* 2001 *Science* **292** 902
- [43] Milosevic D B and Becker W 2002 *Phys. Rev. A* **66** 063417
- [44] Sansone G, Vozzi C, Stagira S and Nisoli M 2004 *Phys. Rev. A* **70** 013411
- [45] Morishita T, Le A-T, Chen Z and Lin C D 2008 *Phys. Rev. Lett.* **100** 013903
- [46] Le A-T, Lucchese R R, Tonzani S, Morishita T and Lin C D 2009b *Phys. Rev.* **80** 013401
- [47] Le A-T, Morishita T and Lin C D 2008a *Phys. Rev.* **78** 023814
- [48] Le A-T, Picca R D, Fainstein P D, Telnov D A, Lein M and Lin C D 2008b *J. Phys. B: At. Mol. Opt. Phys.* **41** 081002
- [49] Minemoto S, Umegaki T, Oguchi Y, Morishita T, Le A-T, Watanabe S and Sakai H 2008 *Phys. Rev.* **78** 061402
- [50] Wörner H J, Niikura H, Bertrand J B, Corkum P B and Villeneuve D M 2009 *Phys. Rev. Lett.* **102** 103901
- [51] Le A-T, Lucchese R R and Lin C D 2010 *Phys. Rev. A* **82** 023814
- [52] Wong M C H, Le A-T, Alharbi A F, Boguslavskiy A E, Lucchese R R, Brichta J-P, Lin C D and Bhardwaj V R 2013 *Phys. Rev. Lett.* **110** 033006
- [53] Le A-T, Lucchese R R and Lin C D 2013a *Phys. Rev. A* **87** 063406

- [54] Le A-T, Lucchese R R and Lin C D 2013b *Phys. Rev. A* **88** 021402
- [55] Jin C, Wörner H J, Tosa V, Le A-T, Bertrand J B, Lucchese R R, Corkum P B, Villeneuve D M and Lin C D 2011a *J. Phys. B: At. Mol. Opt. Phys.* **44** 095601
- [56] Jin C, Le A-T and Lin C D 2011b *Phys. Rev. A* **83** 023411
- [57] Jin C, Le A-T and Lin C D 2011c *Phys. Rev. A* **83** 053409
- [58] Jin C, Bertrand J B, Lucchese R R, Wörner H J, Corkum P B, Villeneuve D M, Le A-T and Lin C D 2012 *Phys. Rev. A* **85** 013405
- [59] Le V-H, Le A-T, Xie R-H and Lin C D 2007a *Phys. Rev.* **76** 013414
- [60] Frolov M V, Manakov N L, Sarantseva T S and Starace A F 2009a *J. Phys. B: At. Mol. Opt. Phys.* **42** 035601
- [61] Frolov M V, Manakov N L, Sarantseva T S, Emelin M Y, Ryabikin M Y and Starace A F 2009b *Phys. Rev. Lett* **102** 243901
- [62] Frolov M V, Manakov N L, Sarantseva T S and Starace A F 2011 *Phys. Rev. A* **83** 043416
- [63] Frolov M V, Manakov N L, Popov A M, Tikhonova O V, Volkova E A, Silaev A A, Vvedenskii N V and Starace A F 2012 *Phys. Rev. A* **85** 033416
- [64] Okajima Y, Tolstikhin O I and Morishita T 2012 *Phys. Rev. A* **85** 063406
- [65] Colosimo P *et al* 2008 *Nat. Phys.* **4** 386
- [66] Hong K-H, Huang S-W, Moses J, Fu X, Lai C-J, Cirmi G, Sell A, Granados E, Keathley P and Kärtner F X 2011 *Opt. Express* **19** 15538
- [67] Hong K-H, Lai C-J, Gkortsas V-M, Huang S-W, Moses J, Granados E, Bhardwaj S and Kärtner F X 2012 *Phys. Rev. A* **86** 043412
- [68] Popmintchev T, Chen M-C, Arpin P, Murnane M M and Kapteyn H C 2010 *Nat. Photonics* **4** 822
- [69] Popmintchev T *et al* 2012 *Science* **336** 1287
- [70] Nobuhisa Ishii K K, Kitano K, Kanai T, Watanabe S and Itatani J 2014 *Nat. Commun.* **5** 3331
- [71] Silva F, Teichmann S M, Cousin S L, Hemmer M and Biegert J 2015a *Nat. Commun.* **6** 6611
- [72] Ba Dinh K, Vu Le H, Hannaford P and Van Dao L 2014 *J. Appl. Phys.* **115** 203103
- [73] Milosevic D B, Paulus G G and Becker W 2003 *Opt. Express* **11** 1418
- [74] Chen Z, Morishita T, Le A-T and Lin C D 2007 *Phys. Rev.* **76** 043402
- [75] Dahlström J M, L'Huillier A and Maquet A 2012 *J. Phys. B: At. Mol. Opt. Phys.* **45** 183001
- [76] Arfken G and Weber H 1995 *Mathematical Methods for Physicists* (San Diego: Academic Press)
- [77] Chirila C C and Lein M 2006 *Phys. Rev. A* **73** 023410
- [78] Ammosov M, Delone N and Krainov V 1986 *Sov. Phys. JETP* **64** 1191
- [79] Krainov V and Ristic V 1992 *Sov. Phys. JETP* **74** 789
- [80] Auguste T, Catoire F, Agostini P, DiMauro L F, Chirila C C, Yakovlev V S and Salières P 2012 *New J. Phys.* **14** 103014
- [81] Austin D R and Biegert J 2012 *Phys. Rev. A* **86** 023813
- [82] Gaarde M B and Schafer K J 2002 *Phys. Rev. A* **65** 031406
- [83] Perez-Hernandez J A, Ramos J, Roso L and Plaja L 2010 *Laser Phys.* **20** 1044
- [84] Tolstikhin O I, Morishita T and Watanabe S 2010 *Phys. Rev. A* **81** 033415
- [85] Gribakin G F and Kuchiev M Y 1997 *Phys. Rev. A* **55** 3760
- [86] Chipperfield L, Knight P, Tisch J and Marangos J 2006 *Opt. Commun.* **264** 494
- [87] Starace A 1982 *Handbuch der Physik* **31** 1
- [88] Gordon A and Kärtner F X 2005 *Phys. Rev. Lett.* **95** 223901
- [89] Chirila C C and Lein M 2007 *J. Mod. Opt.* **54** 1039
- [90] Le A-T, Tong X M and Lin C D 2007b *J. Mod. Opt.* **54** 967
- [91] Becker A, Plaja L, Moreno P, Nurhuda M and Faisal F H M 2001 *Phys. Rev. A* **64** 023408
- [92] Smirnova O, Mouritzen A S, Patchkovskii S and Ivanov M Y 2007 *J. Phys. B: At. Mol. Opt. Phys.* **40** F197
- [93] Smirnova O, Spanner M and Ivanov M 2008 *Phys. Rev.* **77** 033407
- [94] Perelomov A and Popov V 1967 *Sov. Phys. JETP* **25** 336–43
- [95] Granados C and Plaja L 2012 *Phys. Rev. A* **85** 053403
- [96] Odzak S and Milosevic D B 2009 *Phys. Rev. A* **79** 023414
- [97] Pérez-Hernández J A, Roso L and Plaja L 2009 *Opt. Express* **17** 9891
- [98] Odzak S and Milosevic D B 2010 *Phys. Rev. A* **82** 023412
- [99] Ciappina M F, Chirilă C C and Lein M 2007 *Phys. Rev. A* **75** 043405
- [100] Spiewanowski M D, Etches A and Madsen L B 2013 *Phys. Rev. A* **87** 043424
- [101] Spiewanowski M D and Madsen L B 2014 *Phys. Rev. A* **89** 043407
- [102] Bauer D, Milošević D B and Becker W 2005 *Phys. Rev. A* **72** 023415
- [103] Kjeldsen T K and Madsen L B 2004 *J. Phys. B: At. Mol. Opt. Phys.* **37** 2033
- [104] Perelomov A, Popov V and Terentev M 1966 *Sov. Phys. JETP* **23** 924
- [105] Popov V S 2004 *Phys.-Usp.* **47** 855
- [106] Muth-Böhm J, Becker A and Faisal F H M 2000 *Phys. Rev. Lett.* **85** 2280
- [107] Frisch M J *et al* 2004 Gaussian 03, Revision C.02 (Wallingford CT: Gaussian Inc.)
- [108] Schmidt M W *et al* 1993 *J. Comput. Chem.* **14** 1347 ISSN 1096-987X
- [109] Tong X M, Zhao Z X and Lin C D 2002 *Phys. Rev. A* **66** 033402
- [110] Benis E P, Xia J F, Tong X M, Faheem M, Zamkov M, Shan B, Richard P and Chang Z 2004 *Phys. Rev. A* **70** 025401
- [111] Zhao S-F, Liu L and Zhou X-X 2014 *Opt. Commun.* **313** 74 ISSN 0030-4018
- [112] Zhao S-F, Xu J, Jin C, Le A-T and Lin C D 2011 *J. Phys. B: At. Mol. Opt. Phys.* **44** 035601
- [113] Ilkov F A, Decker J E and Chin S L 1992 *J. Phys. B: At. Mol. Opt. Phys.* **25** 4005
- [114] Larochelle S F J, Talebpour A and Chin S L 1998 *J. Phys. B: At. Mol. Opt. Phys.* **31** 1215
- [115] Popruzhenko S V, Mur V D, Popov V S and Bauer D 2008 *Phys. Rev. Lett.* **101** 193003
- [116] Tolstikhin O I, Morishita T and Madsen L B 2011 *Phys. Rev. A* **84** 053423
- [117] Awasthi M, Vanne Y V, Saenz A, Castro A and Decleva P 2008 *Phys. Rev. A* **77** 063403
- [118] Kobus J, Laaksonen L and Sundholm D 1996 *Comput. Phys. Commun.* **98** 346 ISSN 0010-4655
- [119] Madsen L B, Jensen F, Tolstikhin O I and Morishita T 2013 *Phys. Rev. A* **87** 013406
- [120] Zhao S-F, Jin C, Le A-T, Jiang T F and Lin C D 2010 *Phys. Rev. A* **81** 033423
- [121] Wang J-P, Zhao S-F, Zhang C-R, Li W and Zhou X-X 2014 *Mol. Phys.* **112** 1102
- [122] Madsen L B, Tolstikhin O I and Morishita T 2012 *Phys. Rev. A* **85** 053404
- [123] Tolstikhin O I, Madsen L B and Morishita T 2014 *Phys. Rev. A* **89** 013421
- [124] Holmegaard L *et al* 2010 *Nat. Phys.* **6** 428
- [125] Li H, Ray D, De S, Znakovskaya I, Cao W, Laurent G, Wang Z, Kling M F, Le A T and Cocke C L 2011 *Phys. Rev. A* **84** 043429
- [126] Wu J, Schmidt L P H, Kunitski M, Meckel M, Voss S, Sann H, Kim H, Jahnke T, Czasch A and Dörner R 2012 *Phys. Rev. Lett.* **108** 183001

- [127] Yudin G L and Ivanov M Y 2001 *Phys. Rev. A* **64** 013409
- [128] Torlina L and Smirnova O 2012 *Phys. Rev. A* **86** 043408
- [129] Torlina L, Ivanov M, Walters Z B and Smirnova O 2012 *Phys. Rev. A* **86** 043409
- [130] Kopold R, Milošević D B and Becker W 2000b *Phys. Rev. Lett.* **84** 3831
- [131] Le A-T, Wei H, Jin C, Tuoc V N, Morishita T and Lin C D 2014 *Phys. Rev. Lett.* **113** 033001
- [132] Tate J, Auguste T, Muller H G, Salières P, Agostini P and DiMauro L F 2007 *Phys. Rev. Lett.* **98** 013901
- [133] Hernandez-Garcia C, Perez-Hernandez J A, Popmintchev T, Murnane M M, Kapteyn H C, Jaron-Becker A, Becker A and Plaja L 2013 *Phys. Rev. Lett.* **111** 033002
- [134] He L, Li Y, Wang Z, Zhang Q, Lan P and Lu P 2014 *Phys. Rev. A* **89** 053417
- [135] Schiessl K, Ishikawa K L, Persson E and Burgdörfer J 2007 *Phys. Rev. Lett.* **99** 253903
- [136] Frolov V, Manakov M L, N, Xiong W-H, Peng L-Y, Burgdörfer J and Starace A F 2015 *Phys. Rev. Lett.* **114** 069301
- [137] Jin C, Le A-T and Lin C D 2009 *Phys. Rev.* **79** 053413–12
- [138] Gaarde M B, Tate J L and Schafer K J 2008 *J. Phys. B: At. Mol. Opt. Phys.* **41** 132001
- [139] Jin C 2013 *Theory of Nonlinear Propagation of High Harmonics Generated in a Gaseous Medium* (Springer)
- [140] Esarey E, Sprangle P, Krall J and Ting A 1997 *Quantum Electronics, IEEE Journal of* **33** 1879 ISSN 0018-9197
- [141] Takahashi E, Tosa V, Nabekawa Y and Midorikawa K 2003 *Phys. Rev. A* **68** 023808
- [142] Geissler M, Tempea G, Scrinzi A, Schnürer M, Krausz F and Brabec T 1999 *Phys. Rev. Lett.* **83** 2930
- [143] Rae S C and Burnett K 1992 *Phys. Rev. A* **46** 1084
- [144] Priori E *et al* 2000 *Phys. Rev. A* **61** 063801
- [145] Tong X M and Lin C D 2005 *J. Phys. B: At. Mol. Opt. Phys.* **38** 2593
- [146] Börzsönyi A, Heiner Z, Kalashnikov M P, Kovács A P and Osvay K 2008 *Appl. Opt.* **47** 4856
- [147] Leonard P 1974 *At. Data Nucl. Data Tables* **14** 21 ISSN 0092-640X
- [148] Lehmeier H, Leupacher W and Penzkofer A 1985 *Opt. Commun.* **56** 67 ISSN 0030-4018
- [149] Li X F, L'Huillier A, Ferray M, Lompré L A and Mainfray G 1989 *Phys. Rev. A* **39** 5751
- [150] Loriot V, Hertz E, Faucher O and Lavorel B 2009 *Opt. Exp.* **14** 13429
- [151] Loriot V, Hertz E, Faucher O and Lavorel B 2010 *Opt. Exp.* **18** 3011
- [152] Koga J K, Naumova N, Kando M, Tsintsadze L N, Nakajima K, Bulanov S V, Dewa H, Kotaki H and Tajima T 2000 *Phys. Plasmas* **7** 5223–31
- [153] Boyd R 2003 *Nonlinear Optics* (San Diego: Academic Press)
- [154] Jin C and Lin C D 2012 *Phys. Rev. A* **85** 033423
- [155] Ye P, Teng H, He X-K, Zhong S-Y, Wang L-F, Zhan M-J, Zhang W, Yun C-X and Wei Z-Y 2014 *Phys. Rev. A* **90** 063808
- [156] Nisoli M *et al* 2002 *Phys. Rev. Lett.* **88** 033902
- [157] Altucci C *et al* 2003 *Phys. Rev. A* **68** 033806
- [158] Dubrouil A, Hort O, Catoire F, Descamps D, Petit S, Mével E, Strelkov V and Constant E 2014 *Nat. Commun.* **5** 4637
- [159] Constant E, Dubrouil A, Hort O, Petit S, Descamps D and Mével E 2012 *J. Phys. B* **45** 074018
- [160] Tosa V, Kim H T, Kim I J and Nam C H 2005 *Phys. Rev. A* **71** 063807
- [161] Chantler C T, Olsen K, Dragoset R A, Chang J, Kishore A R, Kotochigova S A and Zucker D S 2000 *X-ray form Factor, Stenuation and Scattering Tables (version)* **2** 1
- [162] Henke B, Gullikson E and Davis J 1993 *At. Data Nucl. Data Tables* **54** 181 ISSN 0092-640X
- [163] Siegman A 1986 *Lasers* (CA: University Science, Mill Valley)
- [164] L'Huillier A, Balcou P, Candel S, Schafer K J and Kulander K C 1992 *Phys. Rev. A* **46** 2778
- [165] Tosa V, Kim K T and Nam C H 2009 *Phys. Rev. A* **79** 043828
- [166] Lewenstein M, Salières P and L'Huillier A 1995 *Phys. Rev. A* **52** 4747
- [167] Balcou P, Dederichs A S, Gaarde M B and L'Huillier A 1999 *J. Phys. B: At. Mol. Opt. Phys.* **32** 2973
- [168] Gaarde M B, Salin F, Constant E, Balcou P, Schafer K J, Kulander K C and L'Huillier A 1999 *Phys. Rev. A* **59** 1367
- [169] Muller H G 1999 *Phys. Rev. A* **60** 1341
- [170] Kutzner M, Radojević V and Kelly H P 1989 *Phys. Rev. A* **40** 5052
- [171] Lucchese R R, Raseev G and McKoy V 1982 *Phys. Rev. A* **25** 2572
- [172] Trallero-Herrero C, Jin C, Schmidt B E, Shiner A D, Kieffer J-C, Corkum P B, Villeneuve D M, Lin C D, Legare F and Le A T 2012 *J. Phys. B: At. Mol. Opt. Phys.* **45** 011001
- [173] Jin C, Le A-T, Trallero-Herrero C A and Lin C D 2011d *Phys. Rev. A* **84** 043411
- [174] Shiner A D, Schmidt B E, Trallero-Herrero C, Wörner H J, Patchkovskii S, Corkum P B, Kieffer J-C, Légaré F and Villeneuve D M 2011 *Nat. Phys.* **7** 464
- [175] Hickstein D D *et al* 2012 *Phys. Rev. Lett.* **109** 073004
- [176] Jin C, Wang G, Wei H, Le A-T and Lin C D 2014a *Nat. Commun.* **5** 4003
- [177] Gianturco F A, Lucchese R R and Sanna N 1994 *J. Chem. Phys.* **100** 6464–71
- [178] Natalense A P P and Lucchese R R 1999 *J. Chem. Phys.* **111** 5344–8
- [179] Le A-T, Lucchese R R and Lin C D 2009 *J. Phys. B: At. Mol. Opt. Phys.* **42** 211001
- [180] Le A-T and Lin C 2011 *J. Mod. Opt.* **58** 1158
- [181] Le A-T, Morishita T, Lucchese R R and Lin C D 2012 *Phys. Rev. Lett.* **109** 203004
- [182] Takahashi E J, Lan P, Mücke O D, Nabekawa Y and Midorikawa K 2010 *Phys. Rev. Lett.* **104** 233901
- [183] Wörner H J, Bertrand J B, Hockett P, Corkum P B and Villeneuve D M 2010 *Phys. Rev. Lett.* **104** 233904
- [184] Rupenyan A, Bertrand J B, Villeneuve D M and Wörner H J 2012 *Phys. Rev. Lett.* **108** 033903
- [185] Ren X, Makhija V, Le A-T, Troß J, Mondal J, Jin J, Kumarappan J and Trallero-Herrero J 2013 *Phys. Rev. A* **88** 043421
- [186] Rupenyan A, Kraus P M, Schneider J and Wörner H J 2013 *Phys. Rev. A* **87** 033409
- [187] Zhou X, Lock R, Wagner N, Li W, Kapteyn H C and Murnane M M 2009 *Phys. Rev. Lett.* **102** 073902–4
- [188] Mairesse Y *et al* 2010 *Phys. Rev. Lett.* **104** 213601
- [189] Wörner H J, Bertrand J B, Hockett P, Corkum P B and Villeneuve D M 2010 *Phys. Rev. Lett.* **104** 233904
- [190] Torres R *et al* 2010 *Optics Express* **18** 3174
- [191] Yoshii K, Miyaji G and Miyazaki K 2011 *Phys. Rev. Lett.* **106** 013904
- [192] Diveki Z, Camper A, Haessler S, Auguste T, Ruchon T, Carré P S B, Guichard R, Caillat J, Maquet A and Taieb R 2012 *New J. Phys.* **14** 023062
- [193] Bertrand J B, Wörner H J, Hockett P, Villeneuve D M and Corkum P B 2012 *Phys. Rev. Lett.* **109** 143001
- [194] Ishii N, Kaneshima K, Kitano K, Kanai T, Watanabe S and Itatani J 2014 *Nat. Commun.* **5** 3331
- [195] Silva F, Teichmann S M, Cousin S L, Hemmer M and Biegert J 2015b *Nat. Commun.* **6** 6611

- [196] Jin C, Wang G, Le A-T and Lin C D 2014b *Scientific Reports* **4** 7067
- [197] Jin C, Stein G J, Hong K-H and Lin C D 2015 *Phys. Rev. Lett.* **115** 043901
- [198] Becker W, Liu X, Ho P J and Eberly J H 2012 *Rev. Mod. Phys.* **84** 1011
- [199] Chen Z, Le A-T, Morishita T and Lin C D 2009 *Phys. Rev.* **79** 033409
- [200] Chen Z, Liang Y and Lin C D 2010b *Phys. Rev. Lett.* **104** 253201
- [201] Ray D *et al* 2008 *Phys. Rev. Lett.* **100** 143002–4
- [202] Okunishi M, Morishita T, Prümper G, Shimada K, Lin C D, Watanabe S and Ueda K 2008 *Phys. Rev. Lett.* **100** 143001
- [203] Ray D, Chen Z, De S, Cao W, Litvinyuk I V, Le A T, Lin C D, Kling M F and Cocke C L 2011 *Phys. Rev. A* **83** 013410
- [204] Xu J *et al* 2012 *Phys. Rev. Lett.* **109** 233002
- [205] Xu J, Chen Z, Le A-T and Lin C D 2010 *Phys. Rev. A* **82** 033403
- [206] Blaga C I, Xu J, DiChiara A D, Sistrunk E, Zhang K, Agostini P, Miller T A, DiMauro L F and Lin C D 2012 *Nature* **483** 194
- [207] Pullen M *et al* 2015 *Nat. Commun.* **6** 7262
- [208] Mairesse Y and Quéré F 2005 *Phys. Rev. A* **71** 011401
- [209] Gagnon J, Goulielmakis E and Yakovlev V 2008 *Applied Physics B* **92** 25